

Design of a Small Aeroacoustic Wind Tunnel

Master Thesis



Design of a Small Aeroacoustic Wind Tunnel

Master Thesis
July, 2018

By
Perrin Vendrig

Copyright: Reproduction of this publication in whole or in part must include the customary bibliographic citation, including author attribution, report title, etc.

Cover photo: Vibeke Hempler, 2012

Published by: DTU, Department of Wind Energy, Nils Koppels Alle, Building 403, 2800 Kgs. Lyngby Denmark
www.vindenergi.dtu.dk

Approval

This thesis has been prepared over nine months at the Department of Wind Energy, at the Technical University of Denmark, DTU, in partial fulfilment for the degree Master of Science in Engineering, MSc Eng.

It is assumed that the reader has a basic knowledge in the areas of aerodynamics, computational fluid dynamics and acoustics.

Perrin Vendrig - s145174

.....
Signature

.....
Date

Summary

In this master thesis project the initial steps for the design of a new wind tunnel for aeroacoustic measurements are made. Well-documented sizing methods for different wind tunnel parts were found in a literature study and were used together with 2D CFD simulations to create a new wind tunnel design. Thick corner vanes were used in this design with the purpose of using them as baffle mufflers to create a better environment for aeroacoustic measurements inside the test section. The performance of the wind tunnel was evaluated thereafter by 3D CFD simulations. The 3D simulations provide an idea of the flow velocities, the flow uniformity, turbulence intensities, pressure losses and noise sources inside the wind tunnel. Since an existing wind tunnel fan and 42 kW motor was to be reused, noise measurements were done to find the noise characteristics of the fan-motor combination and to have an idea of how noise would propagate in the environment where the new wind tunnel would be placed. After the noise measurements, predictions of the transmission loss through the corner vanes were made by using finite element analyses.

The main findings were that a redesign of the first diffuser of the wind tunnel design might be needed as large flow separation was found there. This flow separation also generated a lot of noise and would likely affect aeroacoustic measurements inside the test section. The first diffusers also spoil the flow characteristics downstream. Whether this separation would truly occur in a real situation is uncertain as the Boussinesq simplification in the SST $k - \omega$ model that was used may have predicted the existence of separation incorrectly. Other than that, it was found that the flow characteristics inside the test section were decent and that the fan and motor were good enough to move the flow to decent velocities inside the test section. From the noise measurement it became evident that the fan produces significant noise and after the predictions of transmission losses through the wind tunnel (corners), it could be concluded that the addition of porous lining inside the corners does not attenuate the noise sufficiently for the current design. In order to be able to find the transmission losses numerically, a lot of simplifications had to be made to save on computational resources.

Because of the simplifications and the choice of CFD models, there is an uncertainty of the validity of the current results and findings. Verification and validation is therefore needed before it would be recommended to start constructing the wind tunnel. The first important step that should be taken in continuation of this project would be the verification of the CFD results by utilizing a different model and/or using a Kato-Launder limiter for the used $k - \omega$ model. Then a more precise estimation of the effect of the screens, exit diffuser and inlet/filter should be made. Thereafter, the transmission loss through one of the corners should be measured for validating the 2D simplification made in the predictions and whether predicting numerically the transmission loss at the center frequencies of the octave-bands holds in real situations. Noise predic-

tions with a higher resolution of the frequency range may be required otherwise. Furthermore, it is recommended to find the foremost causes of the fan noise and make improvements based on those findings in order to lower to production of noise and find additional ways to attenuate the noise through the tunnel.

The report is limited to simple design methods and simulations. Aerodynamic optimisation programs for, for example, corner vanes were not available and neither was it attempted to do strong iterative design process which includes both the aerodynamic and acoustic aspects of a wind tunnel. The use of CFD is limited to finding steady-state solutions. Even though transient solutions may give a better understanding of the flow inside the wind tunnel, it is not considered as something necessary to find a good design. Neither the direct and integral method, that require an unsteady solution for finding time-dependent (tonal) noise sources in a flow, can be used, because of the wall bounded flow and the boundary conditions inside a wind tunnel. Furthermore, the lack of computational resources also limits the depth of analysis of the noise. Construction and detailed design are not included in this project either. The design that is found and evaluated in this project can be considered as a concept.

Contents

List of Figures	4
List of Tables	11
1 Introduction	12
2 Literature Study	14
2.1 Relevance of Aeroacoustic Research	14
2.2 Aeroacoustic Experiments	14
2.3 Wind Tunnel Types for Aeroacoustic Measurements	15
2.3.1 Closed Test Section	15
2.3.2 Open-jet Test Section	15
2.3.3 Hybrid Test Section	16
2.4 Aeroacoustic Measurements	17
2.5 Noise Sources of Wind Tunnels	18
2.5.1 Fan and Drive-System	18
2.5.2 Microphones and Microphone Arrays	19
2.5.3 Testing Hardware	19
2.5.4 boundary layer	19
2.6 The Anechoic Environment	20
2.6.1 The Anechoic Chamber	20
2.6.2 Acoustic Lining	21
2.6.3 Fan Improvements	22
2.6.4 Mufflers	22
2.7 Wind Tunnel Design	22
2.7.1 The Settling Chamber, Honeycomb Structure and Screens	23
2.7.2 The Contraction	24
2.7.3 The Diffuser	25
2.7.4 Corner Vanes	26
2.8 Conclusion and Discussion	26
3 Outline and Research Statement	30
4 Sizing of the Wind Tunnel	31
4.1 Settling Chamber	31
4.2 Contraction	31
4.3 test section	35
4.4 Diffuser	36
4.5 Corners and Corner Vanes	37

5	2D CFD Evaluations	43
5.1	Geometry	43
5.2	Meshing	44
5.2.1	Flow Regime and Wall Distance	44
5.2.2	The Turbulent boundary layer	45
5.2.3	Application for Meshing	46
5.2.4	Mesh for Case with Wall Treatment	46
5.2.5	Mesh for Case without Wall Treatment	49
5.2.6	Meshes for Convergence Study	52
5.3	Fluent	52
5.4	Results	53
5.5	Discussion of 2D CFD Results	66
6	3D CFD Simulations	69
6.1	Geometry	69
6.2	Meshing	70
6.2.1	Mesh for the Lower Velocity Limit	70
6.2.2	Mesh for the Lower Velocity Limit with Refined Grid	71
6.2.3	Mesh for the Upper Velocity Limit	71
6.2.4	Mesh for the Upper Velocity Limit with Refined Grid	71
6.2.5	Mesh for the Cases with Wall Treatment	71
6.2.6	Mesh for the Cases with Wall Treatment and Refined Grid	72
6.3	Solver Settings	72
6.4	Solution Monitors	73
6.5	Boundary Conditions	74
6.6	Results	74
6.7	Aerodynamic Noise Sources	87
6.8	Discussion of 3D CFD Results	89
7	Noise Measurements	92
7.1	Experiment Setup	92
7.2	Noise Recordings	98
7.3	Noise Post-Processing	100
7.4	Results	101
7.5	Conclusion and Discussion of Measurement Results	112
8	Transmission Losses	117
8.1	Methodology	117
8.2	Models	118
8.3	Geometry	120
8.4	Meshing and Analysis Settings	121
8.5	Results	127
8.6	Discussion of Transmission Loss Results	135
9	General Conclusion and Discussion	138

10 Recommendations	141
11 Bibliography	143

List of Figures

1	Schematic of the red wind tunnel located on the Lyngby DTU Campus.	13
2	Fifth-order polynomial for the shape of the contraction edges (from MatLab).	33
3	First-order derivative of the polynomial (from MatLab).	33
4	Second-order derivative of the polynomial (from MatLab).	34
5	Shape of the contraction in a 3D domain (from MatLab).	35
6	Sketch of the side-view of the first wind tunnel corner with constraints (from CATIA V5).	39
7	Sketch of the side-view of the second wind tunnel corner with constraints (from CATIA V5).	39
8	Sketch of the side-view of the first corner-vane with constraints (from CATIA V5).	40
9	Sketch of the side-view of the second corner-vane with constraints (from CATIA V5).	40
10	Assembly of the wind tunnel parts (from CATIA V5).	41
11	A simple American-projection with dimensions of the wind tunnel contours (from CATIA V5).	42
12	Zero-thickness model of the wind tunnel geometry (from Ansys).	44
13	Mesh of the zero-thickness model of the wind tunnel (from Ansys Fluent).	47
14	Mesh of the zero-thickness model of the wind tunnel at the first corner (from Ansys Fluent).	47
15	Mesh of the zero-thickness model of the wind tunnel at a corner-vane of the first corner (from Ansys Fluent).	48
16	Mesh of the zero-thickness model of the wind tunnel at the outlet of the contraction (from Ansys Fluent).	48
17	Mesh of the zero-thickness model of the wind tunnel (from Ansys Fluent).	50
18	Mesh of the zero-thickness model of the wind tunnel at the first corner (from Ansys Fluent).	50
19	Mesh of the zero-thickness model of the wind tunnel at a corner-vane of the first corner (from Ansys Fluent).	51
20	Mesh of the zero-thickness model of the wind tunnel at the outlet of the contraction (from Ansys Fluent).	51
21	The convergence history of residuals for the simulation with standard grid and wall treatment at pressure difference of 25 Pa (from Ansys Fluent).	53
22	The convergence history of scaled residuals for the simulation with standard grid and wall treatment at pressure difference of 725 Pa (from Ansys Fluent).	54

23	The convergence history of scaled residuals for the simulation with standard grid and no wall treatment at pressure difference of 25 Pa (from Ansys Fluent).	54
24	The convergence history of scaled residuals for the simulation with standard grid and no wall treatment at pressure difference of 725 Pa (from Ansys Fluent).	55
25	The convergence history of velocity at inlet, outlet and inside the test section for simulation with standard grid and wall treatment at pressure difference of 25 Pa (from Ansys Fluent).	55
26	The convergence history of velocity at inlet, outlet and inside test section for simulation with standard grid and wall treatment at pressure difference of 725 Pa (from Ansys Fluent).	56
27	The convergence history of velocity at inlet, outlet and inside test section for simulation with standard grid and no wall treatment at pressure difference of 25 Pa (from Ansys Fluent).	56
28	The convergence history of velocity at inlet, outlet and inside test section for simulation with standard grid and no wall treatment at pressure difference of 725 Pa (from Ansys Fluent).	57
29	Contour plot of static pressure inside the duct for simulation with standard grid and no wall treatment at pressure difference of 25 Pa (from Ansys Fluent).	57
30	Contour plot of static pressure inside the duct for simulation with standard grid and no wall treatment at pressure difference of 725 Pa (from Ansys Fluent).	58
31	Contour plot of static pressure in the first corner for simulation with standard grid and no wall treatment at pressure difference of 25 Pa (from Ansys Fluent).	58
32	Contour plot of static pressure in the first corner for simulation with standard grid and no wall treatment at pressure difference of 725 Pa (from Ansys Fluent).	59
33	The contour plot of the static pressure in the second corner for the simulation with the standard grid and no wall treatment at a pressure difference of 25 Pa (from Ansys Fluent).	59
34	The contour plot of the static pressure in the second corner for the simulation with the standard grid and no wall treatment at a pressure difference of 725 Pa (from Ansys Fluent).	60
35	The velocity vectors in the first corner for the simulation with the standard grid and no wall treatment at a pressure difference of 25 Pa (from Ansys Fluent).	60
36	The velocity vectors in the first corner for the simulation with the standard grid and no wall treatment at a pressure difference of 725 Pa (from Ansys Fluent).	61
37	The velocity vectors in the second corner for the simulation with the standard grid and no wall treatment at a pressure difference of 25 Pa (from Ansys Fluent).	61

38	The velocity vectors in the second corner for the simulation with the standard grid and no wall treatment at a pressure difference of 725 Pa (from Ansys Fluent).	62
39	The streamlines in the first corner for the simulation with the standard grid and no wall treatment at a pressure difference of 25 Pa (from Ansys Fluent).	62
40	The streamlines in the first corner for the simulation with the standard grid and no wall treatment at a pressure difference of 725 Pa (from Ansys Fluent).	63
41	The streamlines in the second corner for the simulation with the standard grid and no wall treatment at a pressure difference of 25 Pa (from Ansys Fluent).	63
42	The streamlines in the second corner for the simulation with the standard grid and no wall treatment at a pressure difference of 725 Pa (from Ansys Fluent).	64
43	Velocity plotted against the gauge pressure at outlet for the two meshes where wall treatment was used (from MatLab).	64
44	The velocity profile over the duct-height in the middle of the test section for all of the four meshes at a pressure difference of 25 Pa (from MatLab).	65
45	The velocity profile over the duct-height in the middle of the test section for all of the four meshes at a pressure difference of 725 Pa (from MatLab).	65
46	Symmetry model of the wind tunnel geometry (from Ansys). . .	70
47	Convergence history of the velocity inside the test section. Wall treatment indicated by WT (from MatLab).	75
48	Residuals of the simulation with standard grid and no wall treatment (from Ansys Fluent).	76
49	Residuals of the simulation with standard grid and wall treatment (from Ansys Fluent).	76
50	Contour plots of the velocity on the symmetry-plane (from Ansys Fluent).	77
51	Contour plots of the $\overline{vv^{+2}}$ Reynolds stresses on the symmetry-plane (from Ansys Fluent).	77
52	Velocity vector plots of the cross-section at different locations in the first diffuser (from Ansys Fluent).	78
53	Velocity vector plots of the cross-section at different locations in the second diffuser (from Ansys Fluent).	78
54	Contour plots of the $\overline{vv^{+2}}$ Reynolds stresses over the cross-sections at different locations in the first diffuser (from Ansys Fluent). . .	79
55	Contour plot of the $\overline{vv^{+2}}$ Reynolds stresses over the cross-sections at different locations in the second diffuser (from Ansys Fluent). . .	79
56	Contour plot of the static pressure over the cross-sections at different locations in the first diffuser (from Ansys Fluent).	80
57	Contour plot of the static pressure over the cross-sections at different locations in the second diffuser (from Ansys Fluent). . . .	80

58	Streamline plot of the wind tunnel (from Ansys Fluent).	81
59	Velocity contour plot of the cross-section at different locations in the test section (from Ansys Fluent).	81
60	Contour plot of the $\overline{vv'^2}$ Reynolds stresses over the cross-sections at different locations in the test section (from Ansys Fluent).	82
61	Contour plot of the static pressure over the cross-sections at different locations in the test section (from Ansys Fluent).	82
62	Pressure losses (from MatLab).	85
63	Pressure losses (from MatLab)	85
64	Contour plots of the acoustic power level in Decibels found in the wind tunnel diffusers (from Ansys Fluent).	88
65	Contour plots of the acoustic power level in Decibels emitted by the surfaces in the wind tunnel (from Ansys Fluent).	88
66	The first microphone, which can be found near the tunnel outlet.	94
67	The second microphone, which is located next to the tunnel outlet.	94
68	The third microphone, which is placed next to the fan and motor outside of the tunnel.	95
69	The fourth microphone, which is placed in a separate compartment underneath the test section.	95
70	The fifth microphone, which stands next to the test section of the tunnel.	96
71	The sixth microphone, which is placed directly in front of the inlet of the tunnel.	96
72	The seventh microphone, which is located some distance away from the inlet.	97
73	Schematic of the microphones that are placed around the wind tunnel.	97
74	Periodogram of the measured noise for when the wind tunnel is switched off (from MatLab).	101
75	Periodogram of the measured noise at a flow velocity of 10 meters per second in the test section and the background noise subtracted (from MatLab).	102
76	Periodogram of the measured noise at a flow velocity of 20 meters per second in the test section and the background noise subtracted (from MatLab).	102
77	Periodogram of the measured noise at a flow velocity of 30 meters per second in the test section and the background noise subtracted (from MatLab).	103
78	Periodogram of the measured noise at a flow velocity of 40 meters per second in the test section and the background noise subtracted (from MatLab).	103
79	Periodogram of the measured noise at a flow velocity of 50 meters per second in the test section and the background noise subtracted (from MatLab).	104

80	Periodogram of the measured noise at a flow velocity of 60 meters per second in the test section and the background noise subtracted (from MatLab).	104
81	The noise for when the wind tunnel is switched off, shown in 1/3 octave-bands (from MatLab).	105
82	The noise at a flow velocity of 10 meters per second, with the background noise subtracted, shown in 1/3 octave-bands (from MatLab).	105
83	The noise at a flow velocity of 20 meters per second, with the background noise subtracted, shown in 1/3 octave-bands (from MatLab).	106
84	The noise at a flow velocity of 30 meters per second, with the background noise subtracted, shown in 1/3 octave-bands (from MatLab).	106
85	The noise at a flow velocity of 40 meters per second, with the background noise subtracted, shown in 1/3 octave-bands (from MatLab).	107
86	The noise at a flow velocity of 50 meters per second, with the background noise subtracted, shown in 1/3 octave-bands (from MatLab).	107
87	The noise at a flow velocity of 60 meters per second, with the background noise subtracted, shown in 1/3 octave-bands (from MatLab).	108
88	Periodogram of the noise recorded by the first microphone and the background noise subtracted for different flow velocities (from MatLab).	108
89	Periodogram of the noise recorded by the second microphone and the background noise subtracted for different flow velocities (from MatLab).	109
90	Periodogram of the noise recorded by the third microphone and the background noise subtracted for different flow velocities (from MatLab).	109
91	Periodogram of the noise recorded by the fourth microphone and the background noise subtracted for different flow velocities (from MatLab).	110
92	Periodogram of the noise recorded by the fifth microphone and the background noise subtracted for different flow velocities (from MatLab).	110
93	Periodogram of the noise recorded by the sixth microphone and the background noise subtracted for different flow velocities (from MatLab).	111
94	Periodogram of the noise recorded by the seventh microphone and the background noise subtracted for different flow velocities (from MatLab).	111
95	Simplified geometry of the second corner with perforated plate and porous material (from Ansys).	121

96	Close-up of the corner vane of the second corner with perforated plate and porous material (from Ansys).	121
97	Simplified geometry of the complete geometry with perforated plates and porous material (from Ansys).	122
98	Mesh of the first corner, perforated plate and porous material assembly with a cell-size of 2.5 millimeter (from Ansys).	123
99	Mesh of the first corner, perforated plate and porous material assembly with a cell-size of 1.75 millimeter (from Ansys).	124
100	Mesh of the second corner, perforated plate and porous material assembly with a cell-size of 2.5 millimeter (from Ansys).	124
101	Mesh of the second corner, perforated plate and porous material assembly with a cell-size of 1.75 millimeter (from Ansys).	125
102	Mesh of the first corner, perforated plate and porous material assembly as in the complete geometry with a cell-size of 7 millimeter (from Ansys).	125
103	Mesh of the first corner, perforated plate and porous material assembly as in the complete geometry with a cell-size of 5 millimeter (from Ansys).	126
104	Mesh of the second corner, perforated plate and porous material assembly as in the complete geometry with a cell-size of 7 millimeter (from Ansys).	126
105	Mesh of the second corner, perforated plate and porous material assembly as in the complete geometry with a cell-size of 5 millimeter (from Ansys).	127
106	Transmission losses through the corners (from MatLab).	128
107	Transmission losses from fan to test section (from MatLab).	128
108	Noise reduction by applying porous material for the two corners and complete configuration (from MatLab).	129
109	Contour plot of transmission losses through the second corner with the JCA model (from Ansys).	129
110	Contour plot of transmission losses through the second corner with the Miki model (from Ansys).	130
111	Contour plot of transmission losses through the second corner with no porous lining (from Ansys).	130
112	Contour plot of transmission losses through the first corner with the JCA model (from Ansys).	131
113	Contour plot of transmission losses through the first corner with the Miki model (from Ansys).	131
114	Contour plot of transmission losses through the first corner with no porous lining (from Ansys).	132
115	Contour plot of transmission losses from fan to test section with the JCA model (from Ansys).	132
116	Contour plot of transmission losses from fan to test section with the Miki model (from Ansys).	133
117	Contour plot of transmission losses from fan to the test section with no porous lining (from Ansys).	133

118 The transmission losses found in the two corners deducted from
the noise measurements made with the first microphone at a flow
velocity of 40 meters per second (from MatLab). 136

List of Tables

1	Flow uniformity within the test section	66
2	Overview of the area-averaged flow velocities found in the test section and total pressure losses for different simulation cases. . .	68
3	Overview of the flow velocities, turbulence intensities and flow uniformities at different locations in the wind tunnel.	83
4	Overview of the wind tunnel parts with their respective number in Figure 63b.	86
5	Number and time of the recordings.	98
6	Recording log.	99
7	Correlation coefficients between all microphones from the complete range of velocities.	115
8	Distances in meters from cross-correlations between all the microphones at a velocity of 10 meters per second in the test section.	116
9	Number of cells found in each geometry.	122
10	Average transmission losses for the corners.	134
11	Results of grid-convergence study for the corners.	134
12	Average transmission losses for the complete configuration. . . .	134
13	Results of grid-convergence study for the complete configuration.	134

1 Introduction

This master thesis projects presents the first steps made for the design of a new small wind tunnel for aeroacoustic measurements on the DTU Lyngby Campus. The new wind tunnel is intended to replace the old red wind tunnel located on the Lyngby Campus of DTU. Besides aeroacoustic measurements, the wind tunnel is also intended to be used for general educational purposes. Since resources are limited, the methods used in the design-process should be cost- and time-effective as well. Therefore, the first criteria for the new wind tunnel will be the re-use of the fan, inlet, and possibly the 4 screens of the old red wind tunnel that are located on the DTU Lyngby campus. The fan is an axial fan with a 42 kW drive-system. The fan has a diameter of 1 meter, a large hub with a diffuser at the outlet and the fan blades intersect the inner boundaries of the duct.

Other requirements for the wind tunnel were the dimensions of the test section with a width of 750 millimeters, a height of 500 millimeters and a length of 2000 millimeters. At the same time, the test section should be closed and have interchangeable walls depending on whether the experiment primarily has aerodynamics or acoustic purposes. Further criteria that were specified, include that the wind tunnel should have an open-circuit and be fitted in the same area as the old red wind tunnel is located now. The test section of the open red wind tunnel is located on the ground floor, whilst the fan-duct is located in the basement as can be seen in the schematic in Figure 1. This means, of course, that there are bends that direct the flow down as both the test section and fan-duct are placed horizontally. Even though there is a so-called elephant-hole between the ground floor and the basement present, that vents the excessive air from the basement up, there is no possibility of using a closed-circuit tunnel due to the fact that the elephant-hole and the hole that accommodates the duct leading the air downstairs are located too closely together. Accommodating the whole tunnel on the ground floor, which would imply elimination of bends, is impossible due to the lack of space.

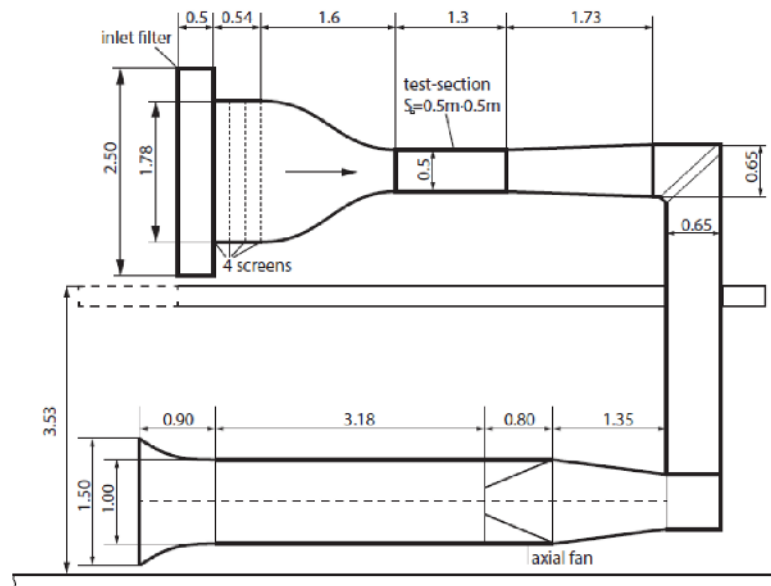


Figure 1: Schematic of the red wind tunnel located on the Lyngby DTU Campus.

2 Literature Study

2.1 Relevance of Aeroacoustic Research

The industry of renewable energy sources is becoming larger with new climate agreements. Wind energy is gaining in popularity and governments are widely investing in new large wind turbines and wind parks. Even small-scale private projects are started up more often than ever. At the same time, growing economies around the world are leading to more air-traffic. Activity around airports is rapidly increasing. Both air-traffic and wind energy produce aerodynamic noise, which falls right into the field of aeroacoustic studies.

(Janssen et al. 2010) compares two Swedish studies and one Dutch study about the annoyance and health effects of wind turbines on people. The paper reanalyzed the data of these three aforementioned studies and used the same methodology on each of them to reach a conclusion about health effects. The findings of the studies were consistent with each other and annoyance by wind turbine noise increased with the measure sound pressure levels. Increased sleep disturbance, stress and lowered well-being were found among the test subjects. (Boes et al. 2013) presents a study where noise measurements of flight operations at Zurich Airport are compared with medical data from residents at the same location. Here too, it indicates increased annoyance in the form of headaches and sleep disruption among the people that were included in the study. These findings are backed up by a literature study by (Kaltenbach et al. 2013), where 10 different studies are reviewed and noise is also associated with hypertension and decreased cognitive ability.

These examples of consequences by wind turbines and aircraft operations make aeroacoustics an interesting and desired field of studies. Comparing the studies presented at the first AIAA Aeroacoustic Conferences mid-20th century with topics of recent conferences, indicates that the focus in aeroacoustics has shifted from jet- and turbofan-noise to airframe-noise, annoyance and studies about noise and high-lift devices. This shift corresponds with the aforementioned developments in wind energy and increased airport operations.

2.2 Aeroacoustic Experiments

Most aeroacoustic experiments are conducted in wind tunnels as it offers a cheaper solution than field tests and the controlled environment allows to get a deeper understanding behind the physics of the noise. There are numerous fields of studies where anechoic wind tunnels can be applied to, such as airfoil studies presented by (Migliore & Oerlemans 2003) and (Lopes et al. 2006), for example, airframe noise and fields that are not related to the aerospace industry, like car acoustics and trains as suggested by (Brouwer 1997). Since this literature study will focus itself on the design of a small anechoic wind tunnel, it can be assumed

that the test section as well as the power source are of limited size. The latter may imply that flow velocities that can be attained would not be very high. With small models and low flow velocities, the Reynolds numbers that can be achieved in the test environment are not likely to exceed $5 \cdot 10^5$. Since real flows conditions are reconstructed in wind tunnels by merely altering the Mach and Reynolds number, the applications of a small wind tunnel will be limited (Anderson 2008). Because of the range of low Reynolds and Mach numbers, it could be used for model validation, tests on individual parts, (2D) airfoil measurements, natural flyers, unmanned aerial systems, some wind turbine applications and propellers (Selig et al. 2011).

2.3 Wind Tunnel Types for Aeroacoustic Measurements

(Glegg & Devenport 2017) distinguishes between three different types of anechoic wind tunnels by the kind of test section they have: Closed, open-jet and hybrid test sections.

2.3.1 Closed Test Section

The physics and interference of aerodynamics in closed test section are well-known and require few corrections. Acoustic measurements can be done by microphones in fairings that are placed in the flow area or those embedded in the wall of the test section. (Jaeger et al. 2000) found an improved method for reducing the flow interaction for embedded microphone array in the wall, by covering the cavities in which the arrays were placed with acoustically-transmissive Kevlar material. This material would allow the noise to pass, whilst it shielded the array from the flow. However, the noise of the boundary layer over the wall of the test section and reflections of the same solid walls are high, cause interference and may therefore spoil aeroacoustic measurements as shown in (Lv et al. 2018). (Soderman & Allen 2002) argues that anechoic wind tunnels with a closed test section require large dimensions where the noise can reach the far-field within the test section. Noise in the near-field, close to the source, is very different to noise from the far-field, which is most often the point of interest. It takes about one to two acoustic wavelengths for noise to reach the far-field.

2.3.2 Open-jet Test Section

Anechoic wind tunnels with an open-jet as a test section can avoid problems with reverberation spoiling the measurements what may happen when doing aeroacoustic measurements in wind tunnels with closed test sections. In anechoic open-jet wind tunnels, the flow from the contraction is directed into an anechoic chamber. The model will then be placed inside the jet that travels through the chamber, whilst microphone arrays can be placed outside of there in order to avoid any flow interaction. However, for the noise to reach the microphone array, it must travel through free shear layer of the flow, where effects like spectral broadening and refraction will play a role. Open-jet anechoic wind tunnels are

considered to be a good option for smaller wind tunnels as it is relatively easy to place a microphone array in the far-field with a sufficiently large anechoic chamber. Undesired noise may arise, however, from the interaction between the contraction nozzle or the collector and the flow.

Noise Refraction Noise from a source inside a jet will refract in the free shear layer and will leave the jet and enter the ambient air under a different angle than it came from. This refraction will pose problems when using the beamforming method, when using microphone arrays to identify noise sources on a body that is exposed to the flow of a jet. Since refraction, as well as the amplitude change through the free shear layer, is independent of frequency and thickness of the free shear layer, simple corrections, as presented by (Amiet 1975), can be done to account for this. When these corrections were validated by NASA, however, they were only valid for moderate angles between the source and the shear layer, noise entering the shear layer in the far-field and distances larger than one jet-radius between source and shear layer.

Spectral Broadening Spectral broadening is another effect that occurs when noise goes through the turbulent shear layer of an open-jet wind tunnel. As described in (Sijtsma et al. 2014), where a model is derived and validated to account for spectral broadening, spectral broadening is the scattering of peaks from tonal noise. This tonal noise inside the jet will be recorded as sound from a frequency-band in the ambient air of an open-jet wind tunnel. The extent of spectral broadening is dependent on flow velocity, noise frequency and the thickness of the shear layer.

Aerodynamic interference Besides the two aforementioned phenomena, aerodynamic interference effects are significant in open wind tunnels and therefore many corrections are required for aeroacoustic measurements in this type of wind tunnel. In some cases, depending on the model size and type, another series of aerodynamic measurements are required in another wind tunnel to account for the interference effects in aeroacoustic experiments as mentioned by (Soderman & Allen 2002).

2.3.3 Hybrid Test Section

The third type is a hybrid wind tunnel, where the hard walls of a closed test section are replaced by acoustic transmissive material. Such walls contain the air flow and therefore limit the amount of aerodynamic interference that is often found in open-jet wind tunnels. The Virginia Tech stability wind tunnel is an example of such a hybrid wind tunnel, where two of the hard test section walls are switched out with acoustic permeable Kevlar. The idea of an acoustic transparent wall was first tested by (Bauer 1976), where a perforated steel plate covered with a fine stainless-steel mesh was used as a substitute for a regular test section wall. One meter behind this wall, a microphone was placed that

only recorded a 1dB transmission loss from noise from the flow through the wall, while adverse effects of the free shear layer were prevented at the same time. (Jaeger et al. 2000) found in his study that Kevlar cloth was very much suited to shield microphones from the flow in hard-walled test sections and in contrast to the perforated plate from (Bauer 1976), it would not fail due to (metal) fatigueness. This study by (Jaeger et al. 2000) led to the Virginia Tech stability wind tunnel, where, as mentioned in the previous, Kevlar is stretched over large cut-outs in the wind tunnel walls, behind which microphone arrays are placed in anechoic chambers on either side. Since hybrid anechoic wind tunnels generally combine the benefits of the hard-walled and open-jet tunnels, they have gotten more popular recently. Other wind tunnels that make use of this configuration are the JAXA tunnel, the NSWCCD tunnel and the new Poul la Cour wind tunnel.

Because of material flexibility, resulting in deforming walls at the hand of the pressure distribution around the model placed inside the test section, and porosity (flow leakage), there will still be a need to account for aerodynamic interference as explained in (Remillieux et al. 2008). (Ito et al. 2008) showed that the aerodynamic corrections that are required for hybrid anechoic wind tunnels are less than the hard-walled and open-jet types. Simple CFD or panel-methods may assist in finding the right corrections to each situation. A downside of hybrid anechoic wind tunnels, is that the test section is relatively expensive. Acoustic transparent walls have high manufacturing costs and there is a special clamping system required in case Kevlar will be used as explained in (Remillieux et al. 2008) and (Devenport et al. 2017).

2.4 Aeroacoustic Measurements

(Soderman & Allen 2002) gives a good overview of common measurement techniques in wind tunnels. Acoustic measurements inside the wind tunnel can either be done by single microphones or a phased microphone array. Condenser microphones are commonly used in aeroacoustic experiments because of their reliability and characteristics. They can be selected upon their characteristics (e.g. microphone diameter) in order to have a specific frequency range or sensitivity. Electret microphones are a cheaper option, but require calibration for each new experiment.

It is recommended to keep microphones outside of the flow and as close as possible to the model at the same time in order to have the largest possible signal-to-noise ratio. At the same time the microphone should be placed in the acoustic far-field, approximately one wavelength away, in order to avoid contamination by pressure fluctuations (of turbulence) in the near-field. When microphones are placed inside an anechoic chamber, it is recommended to keep them one-quarter wavelength away from the wedge-tips. Keeping the microphone (array) out of the flow, prevents parasitic noise for when it would be

exposed directly to the flow. In some experiments, it may be required to expose microphones in the flow after all in order to get a better angle on a noise source. In such occasions, an aerodynamic fairing, which would minimize the amount of noise generated by the exposure, is required as well in order to boost this signal-to-noise ratio.

(Wagner 1996) is a book that functions as an introduction to wind turbine noise. Based on research conducted in the past, the book summarizes different types of aerodynamic noise and noise sources, which are not excluded to only wind turbine cases, but occur in most aerodynamic situations. It comes clearly forward that the intensity of aerodynamic noise is strongly dependent on the flow velocity and that turbulent fluctuations and the boundary layer are prominent noise sources. (Glegg & Devenport 2017) points out the importance of aerodynamic measurements in parallel with acoustic recordings during aeroacoustic experiments. In a study by (Kolb et al. 2007) to noise produced by 2D high-lift devices, aerodynamic properties were measured by pressure tabs and hot-wire anemometry. Aerodynamic measurements are both important for getting a better understanding of the physics behind the noise and corrections applied to the noise measurements during post-processing. In the ONERA CEPRA19 wind tunnel PIV is used as mentioned by (Piccin 2009).

2.5 Noise Sources of Wind Tunnels

(Soderman & Allen 2002) is a paper that discusses the acoustic characteristics of wind tunnels and aeroacoustic measurement techniques in wind tunnels. It states that the quality of acoustic measurements are highly dependent on the signal-to-noise ratio. It is said that the signal requires to be at least 6 dB larger than the background noise of the wind tunnel in order to retrieve accurate data from measurements, even though it is mentioned that (Jacob & Talotte 2000) presents a technique where aeroacoustic sound below the background level can be measured. (Soderman & Allen 2002) presents the drive fan, wall boundary layer, test supporting hardware and microphone self-noise as the four sources of wind tunnel background noise.

2.5.1 Fan and Drive-System

According to (Soderman & Allen 2002), the noise from a common axial drive fan is dominant in the low-frequency range, where the first two tone harmonics of the fan are usually highest. Just like for wind turbines, the noise and tones stems from the blade passage rate. Since best efficiencies of fans are attained at low RPM, the frequency of the tones are low as well. (Santana et al. 2014), a paper on the acoustic treatment of a wind tunnel at the university of Sao Paolo, and (Donald A. Dietrich & Abbott 1977), a study into the noise characteristics of axial fans by NASA, both confirm the dominance of the noise in the lower frequency range with their results of their own fan noise measurements during experiments. The first mentioned shows the first tonal peaks between 100 and

1000 Hertz and for the second study they are located between 0 and 2000 Hertz. (Donald A. Dietrich & Abbott 1977) showed furthermore that fan-noise is increased with increased inflow velocity and angle of attack, blade-loading and rotational speed.

2.5.2 Microphones and Microphone Arrays

Microphone self-noise is another source of background noise in wind tunnels. Microphones directly inserted into the flow, often the case with aeroacoustic measurements in wind tunnel with hard-walled test sections, are shielded from the total pressure by aerodynamic forebodies in order to expose it to just the static pressure. (Allen & Soderman 1993) is a study to a new design of such forebodies by NASA, where it is shown that the self-noise is specifically dominant below frequencies of 5kHz. From (Allen & Olsen 1998), a study into the effect of turbulence intensity on the self-noise of microphones, also by NASA, shows that the increase of turbulence intensity results in higher self-noise levels. The decrease of turbulence intensity from 1 percent to a tenth of a percent shows already a decrease of 20 dB in almost the complete audible spectrum for this study. In the previous, (Jaeger et al. 2000) was already mentioned, where a study to microphones attached or embedded in the wall are subjected to the boundary layer turbulence. Recessed microphones in this study show a decrease of almost 20 dB compared to flush mounted microphones between 2 kHz and 10 kHz.

In (Ross et al. 1983) microphone arrays for open-jet aeroacoustic wind tunnels were placed far away from the jet center-line and significant lower background noise was measured as there was, of course, no self-noise of the microphones as well as the nozzle and collector of the wind tunnel may have shielded the microphones from noise sources elsewhere in the wind tunnel duct, such as the fan. The anechoic chamber may play a role here too as there is sound absorption by the walls and therefore no reverberation.

2.5.3 Testing Hardware

Cables, probes, models, supports, corner vanes and other hardware that is exposed to the flow inside the wind tunnel duct, may also generate significant noise. (Williamson 1996) is a review on the vortex dynamics of cylinder wakes, where it is shown that wires and struts may cause aeolian tones from vortex shedding. The study (Hersh et al. 1974) shows that airfoils with specific shapes may generate noise in a similar fashion unless the boundary layer is tripped at the leading-edge.

2.5.4 boundary layer

The boundary layer inside the wind tunnel is another source of background noise in aeroacoustic experiments. According to (Grissom et al. 2006), where several

studies into boundary layer noise and new experiments into boundary layer noise are discussed, it is related to the wall roughness, but the precise mechanics behind the noise are relatively unknown. Three theories are mentioned in this paper, where either the noise stems from the unsteady fluctuations due to either the height elements or the number of roughness elements per unit area or it is described as dipoles sources as a result of the unsteady loading roughness elements are subjected.

In (Duell et al. 2004) the boundary layer background noise of different wind tunnels used in the automotive and aerospace industry are compared, discussed and used to validate a prediction model for boundary layer noise. From this study, it followed that boundary layer noise becomes dominant over fan-noise and other noise sources above 1000 Hertz at test section inflow velocities of 140 km/h. The dominance of boundary layer noise in the test section diminishes between 7 and 10 kHz in this study. boundary layer noise in hard-walled test sections reach sound levels up to 20 to 30 dB higher than open-jet wind tunnels at 1000 Hertz because of reverberance. In (Soderman et al. 2000), a study to the development of a new acoustic lining for the test section of the NASA 40-80 wind tunnel, background noise of the boundary layer lies roughly between 5 kHz and 10 kHz. In the same studies, a reduction in background noise below 5 kHz is attributed to a lower flow turbulence and above 5 kHz amongst others to a thinner boundary layer.

2.6 The Anechoic Environment

From papers on the design of new aeroacoustic testing facilities, such as (Mathew et al. 2005), (Winkler et al. 2007), (Pascioni et al. 2014) and (Devenport et al. 2017), the criteria on flow quality are presented as a maximum flow non-uniformity of 1 percent and a turbulence intensity below 0.1 percent. These numbers correspond with what is recommended in later mentioned papers dedicated to the design of regular wind tunnels such as (Jewel B. Barlow 1999) and (Mehta & Bredshaw 1979). From (Mehta & Bredshaw 1979) it also becomes evident that the flow quality is of great importance in aeroacoustic measurements as the effect of free-stream turbulence on the leading-edge of a test object may contaminate the results. Reduced flow uniformity may pose difficulties in placing models inside the test section, as well as the thickness of the shear layer will be increased for open-jet tunnels. (Glegg & Devenport 2017) writes that without clear knowledge of the flow quality, it would be a difficult task to put aeroacoustic measurements into perspective, understand the physics behind them and apply the required corrections for both the aerodynamics and the acoustics.

2.6.1 The Anechoic Chamber

An anechoic environment is key for conducting aeroacoustic measurements. For open-jet and hybrid anechoic wind tunnels, the microphone arrays are placed inside anechoic chambers, which are characterized by rock wool or polyurethane

wedges. The arrays are shielded from background noise and protected from noise reflections in this environment. In (Pascioni et al. 2014), a report on the construction of a new anechoic facility in Australia, it is recommended to have an airtight chamber and tightly packed wedges with tip-to-valley lengths of quarter of the wavelength that corresponds to the desired cut-off frequency.

2.6.2 Acoustic Lining

As was mentioned in the previous, the range of relevant frequencies that could be recorded during aeroacoustic experiments is large with scaled models and may also lie outside the audible spectrum of humans. The aforementioned self-noise sources of wind tunnels, emit noise within this relevant frequency range and may therefore spoil aeroacoustic measurements inside the test section. It is therefore also important that self-noise of the wind tunnel is limited and does not propagate to the test section. (Santana et al. 2014) states that rather than addressing all the noise sources individually, it is easier to prevent noise propagating towards the test section.

In (Leclercq et al. 2007) and (Pascioni et al. 2014), two papers on the design of new open-jet facilities, the fan-ducts are disconnected to the rest of the wind tunnel-duct to avoid further effects from vibrations generated by fan and motor. On top of that, the fan-ducts and motors are shielded with acoustic lining. In (Santana et al. 2014) acoustic improvements are done for a closed-circuit wind tunnel, where the ducts before and after the fan-section are equipped with acoustic lining. Diffusers are not given acoustic lining in order to avoid flow separation - With adverse pressure gradients already present, the roughness of the porous surface accompanied by such lining makes the flow more prone to separation. (Johansson 1992) uses a special dampening platform to place the complete motor-fan combination upon on top of it in order to avoid vibrations making finding their way to elsewhere in the tunnel-duct. The hub and the central aft-body of the fan are also lined with sound absorbing material in this study. Experiments with a new wedge-shaped acoustic lining from (Allen & Olsen 1998) show that low frequencies are generally well-absorbed by thick acoustic lining, but require a large thickness. mid- to high-range frequencies are absorbed less well in this study.

The protective layer of the lining, which can be a perforated or porous surface, affects the characteristics of the acoustic lining. In (Munjal 2014) it is shown that the porous surface affects the transmission loss of noise through the lining. A porosity of 20% does not change the characteristics of the lining in terms of transmission loss, whilst a 5% porosity increases its effect somewhat for the lower frequencies and has a poorer performance for a broad range of higher frequencies.

2.6.3 Fan Improvements

(Remillieux et al. 1986) makes use of a microphone array placed in front of the fan to identify the noise sources of the fan. It was found that tip-clearance between the fan-tips and the fan-duct is a prominent noise source and that extensions and fillings reduce the noise produced by the fan. Besides improving the inflow quality, as suggested by (Donald A. Dietrich & Abbott 1977), (Remillieux et al. 1986) also makes use of a low-rpm fan with high solidity and special designed aeroacoustic stator-vanes. (Soderman & Allen 2002) suggest the use of the M-H airfoil for stator-vanes and/or the support structure of the fan that is exposed to the flow.

2.6.4 Mufflers

(Santana et al. 2014) uses baffle mufflers to stop noise propagating towards the test section. In this study it is shown that it has particularly positive effects in the range above 4000 Hertz. Blockage will play a role, however, and pressure losses will be increased with this type of muffler. (Munjal 2014) states that baffle mufflers are particularly effective for lower frequencies. Together with the application acoustic lining on the tunnel walls, the sound pressure levels found in the test section were 5 dB lower in the study of (Santana et al. 2014). (Bergmann 2012) by the dnw institute in Braunschweig for improvements of the tunnel, uses thick corner-vanes with acoustic lining to stop noise from propagating further down the duct. Using thick vanes with long extensions is since recently a popular trend for new anechoic wind tunnels and will, amongst others, also be used for the new Poul La Cour wind tunnel at the Risø facility of DTU as shown in (Devenport et al. 2017). (Devenport et al. 2017) also mentions that corner-vanes, besides acting like a baffle muffler that is effective against lower frequencies, are also expected to be effective for absorbing higher frequencies because of their curvature. The acoustic performance of the corners is evaluated with an insertion loss model in (Devenport et al. 2017). In (Leclercq et al. 2007) and (Piccin 2009), two papers on the update of anechoic wind tunnels, there are silencers placed at the inlet of open-circuit wind tunnels. In these papers, the silencers are either straight vanes or baffle mufflers as described in the previous.

2.7 Wind Tunnel Design

(Mehta & Bredshaw 1979), (Bell & Mehta 1988*b*), (Jewel B. Barlow 1999) and (Bradshaw & Pankhurst 1964) are works that are dedicated to the design of low speed wind tunnels and are often referenced to in other papers on the construction of new low speed wind tunnels such as (Hernandez et al. 2013), where they were used for the design of wind tunnels for the Spanish national council of sports and the technical institute of renewable energy on Tenerife, for example. The aforementioned papers share recommendations for the sizing and design standard components of wind tunnels, which are the screens, honeycombs, settling chamber, contraction, test section, diffusers, corners and drive fan. From

the papers it becomes evident that in particular the contraction requires in the design process. Although, the diffusers and corners also deserve extra attention in the design process.

2.7.1 The Settling Chamber, Honeycomb Structure and Screens

According to (Mehta & Hoffmann 1986), an experimental investigation to the effect of screens on the flow, screens remove turbulence in the flow and improve flow uniformity by creating a static pressure drop. They are also a tool to reduce the boundary layer thickness in a wind tunnel. By refracting the flow through the screen to the local normal, the turbulence-intensity will be reduced in every direction. Screens with an open-area ratio of less than 0.5–0.6 produce an unstable flow, as random jets from the screen pores collide downstream. Currently, open-area ratios are $\beta \sim 0.6$ for wind tunnels.

Screens of the same solidity and shape are more effective with larger spacing of the wiring. Though, simulations in the study (Kulkarni et al. 2010) showed that wires require to have a Reynolds number of less than 50 in order to avoid vortex shedding. Combinations of screens in series, where the mesh becomes finer for every screen, have proven to be very effective in turbulence reduction. These effective combinations however, are at the cost of a higher power-factor/larger pressure loss of the wind tunnel.

Honeycomb structures in wind tunnels both suppress and generate turbulence in a wind tunnel flow and remove swirl. (Loerke & Nagib 1976) shows that the generated turbulence is a result of a laminar flow instability in the direct wake of the structure. The mechanics behind the turbulence generation of honeycomb structures is largely unknown and it is therefore hard to make any predictions on how self-turbulence will show itself for a given structure. (Scheiman & Brooks 1980) showed experimentally and (Kulkarni et al. 2010) numerically that the effectiveness of honeycombs structures can be increased by placing a fine-meshed screen downstream of the honeycomb. There is no clear method in predicting the effects of their configuration together. Honeycombs are especially effects against lateral turbulence, whilst screens are better for removing axial turbulence.

(Mehta & Bredshaw 1979) advises on how the honeycombs and screens are commonly implemented in the tunnel. The settling chamber usually houses the honeycomb structure and/or one or multiple screens. The spacing between the honeycombs and screens should be such that the pressure is fully recovered (i.e. the rate of change of pressure w.r.t. distance from the wall is zero) after the perturbation, before it reaches the next screen. This guarantees that the perturbations of each component are independent of each other. It has been shown that honeycomb/screen combinations with a spacing of 0.2 times the settling chamber diameter performs adequately. This is also the distance that

is suggested for letting the flow recover before it enters the contraction.

2.7.2 The Contraction

The contraction is one of the most important components of a wind tunnel and must be designed with care, as it directly determines the flow quality in the test section. From (Batchelor 1953) it was found that the contraction reduces turbulence and non-uniform flow components. The total pressure remains constant through the contraction and therefore mean and fluctuating velocities become a smaller fraction of the total velocity through the contraction.

(Mehta & Bredshaw 1979) argues that the contraction ratio should ideally be as large as possible, but there is a preferred ratio between 6 and 9. A too large contraction would result in very large dimensions of the inlet and flow noise. A contraction that is too small would result in large pressure losses in the settling chamber. The latter is a direct result of high flow velocities through the screens and honeycombs. The non-uniformities and longitudinal turbulence should be below 1% and non-uniformity should be below 0.5%. These numbers may be achieved with 2 or 3 screens in the settling chamber with such a contraction ratio.

Circular cross-sections are ideal for contractions as cross flows and boundary layer separation in corners are avoided. With the absence of boundary layer separation, the flows in the corners do not necessarily have any effect on the quality of the flow in the test section and remain localized according to (Su 1991). Cross flow-effects can be reduced by reducing asymmetry and reducing velocity extrema in the contraction. (Bell & Mehta 1988*b*) explains how separation occurs due to adverse pressure gradients along the walls of a cross-section. These adverse pressure gradients can be avoided by infinitely-long contractions, which is of course impossible. Because contractions require a finite length, adverse pressure gradients occur. Longer contractions would have less severe adverse pressure gradients and the flow would be less likely to separate, but because of the increased length of the contraction, the boundary layer may grow too much, resulting in a flow of poor quality through the test section. In general, boundary layers are less likely to separate at the contraction-exit due to an increased skin friction coefficient and the stabilizing convex wall-shape. The concave wall-shape at the inlet however, has a destabilizing effect on the boundary layer. Separation at the inlet can be avoided by having large contraction ratios, because of the strong flow acceleration that follows. Low curvature at the end of the contraction, reduces variations in axial velocity across the cross-section and chances on separation. Generally, it is advised to have both at the in- and outlet of the contraction low curvature, whilst there is a steep slope in the central region of the contraction to avoid negative consequences for the flow in the test section.

There are multiple methods to design a wind tunnel contraction. The most popular methods are solving the streamline equation for an axi-symmetric wind tunnel as presented in (Morel 1975), or, for square cross-sections, from (Bell & Mehta 1988a), using a fifth-order polynomial of which the first and second derivative are set to zero to guarantee a slope of zero at both ends of the contraction. For the polynomial method, there are variations to the polynomial presented by (Abbaspour & Shojaee 2009) that improve certain flow characteristics at the cost of other characteristics. Curves described by 3rd and 4th order polynomials may also result in adequate flow characteristics, but will be lesser (although simpler) options. Other methods are connecting two elliptical arcs as presented by (J. H. Downie 1984) or simulation driven design optimization by (Leifsson et al. 2012), for example, where a surrogate-based optimization for a contraction is done by using a lo-fi CFD model.

2.7.3 The Diffuser

As mentioned earlier, the diffuser is another important part of the wind tunnel. A wind tunnel may lose a lot of its efficiency if there is separation inside a diffuser. This is either the consequence of a too thick boundary layer entering the diffuser inlet or a too large divergence-angle. Wind tunnels often use multiple diffusers with moderate area-ratios and low expansion angles, in order to prevent separation due to adverse pressure gradients. The paper (Patterson 1938), a review of multiple papers on the design of diffusers, also saw separation happen often in long diffusers with very low expansion angles.

According to (Patterson 1938) and (Mehta & Bredshaw 1979) splitter plates or deflectors can eliminate the onset of boundary layer separation and reduce the boundary layer thickness by diverting flow from the core to the regions near the wall. Other effects are reducing flow asymmetry and unsteadiness and its drag and create a more uniform velocity profile. When these are implemented at the diffuser-exit, they may also bring velocity variations down from 30% to a mere 5%.

(Bradshaw & Pankhurst 1964) says that smaller expansion angles should be considered for diffusers for open-circuit wind tunnels as boundary layer thickness is relatively larger for these wind tunnels compared to closed-circuit tunnels as the length-to-diameter of the test sections of open-circuit wind tunnels are usually higher. As a result, a boundary layer is more likely to separate in a diffuser.

The optimum divergence angle for a diffuser is dependent on the cross-sectional shape. In (Patterson 1938) axi-symmetric diffusers are presented as the most efficient in terms of flow-expansion efficiency at the same rate of expansion and have an optimum expansion angle somewhere between 5° and 8°. For square cross-sections with two diverging walls this angle is 11° between them.

For square cross-sections throughout, this angle is 6° . The pressure of the flow continues to rise after the flow exits the diffuser. Depending on the divergence-angle of the diffuser, the pressure of the flow can continue to rise for about 2 to 6 times after exiting the diffuser. Depending on the turbulence of the flow at the inlet of the diffuser, a straight duct to settle after the diffuser can increase the efficiency of flow expansion from 5 to 17 percent. In general, the efficiency gain is decreased for larger area ratios. (Johansson 1992) mentions that square and symmetric diffusers are more efficient than those expanding over one plane.

2.7.4 Corner Vanes

(Mehta & Bredshaw 1979) presents a universal method of designing corner vanes from thin metal sheets. In common practice, the vanes are circular arcs with straight extensions at the outer end. The downstream end here is aligned with the duct, whilst the upstream end makes a 4° incidence angle with the flow. The arcs turn 86° in total. For very large wind tunnels however, airfoil shaped vanes are used instead. Even though these vanes could be applied in smaller wind tunnels too in order to reduce pressure losses by about 5 times according to (Sahlin & Johansson 1991), where a study was done to mimic the flow around a corner vane to that of an airfoil in the free stream at a low Reynolds number. An increase in the amount of vanes would decrease pressure losses, but increase friction losses.

Corners may contribute for more than 50% of the total pressure loss, of which the first two corners after the test section are most critical, in a wind tunnel and must therefore be designed with care. While the use of vanes ahead of the test section only improves the flow uniformity in the test section for about 10%, corner vanes after the test section increase the uniformity with 36% as shown in (Calautit et al. 2014). When vanes are used for both corners, the study showed that the uniformity may increase by 65%.

In order to build a more compact wind tunnel, expanding bends could be used, where the corners have wider areas at the outlet. Such corners would lower the criteria for the diffuser. It does require a more careful design of the vanes to guarantee in order to limit the increase of pressure losses, however. (Lindgren et al. 1998), a study to the performance of expanding bends, shows that three-dimensional secondary flow effects are limited if the expansion ratios are kept beneath 1.33. For expanding bends, the location of the vanes w.r.t. the tunnel walls and themselves differ to those of non-expanding bends. This means that an optimisation is required for the geometry of the corner vanes.

2.8 Conclusion and Discussion

From the consulted literature it becomes apparent that the design of a new wind tunnel is rather straightforward. So is applying the modifications that are required to make the wind tunnel fit for aeroacoustic measurements, unless

each noise source inside the wind tunnel is treated separately. It must be kept in mind, however, that most of the consulted literature regarded bigger and commercial projects, where the budgets are also larger. This has obviously consequences for this design process, as the availability of resources that can be used for the new small wind tunnel at DTU are clearly much lower.

When looking at both the given requirements for the new wind tunnel and the literature from this study, a hybrid wind tunnel would in the end be the best configuration. A hard-walled test section with the given requirements on the dimensions of the test section would likely be too small to produce quality results. Besides that, microphones would directly act as extra noise sources. An open-jet tunnel would require a large anechoic chamber, which will drive up costs and there is no guarantee that such a large and static room can be accommodated in the hall where the new wind tunnel will be placed. On top of that, it will be more difficult to conduct regular aerodynamic experiments with an open wind tunnel and the lay-out with the anechoic chamber may impose extra difficulties in accessing the testing area. In short, it is expected that a hybrid configuration will have a higher degree of convenience and has a higher potential to produce quality results.

Because of limited space, the wind tunnel is required to have two bends so the tunnel can make use of the space available on the ground floor and in the basement. From an aerodynamic perspective bends are not ideal and if there was a freedom of choice baffle mufflers would be a better option as, for example, baffle mufflers in (Santana et al. 2014) only resulted in a 2 percent performance loss. However, literature shows that acoustically lined bends are a solid method in stopping noise to propagate to the test section and these should be included in the design as bends are a necessity nevertheless. There will also be a silencer required at the inlet of the tunnel, but this will not be treated further in this study.

From the literature it also became evident that flow quality is key for both being able to understand the physics behind the acoustics and keep lower noise levels. Literature showed that the turbulence intensities found inside the test sections of several wind tunnels was between 0.1-0.3 percent. Flow non-uniformity was found to be below 1 percent. Not just the flow quality inside the test section matters, but also elsewhere in the tunnel. At the inlet of the fan in particular as a lowered quality of the inflow conditions for the fan can result in decreased efficiency and increased noise. Separation noise may propagate upstream and spoil measurements. Screens, aerodynamic stator fairings and blade-tip fills, as suggested in (Soderman & Allen 2002) and (Donald A. Dietrich & Abbott 1977), may improve inflow conditions for the fan. It may be required to have slightly diverging walls in the rather long test section in order to compensate for the boundary layer growth. In short, it can be concluded that the duct of the tunnel should have the focus first and that the initial task in designing

an anechoic wind tunnel is guaranteeing good flow conditions. Modifications to improve the anechoic environment and acoustic properties of the tunnel come in second and do not necessarily have to be included in the initial design process. They could easily be installed at a later stage.

With the limited resources, time and space at hand, common and proven techniques should be used as much as possible. This would mean following the recommendations for the design of all the wind tunnel parts. (Calautit et al. 2014), (Leifsson et al. 2012), (Johansson 1992) and (Bergmann 2012) present simulation-driven design of either wind tunnel parts or of the complete wind tunnel. Optimizing the corners and contraction numerically would be ideal, especially because of the asymmetrical contraction shape and the use of thick corner vanes, but, as said, it would be time consuming with writing code and besides that, for example, software, like MISES from MIT made by Drela for the optimization for wind tunnel vanes, is not widely available for use. CFD, as used by (Calautit et al. 2014) and (Bergmann 2012) however, can be very valuable within the design process by doing quick evaluations of the configuration. CFD would be a practical tool that can identify areas that deserve attention in the design and give an idea of the flow quality and characteristics that can be found in- and outside of the test section. All in all, it will help in preventing unforeseen things happening such as flow separation, rotation and so on.

The fan of the old wind tunnel, including the motor and the duct, are to be re-used for the new design. The settling chamber is to be re-used as well. Whether screens can be used for the new design, depend, as implied earlier, on the flow conditions that can be found inside the new duct as the current screen meshes may result in adverse effects. The 5th order polynomial-shape for the contraction is the more common and a more compact option compared to the shape presented by (J. H. Downie 1984). Space and costs should be prioritized over a potential loss in efficiency and increased pressure losses with the stronger curvature of the polynomial-shape. The design of the diffuser may not follow the recommendations from literature completely. In the previous, it was stated by (Patterson 1938) that symmetrical expansions are the most efficient. However, from (Johansson 1992) and (Wagner 1996) it is known that thick corner vanes can be considered as strongly cambered airfoils and that flow-induced noise increases with the fifth power of the flow velocity. Therefore the flow velocity, especially at the first corner, should be kept as low as possible. The diffusers, while honoring and staying below the recommended maximum expansion angles, cannot have symmetric expansions as the flow from a rectangular test section must be expanded to the circular cross-section of the fan-duct eventually and a large expansion over a limit length is desired before the first corner on top of that. With the general recommendations for corner vanes and their multiple roles in mind, they are together with the bends expected to be the most difficult parts of the wind tunnel to design and to eventually build at a later stage. Optimisation of corner vanes has already been determined to be out of the

scope of this project. Considering the resources available, construction and the desire to use thick vanes to control the noise, it is implied that a certain degree of simplicity is required and that trial-and-error, in order to see "what works", may be needed in the initial stages of designing the vanes and bends.

3 Outline and Research Statement

The methods from literature for sizing and shaping a regular wind tunnel as well as for the acoustic treatment of a wind tunnel are well-proven. Little simulation-driven design has been done for individual wind tunnel parts and complete tunnels in earlier studies. For the design of a small anechoic wind tunnel in this context, simulations of noise propagation could be an important factor for the acoustic treatment in this project. The research statement is therefore "*The Simulation-Driven Design of a Small Aeroacoustic Wind Tunnel*".

In this project, the sizing of wind tunnel parts and aerodynamic evaluation will be presented first. CATIA V5 will be used to create a concept of the wind tunnel design. The wind tunnel parts will be designed, sized and assembled following the recommendations from literature, while keeping aeroacoustic performance in the back of the head. These geometries could then be exported to an external application for CFD evaluations. The preferred application would be Ansys Fluent. Using this application would ease the process of evaluating geometries and whenever necessary, it will allow for quickly adjusting certain characteristics of the geometry to eventually find a final design of the wind tunnel that shows acceptable flow conditions. 2D simulations will primarily be done to evaluate the performance of the corners and its vanes before investing in 3D simulations, which would be used for evaluating the performance of the complete tunnel in terms of, amongst others, power required, pressure losses, flow uniformity and turbulence intensity. Furthermore, aerodynamically generated noise in the tunnel will be identified and could be done by the built-in methods of Fluent employing Lighthill's acoustic analogy and the data acquired from the 3D simulations. The CFD results will be limited to steady-state solutions. Even though transient solutions from Fluent would allow for finding spectra of (tonal) noise sources, generating the right input data for simulations, it would require a lot of time and (computational) resources to find such numbers. Not to mention that such simulations are only possible under a very limited set of conditions.

After aerodynamic analyses, acoustic measurements will be done on the current site of the red wind tunnel in order to find the noise spectra of the fan and the power-source that will both be re-used for the new wind tunnel. Additionally, any specifics of the noise propagation from the basement to the ground floor are sought after during these measurements - whether the noise would mostly propagate in through the wind tunnel or through the elephant hole in the current situation. At the same time, transmission loss through the corners will be predicted by doing simulations in Ansys Mechanical. The acoustic measurements and the prediction of the transmission losses will be put side to side in order to make a prediction about the acoustic environment inside the test section. This project will be concluded with a general conclusion and recommendations for future work.

4 Sizing of the Wind Tunnel

In this section, a conceptual design of the wind tunnel duct will be made. This model must be in line with the aforementioned criteria. The designs of a settling chamber, contraction, test section, two diffusers and two corners will be presented. The assembly of the components that will be designed in this section will be used for CFD simulations at a later stage to evaluate the performance of the wind tunnel design.

4.1 Settling Chamber

As mentioned in the previous, the screens of the old red wind tunnel, depending on their characteristics, will be re-used for the new aeroacoustic tunnel. The characteristics of these screens will not be evaluated and their effect will not be evaluated in this study, but the general effect on screens on the flow will be included in pressure loss estimations later on in this study. Also, the screens will not be taken into account for the CFD evaluations for the sake of simplicity. At this point, only the dimensions of the settling chamber will be determined. A spacing of 0.2 times the (hydraulic) diameter of the settling chamber is recommended by (Mehta & Bredshaw 1979). With a wall-height and width of 1.78 meter for a square cross-section, the length of the settling chamber is 0.356 meter long. It must be kept in mind that with the inclusion of screens, the settling chamber will increase in length as the flow needs to settle with approximately 0.2* times the hydraulic diameter of the settling chamber after each screen.

4.2 Contraction

With a square settling chamber and the rectangular test section, the contraction will have an aspect-ratio. A contraction with cross-sectional dissimilarity may have some disadvantages - The aspect-ratio does make the flow more two-dimensional and flow-extrema will be increased on the narrow side, whilst they are decreased on the wide side. These effects mostly appear in the corners of the cross-section from a study by (J. H. Downie 1984).

The most straightforward and mentioned method to design the contraction, is following the curve of a polynomial of the fifth order as it is a good compromise that minimises the chances of separation occurring over the curves and is compact at the same time. The cross-section of both the settling chamber and test section have surface areas that were determined to be 3.1684 m^2 and 0.375 m^2 , respectively. These areas result in a contraction ratio of 8.45. The same literature that recommended the fifth-order polynomial method to design the contraction, also recommended an optimum contraction ratio that lies between 8 and 9.

Besides changing the surface area of the duct, the contraction also acts as a

transition from a square cross-section to a rectangular shape. The application of the fifth-order method in this project will therefore differ somewhat from the (axi-)symmetric cases widely presented in the literature. Since both the cross-sections are symmetric about the horizontal- and vertical-axis, a diagonal from one corner of the square cross-section to the closest corner of the rectangular cross-section will have the shape of the fifth-order polynomial. This approach acts as a compromise of the polynomial shape between the vertical and horizontal sides of the contraction. With sides a of the square cross-section and width b and height h from the rectangular cross-section, the envelope of the polynomial then must have a "height" h_p that can be calculated with Equation 1 as followed

$$h_p = \sqrt{\left(\frac{1}{2}(a-b)\right)^2 + \left(\frac{1}{2}(a-c)\right)^2} \quad (1)$$

Resulting in a height of 0.8215 *meter* for h_p .

As mentioned in the previous, the contraction shape can be found by using a fifth-order polynomial fit. The conditions of both ends are known: Both ends are clamped (second-order derivative is 0), with zero slope (first-order derivatives are 0) and the ends lie at 0 and h_p height. From Equations 2, 3 and 4, the first step in finding the coefficients for the polynomial can be found. In Equation 4 it can be seen that the first 3 terms are nonzero and the last three disappear.

$$y = x^5 + x^4 + x^3 + x^2 + x + C = 0 \quad \text{or} \quad h_p \quad (2)$$

$$\dot{y} = 5x^4 + 4x^3 + 3x^2 + 2x + 1 = 0 \quad (3)$$

$$\ddot{y} = 20x^3 + 12x^2 + 6x + 2 = 0 \quad (4)$$

The coefficients of the polynomial can be found by taking the cross-product of the first 3 terms of Equations 2, 3 and 4, which results into Equation 5.

$$h = 6x^5 - 15x^4 + 10x^3 \quad (5)$$

The envelope of the polynomial was determined by a discretization between the numbers 0 and 1 of 100 steps first. This vector for x as well as the outcome for h , can be multiplied by x_s and h_s , respectively, to find the exact coordinates of the envelope. In Figure 2 the polynomial can be seen. In Figure 3 and 4, the first- and second-order derivatives, respectively, of the polynomial are shown.

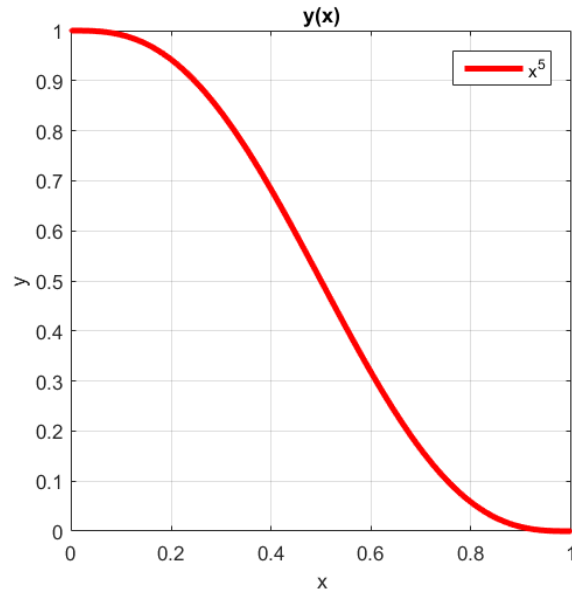


Figure 2: Fifth-order polynomial for the shape of the contraction edges (from MatLab).

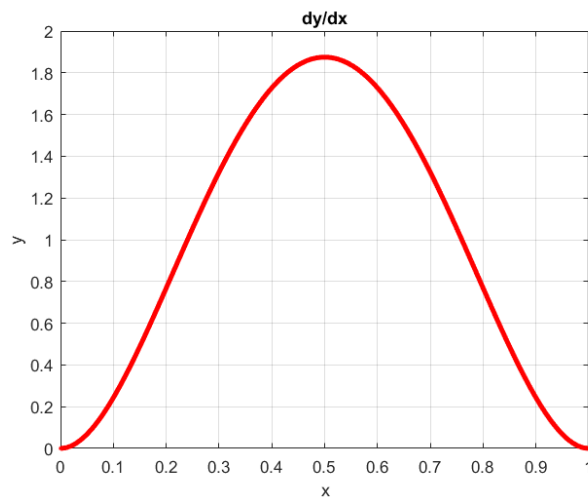


Figure 3: First-order derivative of the polynomial (from MatLab).

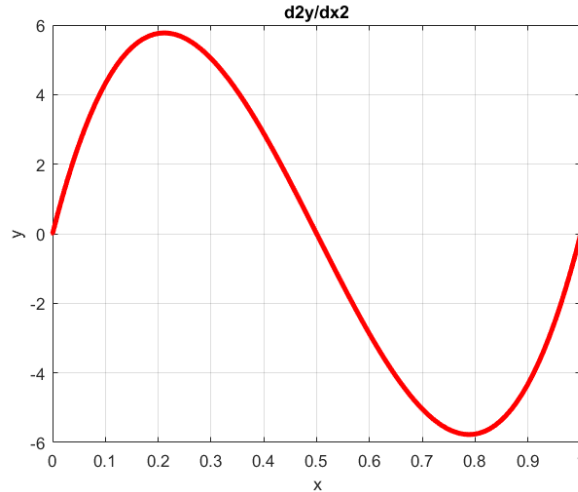


Figure 4: Second-order derivative of the polynomial (from MatLab).

In Figures 2, 3 and 4 it can be seen that the maximum slope is halfway through the contraction, the outer-ends do not have a slope and they are clamped and maximum curvature is just after and before, the contraction-inlet and outlet, respectively. The next step in the contraction design is determining the coordinates of the edges of the contraction in a $3D$ domain. This can be done by taking the sine and cosine of the angle the edges make with the vertical-axis of one of the cross-sectional planes. In the $3D$ domain, the x coordinates of the polynomial become the z coordinates. h_p can be decomposed into x and y coordinates as shown in Equations 6 and 7.

$$x = h \cdot \sin\left(\tan\left(\frac{1}{2}\left(\frac{a-b}{a-h}\right)\right)\right) - C \quad (6)$$

$$y = h \cdot \cos\left(\tan\left(\frac{1}{2}\left(\frac{a-b}{a-h}\right)\right)\right) - K \quad (7)$$

For Equations 6 and 7, the signs change depending on which corners of the square and rectangular cross-sections on the xy -plane the polynomial connects. Constants C and K indicate the coordinates of the corners of the square cross-section. For C as well as K , these values can be either -0.89 or 0.89 meter. In Figure 5 the shape of the contraction in a $3D$ domain can be seen. x_p is chosen to be 1.60 , which makes the contraction-length $.160$ meter and gives a 0.89 factor when it is divided by the side-length of the contraction-inlet. A factor between 0.667 and 1.79 is recommended in order to either avoid separation due to strong curvature or growth of the boundary layer as mentioned by (Bell & Mehta 1988a). The contraction is therefore rather short, which was mostly done in order to save space at the place where it is located.

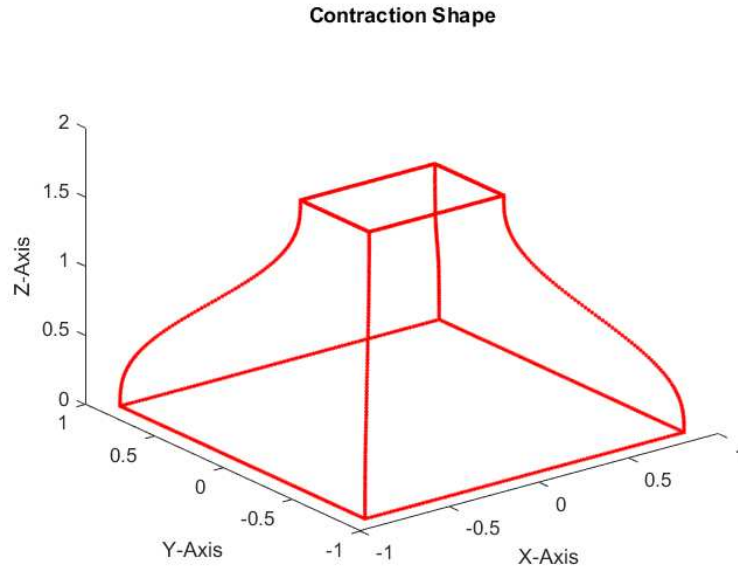


Figure 5: Shape of the contraction in a 3D domain (from MatLab).

For the sake of flow uniformity, a duct with a length of 0.2 times the width of the cross-section at the contraction-inlet is placed between the contraction-exit and the start of the test section to let the flow settle. This helps the flow settle to a uniform velocity-profile and pressure distribution in the test section and is recommended by (Mehta & Bredshaw 1979).

4.3 test section

The preferred dimensions of the test section were $2 \times 0.5 \times 0.75$ meter. This results in a cross-sectional area of 0.375 m^2 . It is suggested that the cross-sectional area of the fan should be about 2 to 3 times as large as the cross-section of the test section according to (Bradshaw & Pankhurst 1964). A too small area-ratio would require a high rotational speed of the fan resulting in more vibrations (and therefore more noise) and implies increased overall dimensions of the wind tunnel, whilst a too large ratio would result in turbulence and a poor velocity-profile at the fan-inlet (which implies a worse fan efficiency). With a fan area of 0.785 meter, this would result in a ratio of 2.09. A ratio of 2 is recommended to keep the wind tunnel dimensions small.

The hydraulic diameter of the test section can be determined by Equation 8

$$D_h = 2 \frac{ab}{a+b} \quad (8)$$

With $a = 0.50$ and $b = 0.75$, the hydraulic diameter becomes 0.60 meter. It is recommended that the length of the test section is kept between 0.5 and 3 times the hydraulic diameter in order to let the flow from the contraction recover and become uniform over a minimal length and avoid severe boundary layer growth and/or flow separation in the test section according to (Jewel B. Barlow 1999). With a test section length of 2 meter, the test section is 3.33 times the hydraulic diameter. And 4 times if the duct between the contraction and the test section is taken into account as well. It may therefore be necessary to have slightly diverging walls in the test section on the narrow side. Whether such measures must be taken for the wind tunnel design, should become evident by CFD later on.

4.4 Diffuser

Even though it is desired to keep the wind tunnel dimensions limited, the diffuser and maximum expansion angles, as well as the fact that the available area for placing the wind tunnel is divided between two floor-levels, limit possibilities of keeping the tunnel compact. Since the corners of the wind tunnel will have guide-vanes, it is important that the flow is sufficiently expanded before it reaches these vanes in order to limit the self-noise and spoiling future noise-measurements as a consequence. Besides that, significant pressure losses may occur in the corners with a high flow-velocity. With an area of 0.785 m^2 for the fan-inlet, it means that the duct, before changing the cross-sectional shape from square to circular, will have sides with a width of 0.886 meter.

In (Wagner 1996) it is mentioned that sound power levels increases with a factor of the fifth-order of flow velocity. It is assumed that 60% of the flow-velocity in the test section at the start of the first corner is enough to keep the self-noise (and also pressure losses) sufficiently low. From continuity, the area of the diffuser-exit should then be 0.625 m^2 , if the test section dimensions are 0.50 meter in height 0.75 meter in width. From literature, such as (Mehta & Bredshaw 1979) and (Patterson 1938), the most efficient expansion angles for diffusers range between 6 and 11 for square and rectangular ducts. From quick 2D CFD evaluations and trial and error at a later stage in this project, however, it became evident that the maximum expansion angle for the ducts was about 6 degrees only. In order to reach an area of 0.625 m^2 , the wide side of the test section expanded to a width of 0.8862 meter, whilst the narrow side expanded to a height of 0.705 meter. This results in a length of 1.950 meters for the first diffuser with an expansion angle of 6 degrees on the narrow side. On the wide side, it resulted in an expansion angle of 3.995 degrees.

The second diffuser lies between the first and the second corner and has a length of 2.2 meters. The second diffuser is placed vertically and the length of 2.2 meters guarantees that the test section has a sufficient height to do experiments and work with models inside. The second diffuser only expands two opposing

walls from a width of 0.705 meter to 0.886 meter. This results in an expansion angle of 4.72 degrees.

4.5 Corners and Corner Vanes

The design of the corners and the corner-vanes for this wind tunnel were inspired by the German WindGuard wind tunnel. Rather than a 90 degree bend, the corners consist out of two 45 degree bend with a straight part in between. This does not necessarily have any direct aerodynamic advantages, but it does simplify manufacturing and the addition of acoustic lining at a later point in the designing process. Additionally, no impermeable boundary to prevent the flow from leaking through the porous lining would be needed for the vanes. The corners play an important role in noise propagation and the design of them is, amongst others, a trade-off between aerodynamic and acoustic characteristics.

The design of the corners, together with its vanes, was mostly a trial-and-error approach, where the configuration of the corners were modified at the hand of the results from quick 2D CFD evaluations of the whole wind tunnel configuration. The setup of the 2D CFD simulations and the final results will be discussed later in Section 5.5. While the length of the straight connection between the two bends of each corner was kept at 300 millimeters, the radii of the first and second bend of each corner, which correspond with the center-line of the leading- and trailing-edge of the corner-vanes, respectively, were varied until CFD results did not show any severe flow distortion or separation for different flow velocities. This generally meant increasing the radius of the second bend of each corner, adjusting the first bend-radius so that it would follow the streamlines of the flow and fitting half of an ellipse, where the major-axis is approximately six times the length of the minor-axis, as a leading-edge. This was done to get an airfoil-shape for the corner vanes as recommended by (Johansson 1992). The ellipse was made by a standard ellipse shaper-function within the sketch-environment of CATIA V5. The co-vertices were tangent to and coincided with the two arcs of the first bend of the vane. The vertex was placed on the center-line/chord of the vane and its position was fixed within the tunnel-corner by coinciding this point on the straight construction-line that connected the start of the first inner-bend with the first outer-bend. The minor-axis of this ellipse-shaped leading-edge tilted because of the sketch constraints it was subjected to. Giving this axis a length that equals the vane-thickness (30 and 60 millimeter for the vanes in the first and second corner respectively) proved to work properly during CFD simulations. For the trailing-edge, the two arcs tangent to their respective wall of the vane met on the construction line between the two ends of the second inner- and outer-bend.

The dimensions of the first corner-inlet and - outlet were 0.886 meter in width and 0.705 meter in height. For the first corner, a thickness of 30 millimeters for the corner vanes gave good aerodynamic results. The first bend of 45 degrees

had a radius of 210 millimeter and for the second bend it was 350 millimeter. As mentioned in the previous, the bends were connection by a straight wall of 300 millimeter in between. The first inner-bend is tangent with the wall-angle of the first diffuser and therefore the angle is only 42 degrees, whilst there is a 42.65 degree angle between the second inner-bend and the second diffuser. The straight outer-walls before the first bend and after the second bend are connected by an angle that is equal to the wall-angle of the first and second diffuser, respectively. The vane-spacing (wall-to-wall) in the first corner is 98 millimeter with 7 vanes in total.

The second corner was designed similarly to the first corner. The in- and outlet dimensions were 0.886 meter for both the width and height. The radii of the first and second bends were 320 and 540 millimeter, respectively. The thickness of the vanes was doubled w.r.t. the first corner to 60 millimeters. At the end of the second diffuser the velocity of the flow is approximately 48% of the flow velocity in the test section. self-noise would therefore be less significant and the aerodynamic distortion, because of a greater thickness, is unlikely to affect the flow quality in the test section significantly so far downstream. The first inner-bend of the second corner is tangent with the wall-angle of 2.35 degrees of the second diffuser and therefore the bend only makes a total angle of 42.65 degrees. The three other bends of the corner make a 45 degree angle between the straight walls they are located. The outer-wall of the second-corner at the inlet makes a 2.35 degree angle with the outlet of the second diffuser. The vane-spacing of the second corner is 96 millimeter with 7 vanes in total.

The second corner is followed by a straight duct with a square cross-section. The sides are 0.886 meter in width and the length of the duct is 0.6 times the width of the cross-section. This part was included to improve the flow conditions at the outlet for better CFD results. Ansys Fluent may experience trouble with converging when there are a lot of flow irregularities and distortion at the outlet of the flow-domain. The factor of 0.6 is rather arbitrary, but assumed to be high enough to not let the flow distortion at the corner affect the conditions at the outlet. For the final design, this part of the tunnel should be a gradual change from the square cross-section to the circular cross-section with a diameter of 1 meter that matches the fan-duct. For now, this cross-section is kept as a square for the sake of simplicity during the CFD simulations. Figure 6 and 7 are side-views of the first and second corner, respectively. Figure 8 and 9 present their respective vanes. Figure 10 shows the assembly of all the wind tunnel parts. With the dimensions shown in Figure 11, the test section of the new tunnel would approximately be at chest-height on the ground floor.

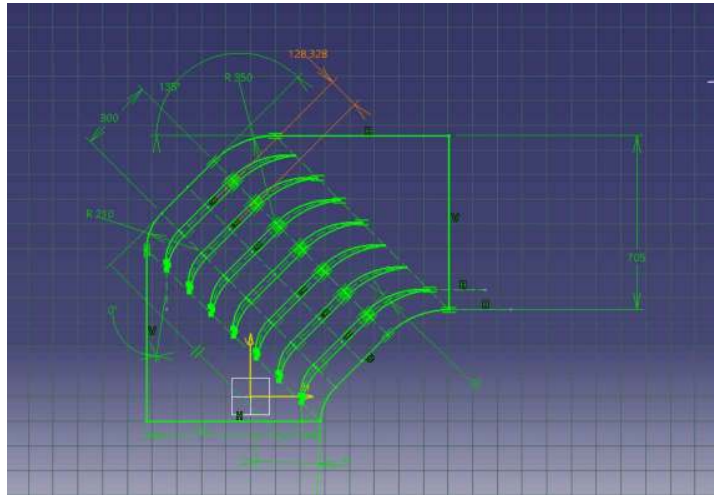


Figure 6: Sketch of the side-view of the first wind tunnel corner with constraints (from CATIA V5).

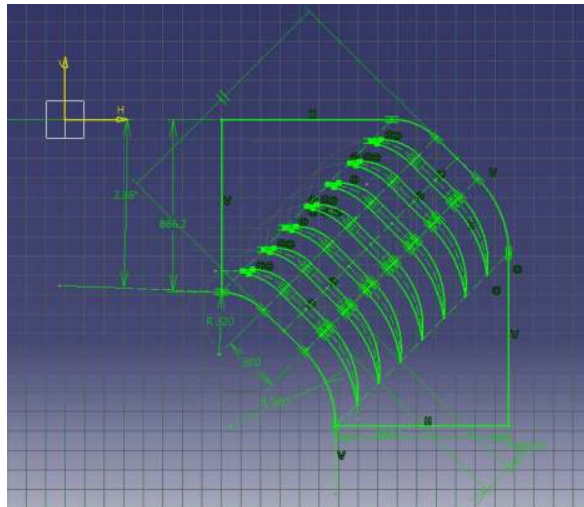


Figure 7: Sketch of the side-view of the second wind tunnel corner with constraints (from CATIA V5).

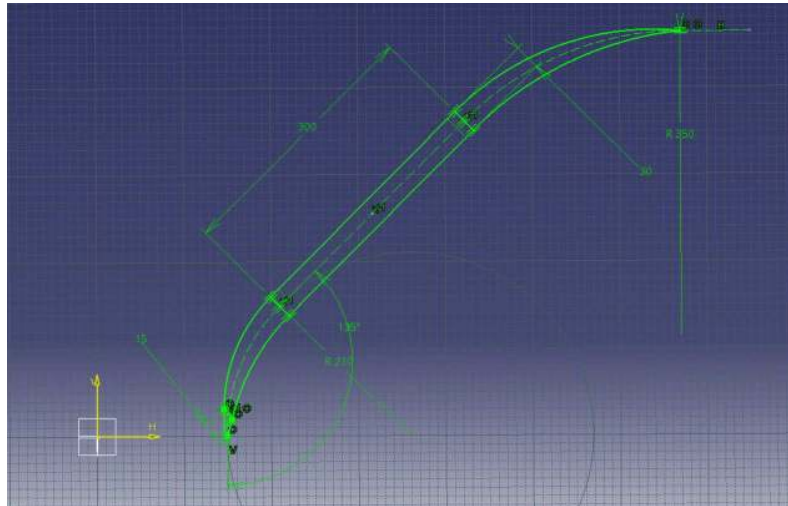


Figure 8: Sketch of the side-view of the first corner-vane with constraints (from CATIA V5).

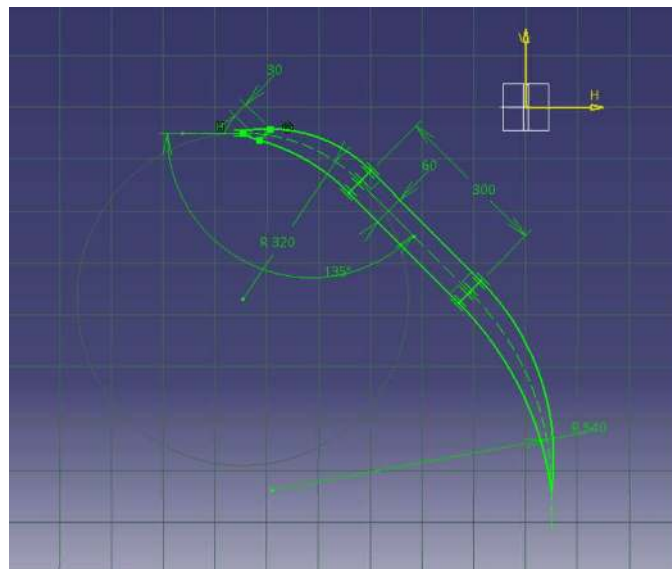


Figure 9: Sketch of the side-view of the second corner-vane with constraints (from CATIA V5).

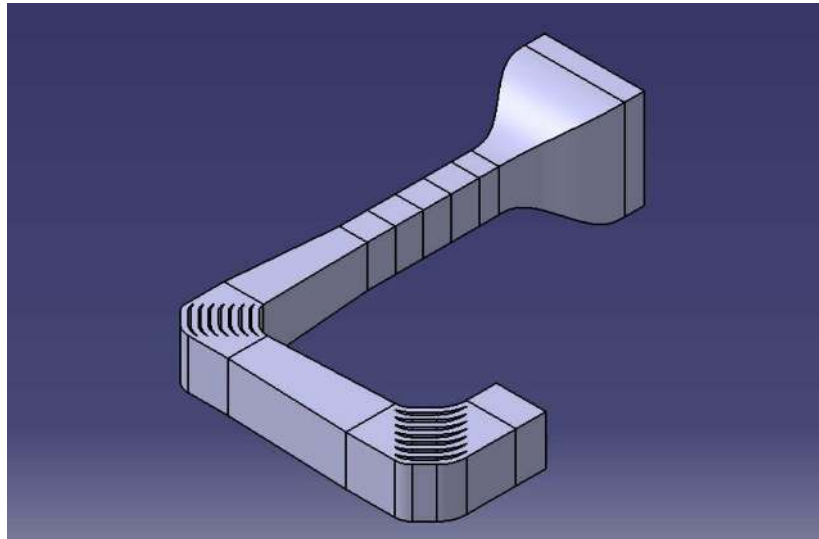


Figure 10: Assembly of the wind tunnel parts (from CATIA V5).

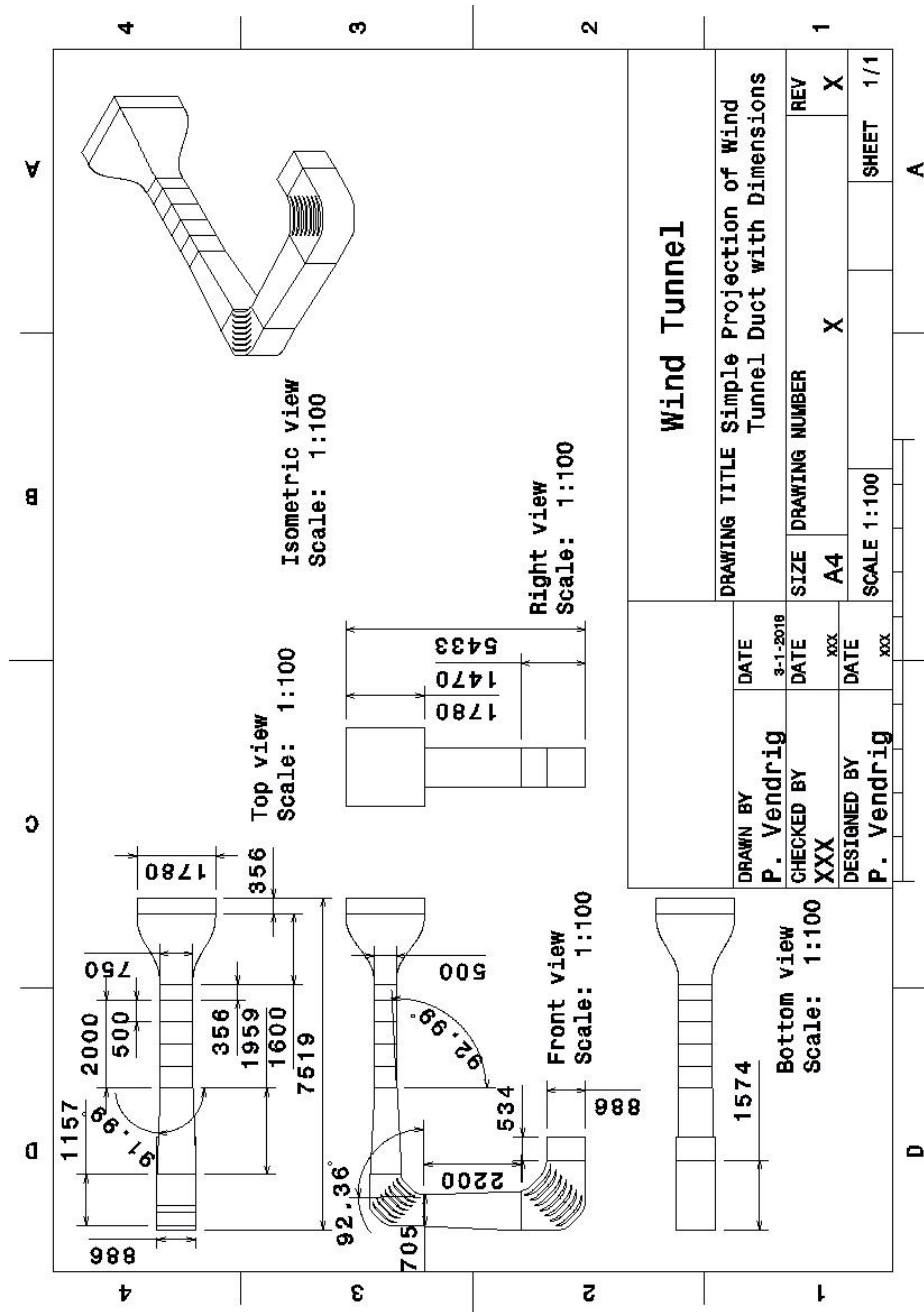


Figure 11: A simple American-projection with dimensions of the wind tunnel contours (from CATIA V5).

5 2D CFD Evaluations

2D CFD evaluations were used to investigate the flow through the conceptual design of the wind tunnel from the settling chamber to the inlet of the fan-duct. From the 2D evaluation it should become evident whether the tunnel can achieve acceptable flow conditions for experiments in the future. This mostly means preventing separation, investigate the effects of the corner-vanes on the flow and attain good levels of flow uniformity inside the test section. For these evaluations, Fluent of Ansys 18.0 was used.

These CFD evaluations were divided up in two stages: The first part used quick evaluations to determine the average flow velocity found in the test section as a result from the pressure difference between the inlet and outlet of the duct. These evaluations were also used to investigate the influence of the corner shape and corner vanes on the flow quality. The wall treatment in Fluent was helpful here, as they allowed the cell count of the mesh, and therefore the computational effort, low. In the second part the complete boundary layer was resolved throughout the duct for the lower and upper velocity limit as determined in the previous. These evaluations were expected to show boundary layer growth and whether separation would occur in the wind tunnel more precisely. For all the simulations, simulations are run again with a refined grid in order to find out whether the solutions are grid-dependent or not.

The following sections will give insight in importing the geometry in Ansys, meshing and solver settings. Whereafter the 2D CFD results are shown and discussed.

5.1 Geometry

For the 2D evaluations, a section-cut of the wind tunnel model on the symmetry-plane was made in CATIA V5. The test section of the conceptual design was divided up in four equal parts of 0.5 meter in length before that, in order to help setting up the simulation. The section-cut contained only the contour lines of the geometry and the separation lines of the different components in a sketch. For use later on in Ansys as a zero thickness model, fills were added to create faces along the complete geometry. The model was then exported to Ansys. In Figure 12, the geometry is shown as it is displayed in the design modeler. It can clearly be seen that the components that were designed in the previous section match with the faces of the model and are divided by edges. The inlet, outlet and all the other edges that separated the different components received named selections that would simplify meshing and setting up the solver at a later stage.

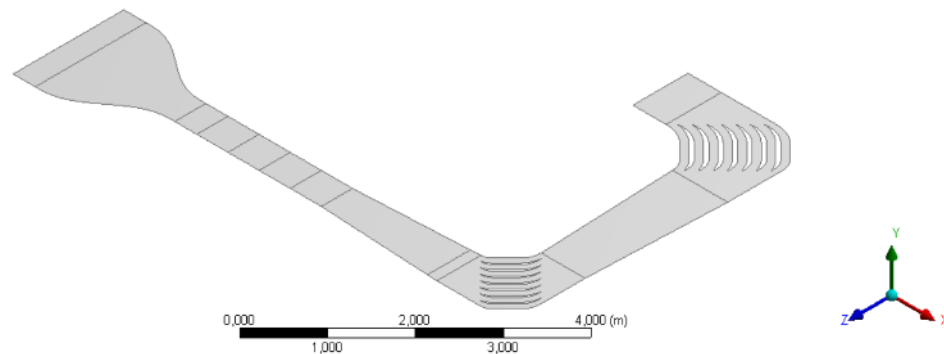


Figure 12: Zero-thickness model of the wind tunnel geometry (from Ansys).

5.2 Meshing

The next step was importing the geometry in the standard mesher of Ansys. Here virtual topology was used to join multiple discontinued edges of each single component. The curved contours of, for example, the contraction and the corner-vanes consisted out of multiple (straight) edges, that were joined to one single edge, which was done for the sake of simplicity in meshing and using the solver as well. Actual meshing was the next task. Since there were different evaluations, the meshes required different criteria. Therefore, there should be an idea of the expected flow velocities that can be attained in the test section of the new wind tunnel with the current power source and fan.

5.2.1 Flow Regime and Wall Distance

Currently, the red wind tunnel at DTU can achieve a flow velocity of 65 meters per second in the test section, where the surface area of the cross-section is 0.25 square meters. Since the cross-sectional area of the new wind tunnel is supposed to be 0.375 meters squared, continuity tells that the maximum speed should theoretically be 43.3 meters per second. With some margin, it is assumed that a flow velocity of 50 meters per second can be achieved. The lower velocity limit is set to approximately 10 meters per second. The lower limit is rather arbitrary and merely used to evaluate performance at low flow velocities.

There is no such thing as creating the perfect mesh and it is rather a trade-off between different criteria to reach an acceptable solution to the problem. First of all, the mesh needs to fulfill the requirements of the model in terms of wall

distance in order to find an accurate solution. A turbulent boundary layer can be divided up into three regimes: the viscous sub-layer, the buffer layer and the log-law layer. Moving away from the object placed in a turbulent flow, these regimes follow each other up in the same order they have been mentioned, until the log-law regime transitions to the free-stream region. The distance away from the wall to which each region extends can be expressed in the non-dimensional wall-distance y^+ . The non-dimensional wall-distance can be calculated by using Equations 9 through 12.

$$C_f = (2\log_{10}(Re) - 0.65)^{-2.3} \quad \text{for } Re < 10^9 \quad (9)$$

$$\tau_w = \frac{1}{2}C_f\rho v^2 \quad (10)$$

$$u_* = \sqrt{\frac{\tau_w}{\rho}} \quad (11)$$

$$y = \frac{y^+\mu}{\rho u_*} \quad (12)$$

Where C_f is the skin-friction coefficient, τ_w is the wall shear stress, u_* is the friction velocity and y the wall-distance.

5.2.2 The Turbulent boundary layer

The viscous sub-layer, also called the laminar layer, goes according to turbulence theory from the wall, where both the flow velocity (zero-slip) and the non-dimensional wall-distance are zero, to about a wall-height where y^+ is 5. From here on the boundary layer moves into the region of the buffer layer, where the flow is not fully turbulent yet. This region is where the transition from laminar to turbulent flow takes place and when the flow is fully turbulent, the logarithmic layer starts. This region lies between a y^+ of 30 and 300. In turbulence theory the upper limit of this layer is not set and depends on the flow characteristics. The logarithmic layer extends as far as where the log-law still governs the flow characteristics better than the free-stream properties, which can even be up to the point where y^+ lies around 500 or more as stated in (Sumer 2003). In Fluent however, this is set upper-limit is set to 300 according to the Fluent User's Guide.

The SST $k - \omega$ model can be used to solve the complete flow field. This, however, requires a y^+ of at least 1 for the cell at the wall together with a slow cell growth-rate in order to capture all the four regimes accurately. This results in a very fine mesh and the cell count would bring up the computational effort greatly. This cell number can be brought down by using the wall treatment that the $k - \omega$ models in Fluent have by default. Fluent provides a y^+ -insensitive wall treatment for all the $k - \omega$ models. This wall treatment will be discussed in greater detail later on in the project. This wall treatment means also that

the mesh can be used safely for a range of velocities and would make a grid-convergence study easier.

5.2.3 Application for Meshing

The Ansys Mesher was used to mesh the section-cut. The built-in mesher of Ansys was preferred over block-meshing in programs such as ICEM CFD, because of its user-friendliness and the ease of generating and changing a proper mesh quickly for a relatively complex geometry. The mesh was unstructured, because of the complex geometry. It was also believed that a structured mesh was not per se needed to get a converged solution.

5.2.4 Mesh for Case with Wall Treatment

From inlet to outlet, the walls of the geometry were divided up in parts of 0.0125 meter in length. This was a soft edge-sizing constraint, meaning that these divisions could become finer near the curvature and corners of, for example, the corners vanes and the angle the diffusers make with straight walls. This constraint was put in place in order to have a smoother transition (volume wise) between the inflation-layer and the triangles of the mesh. An inflation of twelve layers was created, where the first layer-height was 0.0007 meter from inlet until the end of the test section, 0.001 meter from the first diffuser until the first corner and 0.0013 meter from the second diffuser until the outlet. The growth-rate through the inflation-layers was set to 1.1. Even though the wall treatment is insensitive to the wall-distance, the inflation-layer was set up in such a manner that the cells adjacent to the wall lied between about 30 and 100 for the velocity range that was discussed in the previous. For the lower-limit of the velocity range, the ten of the twelve layers fell within a y^+ value of 300 as recommended by Fluent. The number that covers the boundary layer would become less with increasing flow velocity. The decision to not follow up on the ten-layer recommendation by the Fluent User's Guide for the higher velocities was made, since it would result in a drastic increase of the number of cells for the mesh. The cell-count would approach numbers for the meshes where no wall treatment would be used and because of computational effort, part of the purpose of this series of simulations would be lost. The numbers of y^+ corresponding with first-layer height are expected to be lower, because of the velocity-gradient near the wall. The theoretical values should therefore be a safe approximation. Twelve layers in combination with the other settings, gave size-wise a smooth transition between the inflation-layer and the unstructured mesh. In the end, a triangle-method was selected for meshing this geometry. Figures 13, 14, 15 and 16, show screen captures of the mesh of the complete wind tunnel, first corner, a corner-vane in the first corner and of the wall at outlet of the contraction, respectively. The limited amount of cells that make up the inflation-layer can be seen very in these figures.

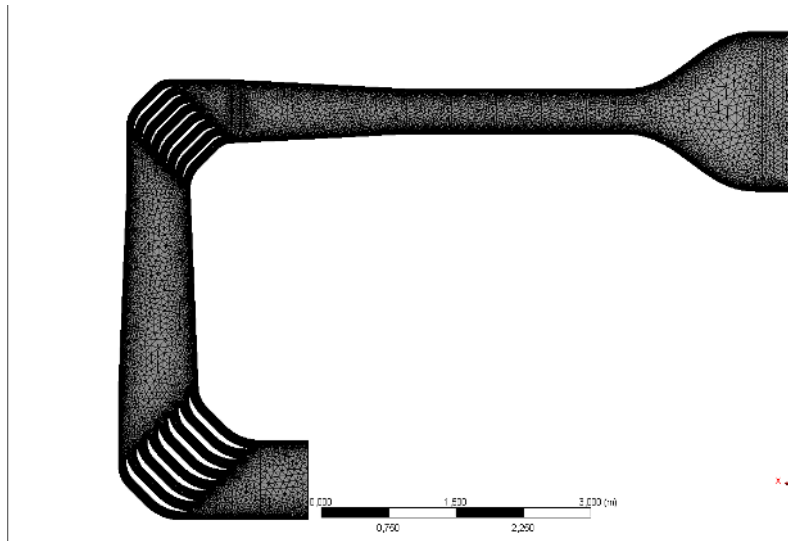


Figure 13: Mesh of the zero-thickness model of the wind tunnel (from Ansys Fluent).

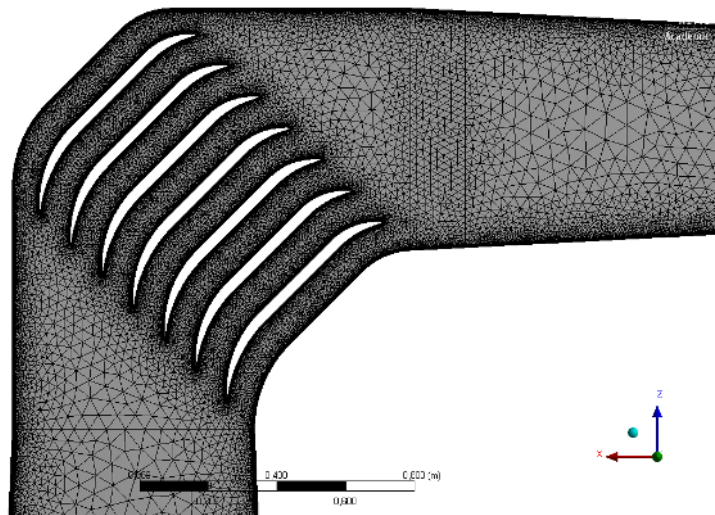


Figure 14: Mesh of the zero-thickness model of the wind tunnel at the first corner (from Ansys Fluent).

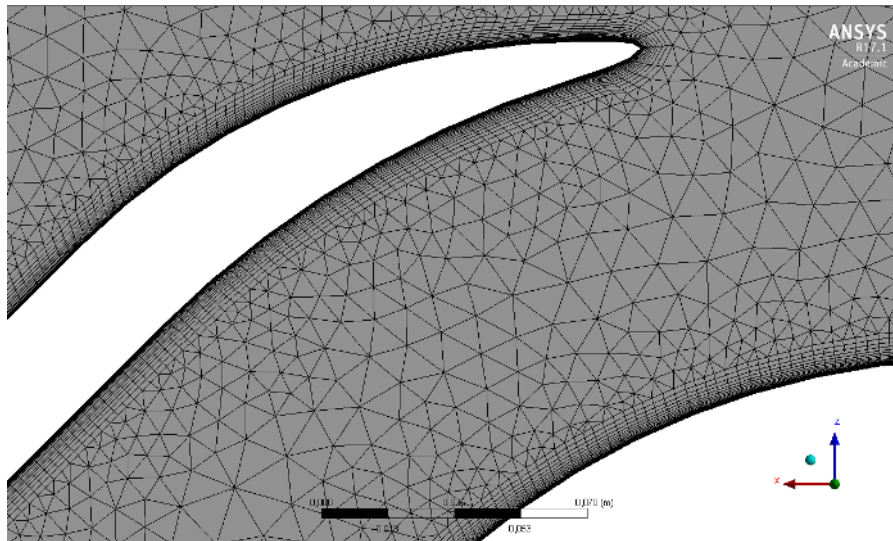


Figure 15: Mesh of the zero-thickness model of the wind tunnel at a corner-vane of the first corner (from Ansys Fluent).

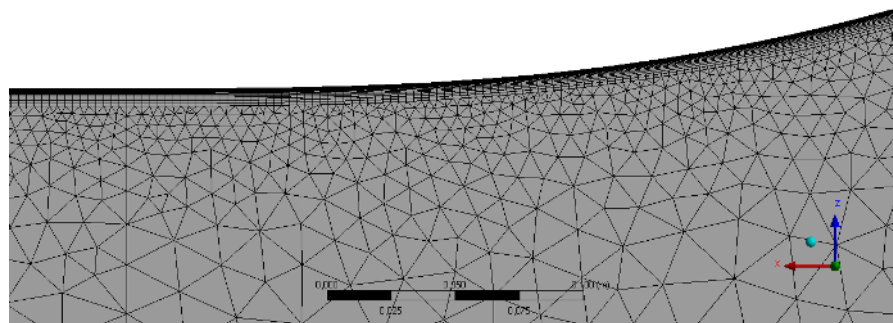


Figure 16: Mesh of the zero-thickness model of the wind tunnel at the outlet of the contraction (from Ansys Fluent).

The application had its default settings set to CFD with a solver preference completely set for Fluent. The mid-side element nodes were set to dropped. The size function was set to proximity and curvature with a fine relevance center. The initial size seed was on the active assembly and the smoothing of the mesh was selected to be high. The span angle center was fine and the number of cells across the gap was set to 10. Both the faces and edges were selected as the sources of the proximity size function. The growth-rate was 1.2 and the other settings remained untouched and were left to their default values. This resulted in a mesh with 89159 cells. The maximum skewness was 0.9993 with an average of 0.09826. The cells with this maximum skewness were only a very few present on the trailing-edges of the corner-vanes and are not expected to effect the solution in any way.

5.2.5 Mesh for Case without Wall Treatment

This mesh was made in order to let the solver integrate through the viscous sublayer and resolve the complete boundary layer. The y^+ value of the cells adjacent to the wall should therefore be less than 1. Unlike the previous case, this y^+ criterium should be met for the complete velocity-range. The walls were divided up in parts of 0.002 meter in order to hold an adequate transition between the inflation-layer and the unstructured mesh without requiring a high growth-factors between the inflations. The inflation-layers were set up in similar fashion to the previous mesh, where the first-layer heights where $4 \cdot 10^{-6}$ meter from inlet until the end of the test section, $5 \cdot 10^{-6}$ meter from the first diffuser until the first corner and $7 \cdot 10^{-6}$ meter from the second diffuser until the outlet. The growth-rate of both the inflation-layer and the rest of the mesh was set to 1.2 and a number 32 layers was chosen. This inflation-layer would cover the boundary layer for the given velocity-range with more than ten cells as well. The relevance center for this mesh was set to *coarse* and the number of cells across a gap was 9. This resulted in a mesh with 628829 cells. The maximum skewness was 0.9999 with an average of 0.06124. The cells with this maximum skewness were only a very few present on the trailing-edges of the corner-vanes and are not expected to effect the solution in any way. Figures 17, 18, 19 and 20, show screen captures of the mesh of the complete wind tunnel, first corner, a corner-vane in the first corner and of the wall at outlet of the contraction, respectively. The refined inflation-layer for resolving the complete boundary layer can be observed very well in these figures.

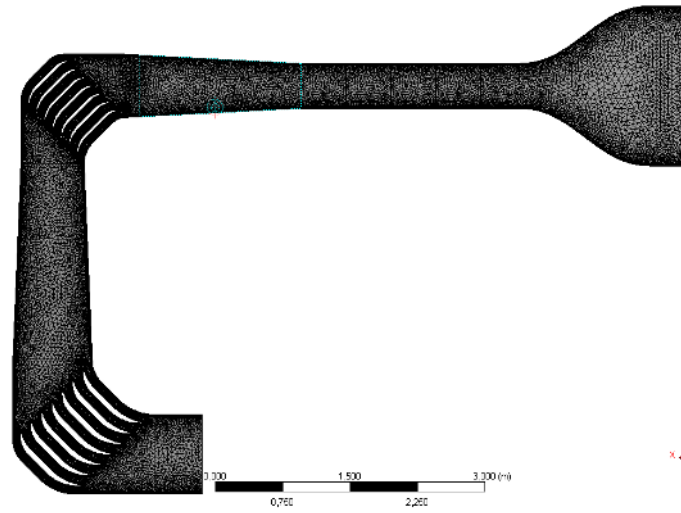


Figure 17: Mesh of the zero-thickness model of the wind tunnel (from Ansys Fluent).

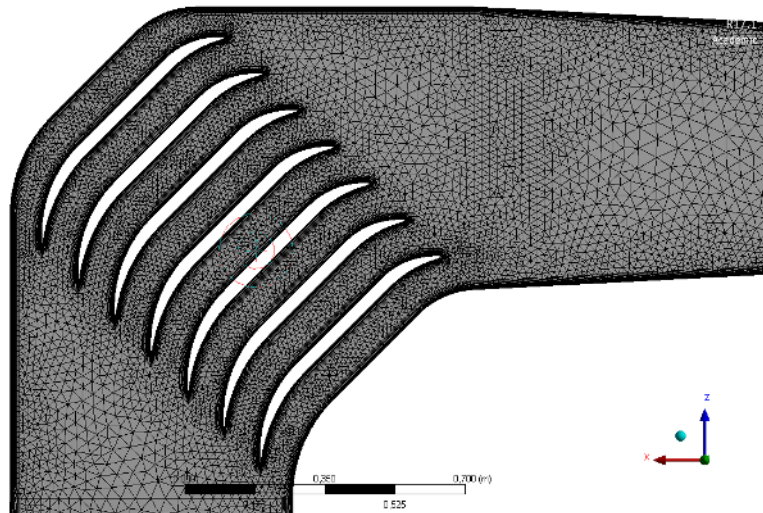


Figure 18: Mesh of the zero-thickness model of the wind tunnel at the first corner (from Ansys Fluent).

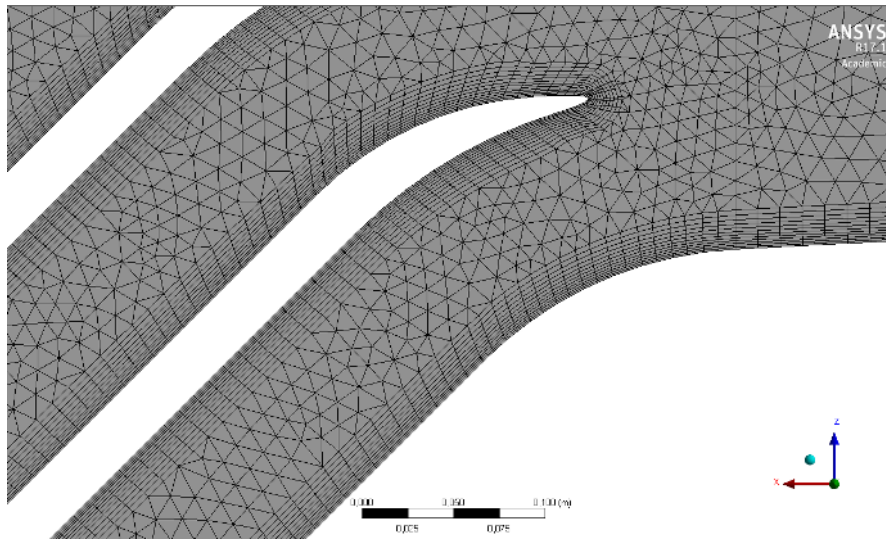


Figure 19: Mesh of the zero-thickness model of the wind tunnel at a corner-vane of the first corner (from Ansys Fluent).

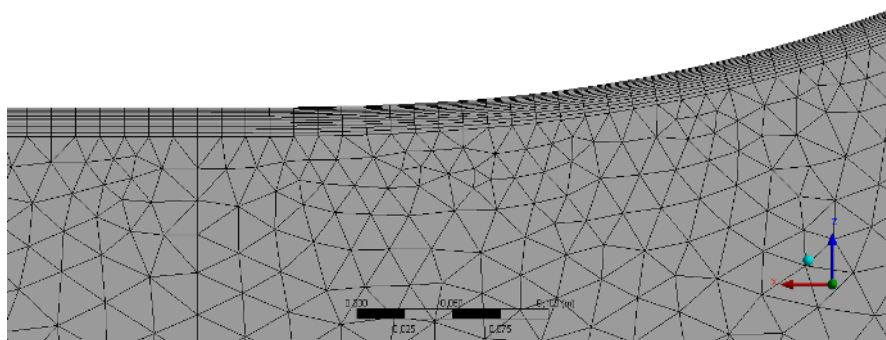


Figure 20: Mesh of the zero-thickness model of the wind tunnel at the outlet of the contraction (from Ansys Fluent).

5.2.6 Meshes for Convergence Study

For the cases with wall treatment, the first layer-heights were left alone. The edge-sizing at the walls was lowered 0.0075 meter, the number of cells across the gap was increased to 15 and the growth-rate of the cells was lowered, again, to 1.1. This resulted in a mesh with 138500 cells. The maximum skewness was 0.99943 with an average of 0.08124. The cells with this maximum skewness were only a very few present on the trailing-edges of the corner-vanes and are not expected to effect the solution in any way.

The edge-sizing along the walls was decreased to 0.0015 meter for the cases without wall treatment. The number of cells across gaps was 15 and the relevance center *medium*. The growth-rate of the cells in the mesh was lowered to 1.1. This resulted in a mesh of 940159 cells with a maximum skewness of 1. The cells with this maximum skewness were only a very few present on the trailing-edges of the corner-vanes and are not expected to effect the solution in any way.

5.3 Fluent

As mentioned in the previous SST $k - \omega$ model was chosen to do the CFD evaluations. The SST $k - \omega$ model is two-equation eddy-viscosity model that solves the turbulent kinetic energy k and the specific rate of dissipation of kinetic energy ω . Eddy-viscosity models also use the eddy-viscosity μ_t in order to calculate the Reynolds stresses. Fluent implements this model as formulated by (Menter 1994). The curvature correction and production-limiter that Fluent offers for the SST $k - \omega$ model were also selected.

The driving force will be pressure difference between the in- and outlet. The turbulence-intensity was set to the default value of 5%. The hydraulic diameters of the in- and outlet correspond with the duct-height that is normal to the flow direction. For the in- and outlet, this would be 1.78 and 0.8862 meter, respectively. The gauge pressure at the inlet of the wind tunnel was kept at 0 Pascal, whilst the gauge pressure at the outlet would be set and -25 Pascal and would subsequently be decreased with increments of 25 Pascal until a flow velocity of 50 meters per second would be reached inside the test section of the wind tunnel. This was later on found to be at -725 Pascal.

For the simulations, the SIMPLE algorithm was used - A semi-implicit method that solves the momentum equation implicitly and the velocity equation explicitly. For the spatial discretization, the default settings of Fluent were used. The under-relaxation factors were set to the default values as well, except for the pressure, which was set to 0.2. The under-relaxation factor for pressure was lowered for the sake of stability. Convergence would be met if all the residuals would fall below $1e-5$ and the flow velocity inside the test section was monitored

at the same time. Before running the simulations, a standard initialization was used.

5.4 Results

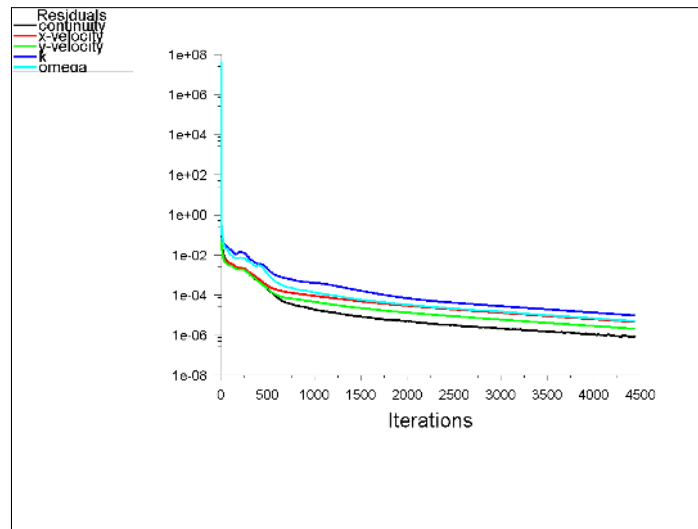


Figure 21: The convergence history of residuals for the simulation with standard grid and wall treatment at pressure difference of 25 Pa (from Ansys Fluent).

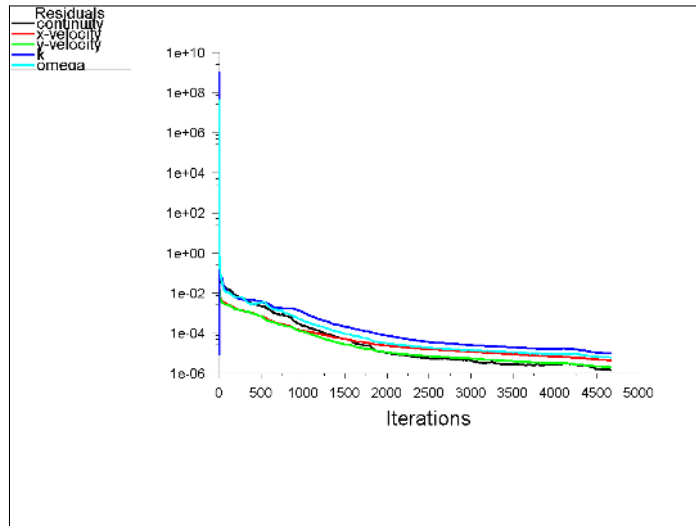


Figure 22: The convergence history of scaled residuals for the simulation with standard grid and wall treatment at pressure difference of 725 Pa (from Ansys Fluent).

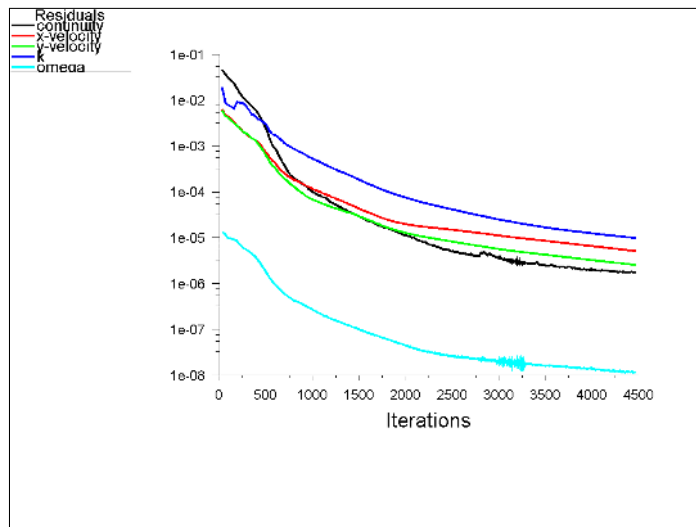


Figure 23: The convergence history of scaled residuals for the simulation with standard grid and no wall treatment at pressure difference of 25 Pa (from Ansys Fluent).

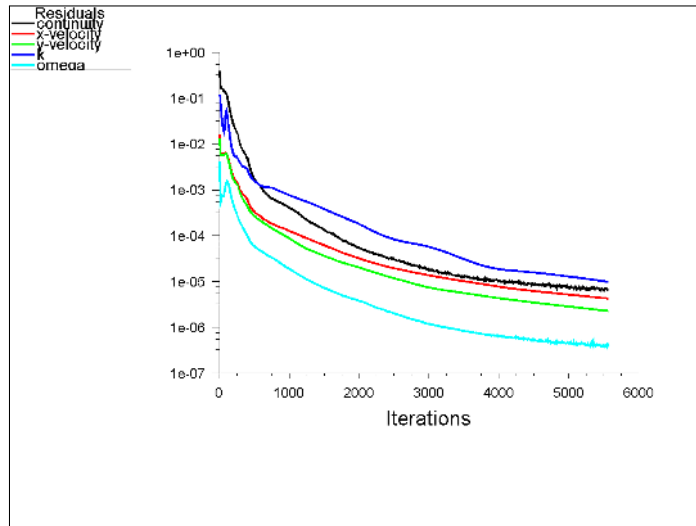


Figure 24: The convergence history of scaled residuals for the simulation with standard grid and no wall treatment at pressure difference of 725 Pa (from Ansys Fluent).

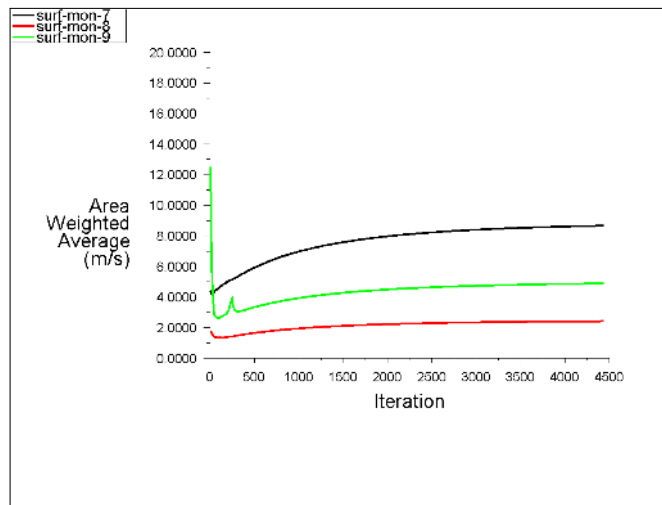


Figure 25: The convergence history of velocity at inlet, outlet and inside the test section for simulation with standard grid and wall treatment at pressure difference of 25 Pa (from Ansys Fluent).

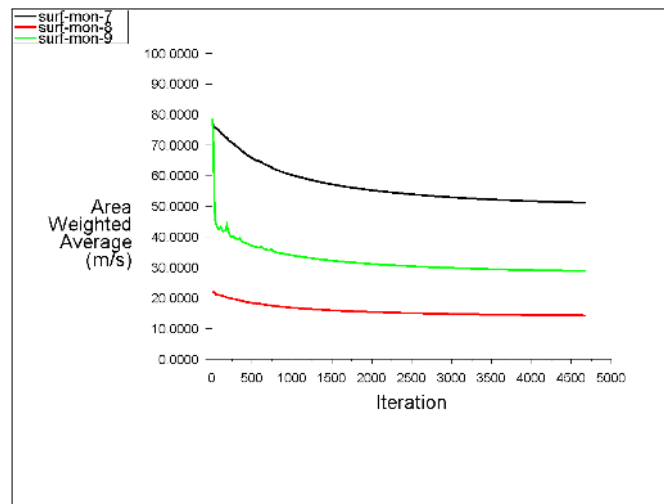


Figure 26: The convergence history of velocity at inlet, outlet and inside test section for simulation with standard grid and wall treatment at pressure difference of 725 Pa (from Ansys Fluent).

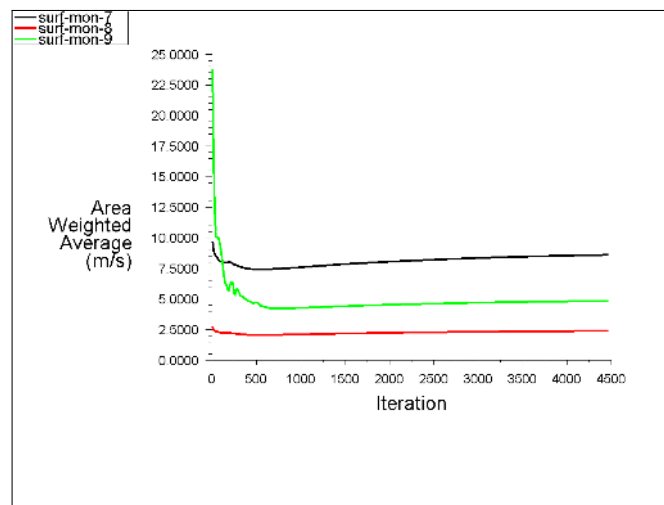


Figure 27: The convergence history of velocity at inlet, outlet and inside test section for simulation with standard grid and no wall treatment at pressure difference of 25 Pa (from Ansys Fluent).

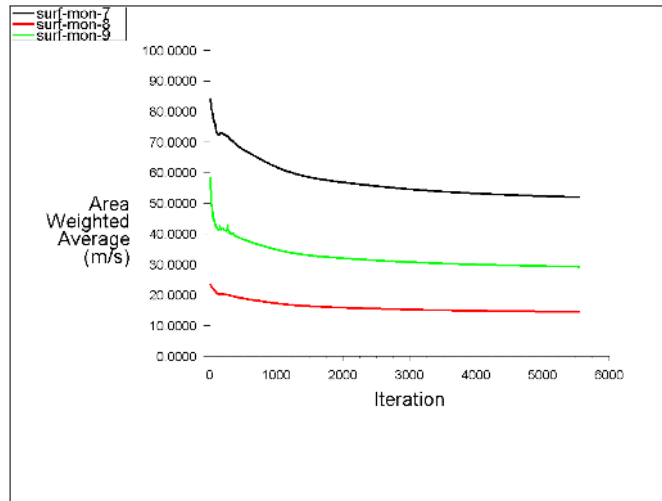


Figure 28: The convergence history of velocity at inlet, outlet and inside test section for simulation with standard grid and no wall treatment at pressure difference of 725 Pa (from Ansys Fluent).

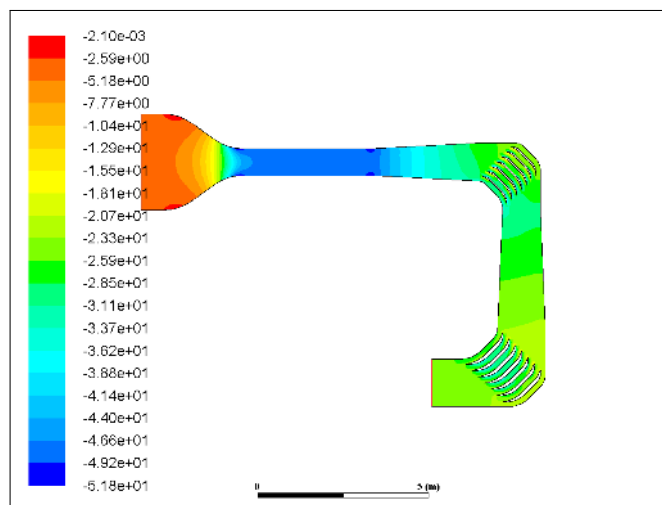


Figure 29: Contour plot of static pressure inside the duct for simulation with standard grid and no wall treatment at pressure difference of 25 Pa (from Ansys Fluent).

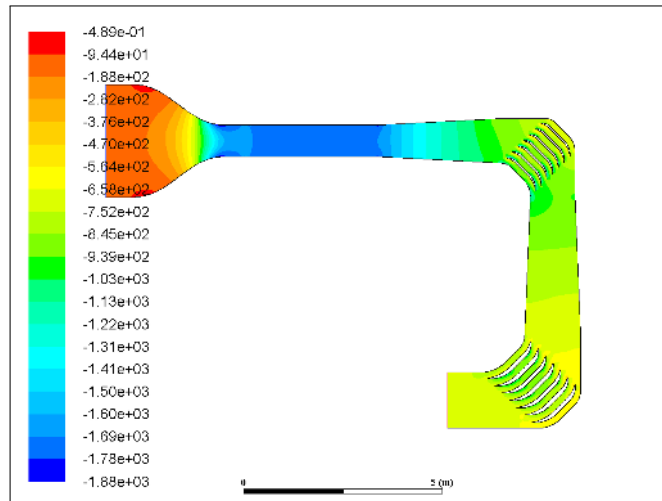


Figure 30: Contour plot of static pressure inside the duct for simulation with standard grid and no wall treatment at pressure difference of 725 Pa (from Ansys Fluent).

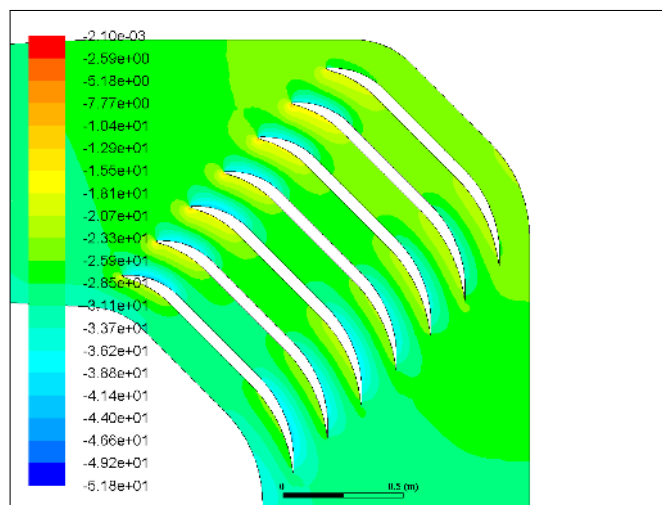


Figure 31: Contour plot of static pressure in the first corner for simulation with standard grid and no wall treatment at pressure difference of 25 Pa (from Ansys Fluent).

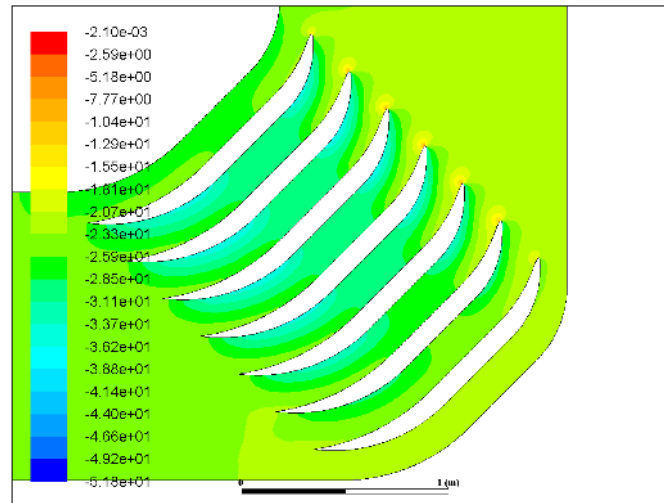


Figure 32: Contour plot of static pressure in the first corner for simulation with standard grid and no wall treatment at pressure difference of 725 Pa (from Ansys Fluent).

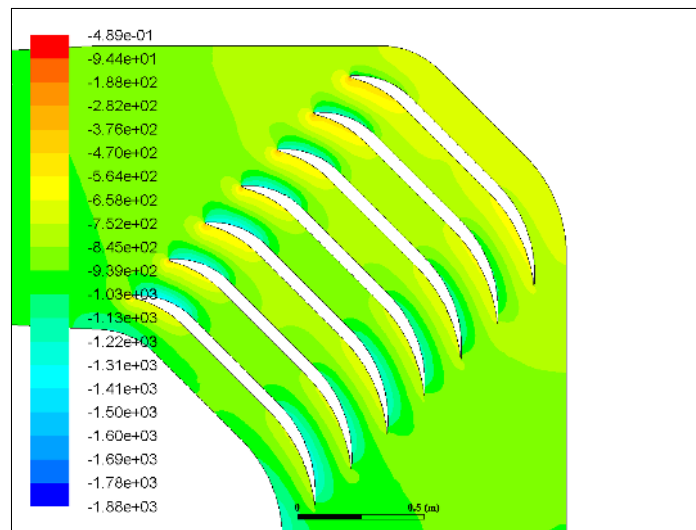


Figure 33: The contour plot of the static pressure in the second corner for the simulation with the standard grid and no wall treatment at a pressure difference of 25 Pa (from Ansys Fluent).

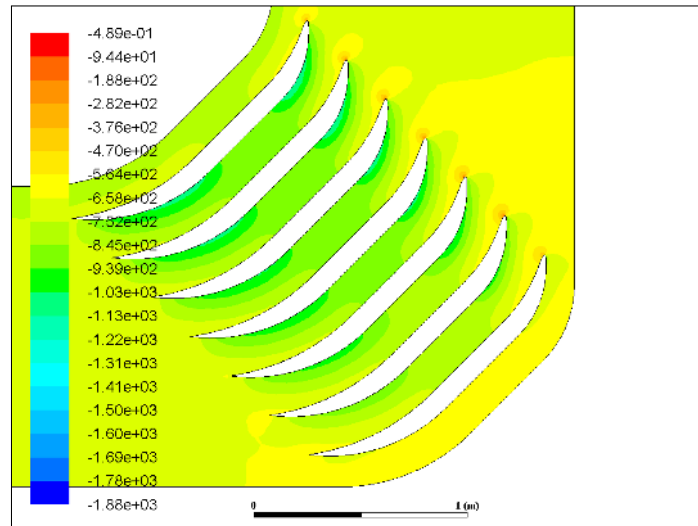


Figure 34: The contour plot of the static pressure in the second corner for the simulation with the standard grid and no wall treatment at a pressure difference of 725 Pa (from Ansys Fluent).

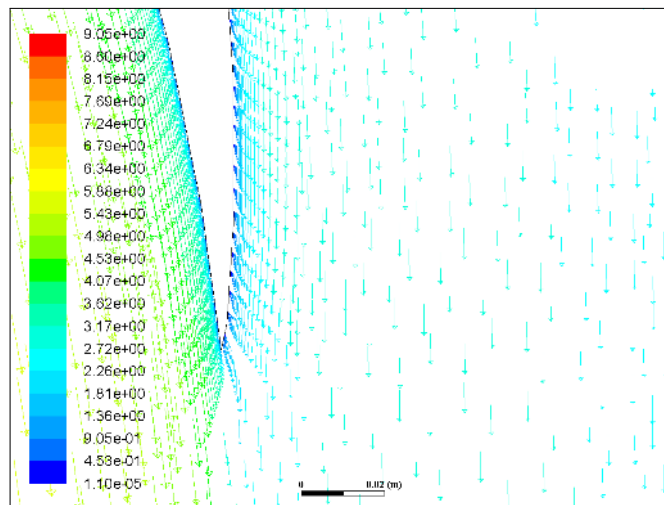


Figure 35: The velocity vectors in the first corner for the simulation with the standard grid and no wall treatment at a pressure difference of 25 Pa (from Ansys Fluent).

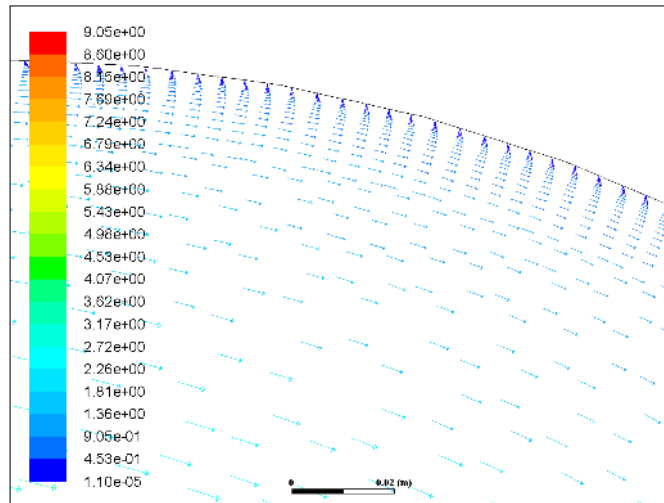


Figure 36: The velocity vectors in the first corner for the simulation with the standard grid and no wall treatment at a pressure difference of 725 Pa (from Ansys Fluent).

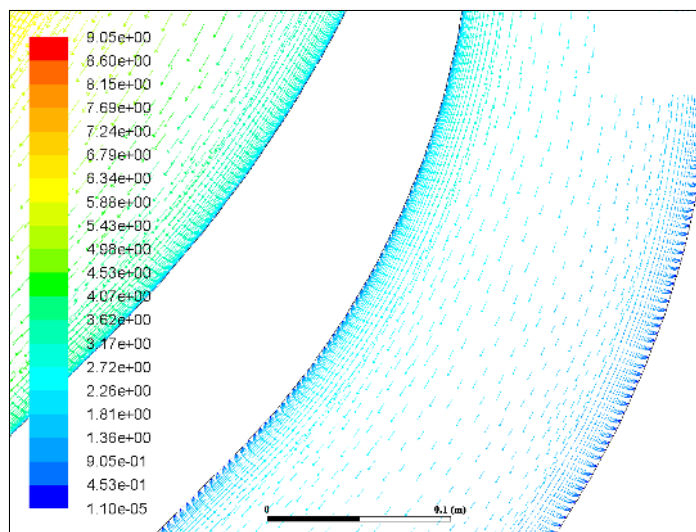


Figure 37: The velocity vectors in the second corner for the simulation with the standard grid and no wall treatment at a pressure difference of 25 Pa (from Ansys Fluent).

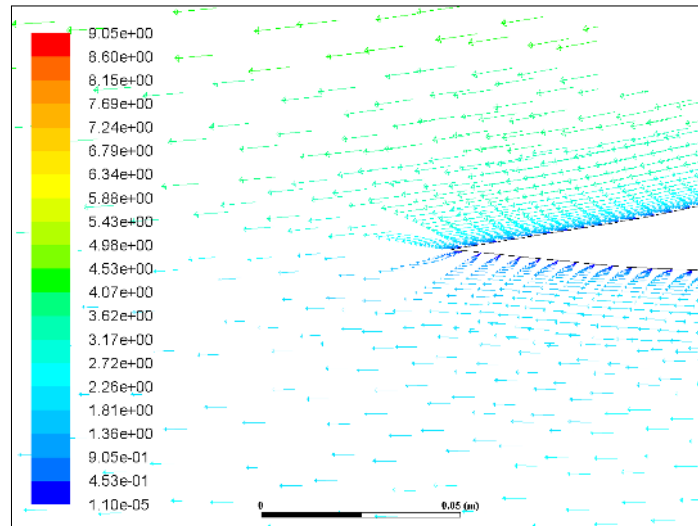


Figure 38: The velocity vectors in the second corner for the simulation with the standard grid and no wall treatment at a pressure difference of 725 Pa (from Ansys Fluent).

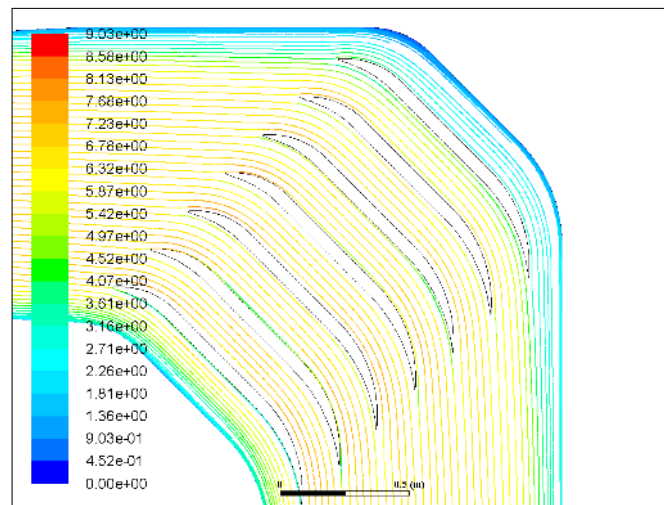


Figure 39: The streamlines in the first corner for the simulation with the standard grid and no wall treatment at a pressure difference of 25 Pa (from Ansys Fluent).

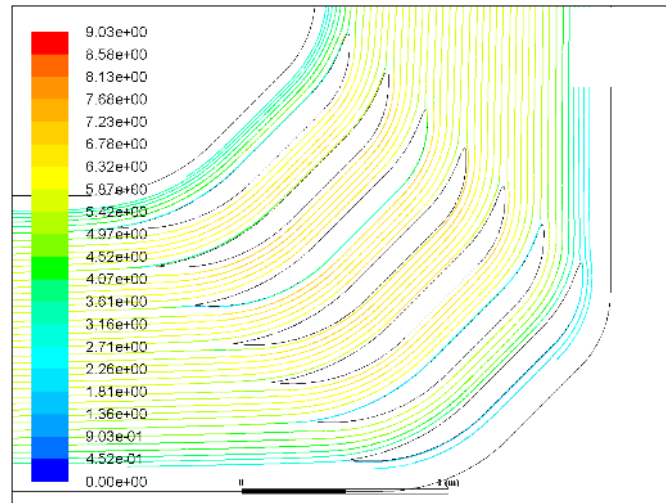


Figure 40: The streamlines in the first corner for the simulation with the standard grid and no wall treatment at a pressure difference of 725 Pa (from Ansys Fluent).

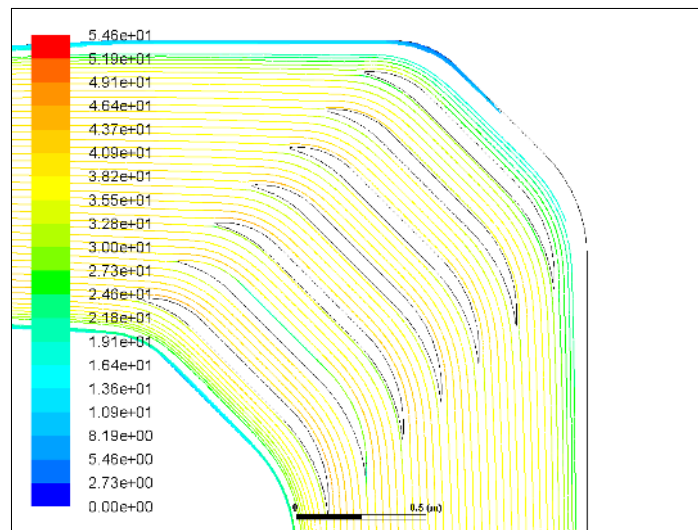


Figure 41: The streamlines in the second corner for the simulation with the standard grid and no wall treatment at a pressure difference of 25 Pa (from Ansys Fluent).

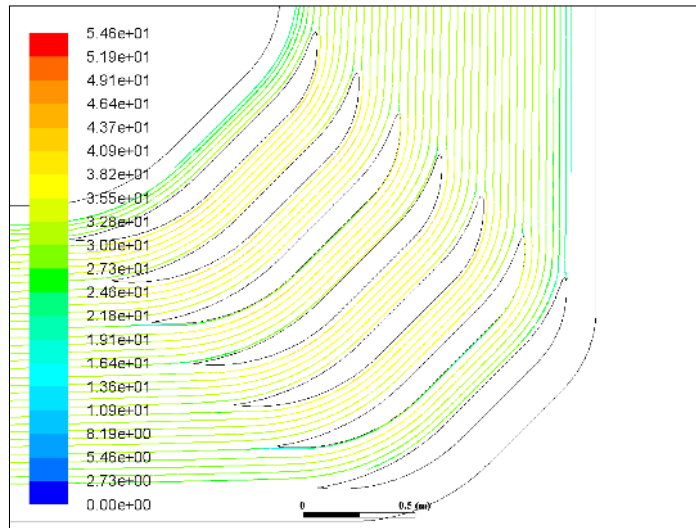


Figure 42: The streamlines in the second corner for the simulation with the standard grid and no wall treatment at a pressure difference of 725 Pa (from Ansys Fluent).

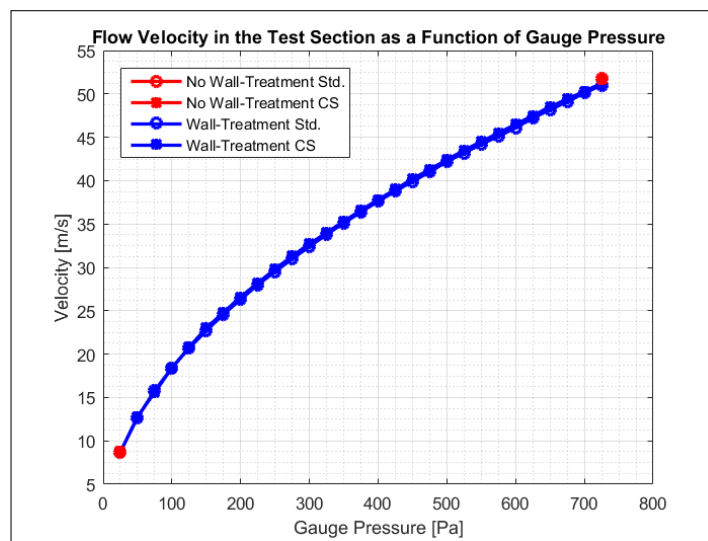


Figure 43: Velocity plotted against the gauge pressure at outlet for the two meshes where wall treatment was used (from MatLab).

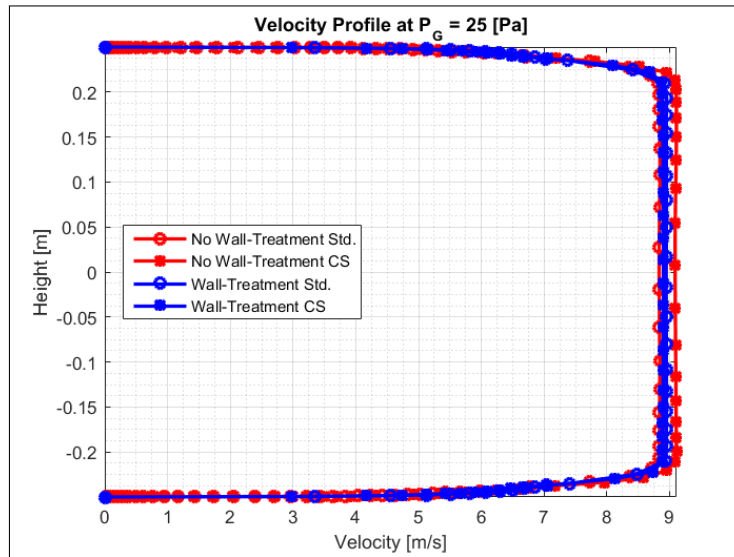


Figure 44: The velocity profile over the duct-height in the middle of the test section for all of the four meshes at a pressure difference of 25 Pa (from MatLab).

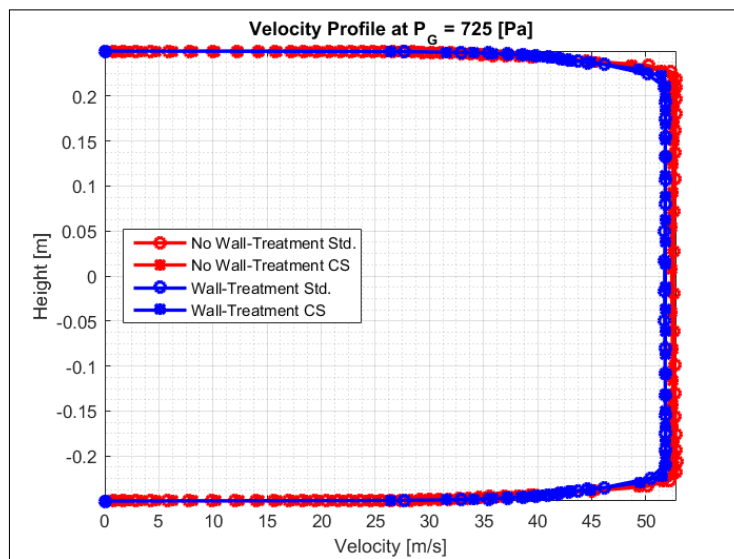


Figure 45: The velocity profile over the duct-height in the middle of the test section for all of the four meshes at a pressure difference of 725 Pa (from MatLab).

5.5 Discussion of 2D CFD Results

Figure 21 and 22 show the residuals for the simulations with the standard grid and the use of the wall treatment for pressure differences at 25 and 725 Pa, respectively, at which the upper and lower limits of the earlier specified velocity-range would be reached. Figure 23 and 24 show the same plots for the standard grid where no wall treatment was used for pressure differences at 25 and 725 Pa, respectively. The wavy trend of the solutions for the first couple of iterations can be a results of sensitivity of the SST $k - \omega$ model to the initial conditions. The fact that the oscillating behaviour does not continue until convergence, indicates that a steady RANS model can be used adequately for these cases.

Figure 25 and 26 show the convergence of the average velocity found at the inlet, outlet and inside the test section for the simulations with the standard grid and the use of the wall treatment for pressure differences at 25 and 725 Pa, respectively. Whereas Figure 27 and 28 show the same plots for the standard grid with no wall treatment for pressure differences at 25 and 725 Pa, respectively. The plots show that the velocity hardly changes when convergence is reached and are, therefore, a good indication that the solution is acceptable.

Figure 43 shows the average velocity inside the test section plotted against the gauge pressure from 25 until 725 Pa for the standard mesh and refined mesh where wall treatment was used. It can be seen that the velocities range from approximately 10 to 50 m/s . In the same Figure, the velocities that were found at 25 and 725 Pa can be observed for the standard and refined mesh without wall treatment. The results from the cases with the refined grids are overlapping with those from the standard grids.

Figures 44 and 45 show the velocity profiles seen in the duct at pressure differences of 25 and 725 Pa, respectively. It can be seen that the flow is uniform for a large part of the cross-section and the velocity profiles do not show any strange behaviour. Table 1 shows the flow uniformity for the four different meshes at a pressure difference at 25 and 725 Pa. It can be seen that sufficient levels of uniformity are reached.

Table 1: Flow uniformity within the test section

Gauge Pressure at Outlet	No Wall-Treatment Std.	No Wall-Treatment CS	Wall-Treatment Std.	Wall-Treatment CS
25	0.9912	0.9918	0.9884	0.9900
725	0.9912	0.9918	0.9882	0.9899

Figures 29 to 34 show the static pressure in the complete tunnel and the corners for a solution where no wall treatment was used for pressure differences

of 25 and 725 Pa. From these Figures, it can be seen that the flow that has gone through the contraction requires some distance for the pressure to settle and remain largely unchanged throughout the test section. This was, as mentioned in the previous, already taken into account during the sizing of the new wind tunnel duct. Pressure recovery can be seen inside the diffusers and corners as soon as the flow has left the test section. The recovery is gradual and there seems not to be any strange behaviour throughout the duct. The rapid change of static pressure inside the contraction is because of the flow acceleration and the two small low pressure regions at the end of the test section in Figure 29 are a consequence of the angle that the first diffuser makes with the test section. A closer look at the corners, shows, as expected, low pressure regions over the outside of the corner-vane and high pressure regions at the leading edge (stagnation) and along the inside of the corner-vane. The absence of severe changes in variations of static pressure may already hint that there will not be any flow separation present.

Figures 39 to 42 show the streamlines in the corners. Figures 39 and 40 show the streamlines at a pressure difference of 25 Pa in the first and second corner, respectively. Figures 41 and 42 show the streamlines at a pressure difference of 725 Pa in the first and second corner, respectively. If separation would occur, the corners would be the most likely areas for where it would take place. From inspecting Figures 39 to 42, it can be concluded that separation cannot be found in the corners. The streamlines that are discontinued in the corners, indicate low velocities and at these locations separation or flow reversal may occur after all. It is therefore important to inspect the vector plots at these locations as well.

Figures 35 to 38 show vector plots of critical locations inside the wind tunnel, where separation or flow reversal may occur. These locations were considered critical after inspection of the streamline plots. Figures 35 and 37 show the outer part of first bend of the first and second corner, respectively. Figures 36 and 38 show the same, except that the second bend is shown for the first and second corner, respectively. None of the above mentioned phenomena occur at any of the four locations, even though flow velocity becomes rather low.

The results of the 2D CFD evaluations show that the wind tunnel has acceptable characteristics. From Figures 43, 44 and 45 it can already be seen that the results vary very little with a refined grid. Even though the number of cells was only increased once by a factor of approximately 1.5 and the refining of the inflation-layer may not have been the right way to go in a convergence-study, it is not expected that outcomes would drastically change when an additional converged grid was used. In Table 2 an overview of the area-averaged flow velocities inside the test section and total pressure losses of the simulations can be seen. it can be seen that the numbers are consistent with continuity and Bernoulli's principle at the outlet. Even though the set-up of the simulations were not ideal

and did not always follow the Fluent User's Guide recommendations, the results are considered good enough. The next step is to evaluate the 3D geometry of the wind tunnel.

Table 2: Overview of the area-averaged flow velocities found in the test section and total pressure losses for different simulation cases.

	Gauge Pressure [Pa]	Flow Velocity [m/s]	Pressure Loss [Pa]
No WT Std.	25	8.63	9.80
	725	51.8	189
No WT Rfd.	25	8.85	9.25
	725	51.7	192
WT Std.	25	8.73	9.49
	725	51.0	204
WT Rfd.	25	8.68	9.67
	725	51.2	199

6 3D CFD Simulations

The 3D CFD simulations in Ansys were setup in a similar fashion as the 2D simulations. In total, 20 initial simulations were done. The first 2 simulations were to resolve the complete boundary layer at the aforementioned lower and upper velocity boundaries of approximately 10 and 50 meters per second, respectively, inside the test section of the wind tunnel. These simulations were to give a clear insight in the flow quality of the wind tunnel and were used to find the most prominent broadband noise sources. The following 8 simulations used wall treatment. These simulations were used to make velocity and pressure loss distributions of the wind tunnel. These distributions could later be used to evaluate whether the current power source and fan are sufficient for the new design. The last 10 simulations were the same as the aforementioned cases, but with a refined grid for a small convergence study.

In this section, the geometry will be evaluated and treated first, then the meshes for the 3D cases are created, where after the solver settings are discussed. Then the aerodynamic results are presented and the foremost flow-induced noise sources are shown. This section will be concluded with a discussion about the results.

6.1 Geometry

The 3D model was first given 30 millimeter chamfers that made a 45 degree angle with the wall on the corners of the cross-section. Then, before exporting the geometry, the angles the diffusers make with the other parts at the inlet, were rounded off with an arch with a radius of 200 millimeter. After exporting the model from Catia V5 and importing the 3D model into the Ansys Design Modeler, the adjacent faces of all parts of the wind tunnel were given named selections for the sake of post-processing the results of the CFD evaluations at a later stage. The next step was creating a symmetry-plane along the flow direction of the wind tunnel in order to reduce cell-count after meshing and minimizing computational effort during the evaluations as only half of the geometry was required to be meshed. This symmetry-plane would not affect the solutions as the 3D effects were not expected to be asymmetrical in a symmetrical duct. If rotation were to occur around the axis of the flow-direction however, this may be more difficult to identify because of the asymmetrical motion and the nature of the set-up with the symmetry plane. In Figure 46 the geometry is as it will be seen by the mesher and the solver in the subsequent steps of finding a 3D CFD solution.

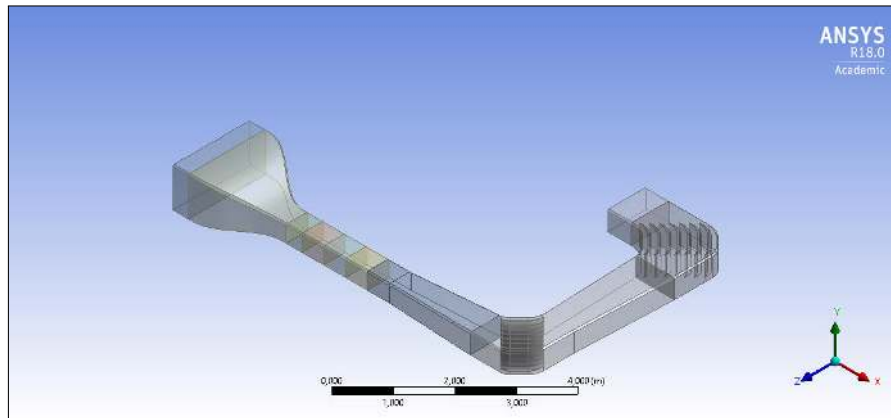


Figure 46: Symmetry model of the wind tunnel geometry (from Ansys).

6.2 Meshing

For the 20 different cases, or simulations, 6 meshes were required, of which 4 were needed for the cases where the boundary layer was resolved completely and 2 were needed for the cases with wall treatment. Again, the Ansys Mesher was used.

6.2.1 Mesh for the Lower Velocity Limit

For this mesh, with the assumption of a flow velocity of approximately 10 meters per second inside the test section, a first layer height of $2e-5$ m for the inflation-layer between the inlet and the end of the first diffuser was chosen. For the first corner and the second diffuser, this first layer height was increased to $3.3e-5$ m because of the increased cross-section. From the start of the second corner until the outlet, the first layer height was set to $4.2e-5$. All the inflation-layers had 28 layers and a growth factor of 1.2. Whilst fewer layers would suffice to reach a y^+ value of 300, which Fluent considers as the point where the free-stream region begins, layers were added to secure a better volume-wise transition to the tetrahedron mesh. A later check in Fluent, after reaching a converged solution, it was found that the y^+ value would not exceed 0.822, which is well under the recommended value of 1 for resolving the complete boundary layer.

Further settings for the mesh were a proximity and curvature size function, of which the proximity size function had the faces and edges as its source, with a coarse relevance center. The transition was set to be fast and a fine span angle was selected. The number of cells across a gap was set to 4. The initial size seed was selected to be on the active assembly, the growth rate was 1.2 and the automatic mesh based defeaturing was turned on. All the other options had its default values. A face sizing of 0.02 m was given to the outer walls of the wind

tunnel. The faces of the trailing edges of the corner vanes were given a face sizing of 0.01 m. Both sizings were done with the soft sizing option.

These settings resulted in a mesh with 10799471 cells with a maximum and average skewness of 0.96132 and 0.31015, respectively.

6.2.2 Mesh for the Lower Velocity Limit with Refined Grid

For the refined grid, with respect to the standard grid, the following changes were made: the relevance center was set to medium, the number of cells across a gap was 5 and the growth rate was lowered to 1.15. The face sizing of the outer walls and trailing-edges of the corner vanes were lowered to 0.015 m and 0.0075 m, respectively. This resulted in a mesh of 21057436 cells with a maximum and average skewness of 0.96104 and 0.28549, respectively. Even though the inflation layer did not change, the maximum y^+ value found in this grid was 0.971.

6.2.3 Mesh for the Upper Velocity Limit

The first layer height of the inflation layer from the inlet until the end of the first diffuser was $6e - 6$ m, from the start of the first corner until the end of the second diffuser this height was increased to $1e - 5$ m and from the start of the second corner until the outlet to $1.25e - 5$ m. The amount of inflation layers was 35 with a growth rate of 1.2. During post-processing, the maximum y^+ value found was 0.969.

The general mesh settings, together with the face sizings, were identical to the case with the standard grid of the lower velocity limit. An edge sizing option was added for the trailing edges of all the corner vanes. The hard sizing option was selected with an element size of 0.0025 m. In order to avoid stair-step meshing, the gap factor of the inflation layer was decreased to 0.2 and the maximum angle was increased to 180° . With these option, a mesh with 14855129 cells was generated and had a maximum and average skewness of 0.96195 and 0.20355, respectively.

6.2.4 Mesh for the Upper Velocity Limit with Refined Grid

For this refined grid, the exact same changes were made as done for the refined grid of the mesh for the lower velocity limit. The edge sizing on the trailing-edge was lowered to $2e-3$ m with a growth-rate of 1.15. This resulted in a mesh of 28094966 cells with a maximum and average skewness of 0.96341 and 0.29959, respectively. The maximum y^+ value found for this grid was 0.981.

6.2.5 Mesh for the Cases with Wall Treatment

As mentioned in the previous, Fluent provides a wall treatment to solve the boundary layer independent of the non-dimensional wall distance. It is recom-

mended however to keep cover the boundary layer with at least 10 cells in order produce accurate results. Since this mesh will be used for different flow velocities ranging from the lower until the upper limit, it has to fulfill the 10 layer criterium in each case. With first layer heights of 4e-5 m, 7e-5 m and 8e-5 m for the aforementioned regions of the wind tunnel, 24 inflation layers and a growth rate of 1.2, the 10 layer criterium would be fulfilled for flow velocities lying approximately between 10 and 50 meters per second inside the test section.

The general meshing settings were identical to those of the mesh for the lower velocity limit – the first presented meshing case, with the face sizing options included. Along with the inflation layer, this resulted in a mesh with 9367840 cells and a maximum and average skewness of 0.95857 and 0.31321, respectively.

6.2.6 Mesh for the Cases with Wall Treatment and Refined Grid

For this mesh, the settings of the standard mesh for the cases with wall treatment have undergone the same changes as done for the refined grid of the first presented case in this subsection. This resulted in a mesh of 1833485 cells and a maximum and average skewness of 0.957 and 0.287, respectively

6.3 Solver Settings

It was desired that a solution as found for a 3D model with double precision. From the relatively large face sizing compared to the low first layer heights of the inflation layer, it can be assumed that the aspect-ratio of the cells are high and the double precision, at the costs of extra memory, would be helpful. The SST $k - \omega$ model was preferred for its favorable characteristics close and away from the wall. For all the simulations, besides the default settings, the regular production limiter and curvature correction were selected too.

In contrast to the 2D simulations, the pressure based coupled-solver was used instead of the SIMPLE algorithm that uses a pressure based segregated algorithm. The use of the SIMPLE algorithm resulted in a strong oscillation of the residuals and difficulties in converging in trial simulations. Especially when a more accurate solution was desired by using a second order upwind scheme for spatial discretization of the flow variables. The difficulty of reaching a converged solution is likely to be a consequence of the highly skewed cells found in the meshes and the number of them. The pressure-based coupled solver is considered more robust and superior to the SIMPLE solver by Ansys. The coupled solver is a full implicit coupling method that couples the pressure and momentum continuity equations and solves these simultaneously by introducing a time-step in the form of the Courant number. It was therefore believed that the coupled solver would give the desired performance. The Courant number will replace the under-relaxation factors for pressure and momentum and localize

the advancement of the solution with a localized time-step. This localized time-step is superior to one single time-step over the whole domain as a universal time-step may either be too low and result in slow convergence or too high and result in solution divergence. The full implicit coupled method is, of course, faster than the semi-implicit segregated method, but is at the cost of using approximately twice as much memory according to the Fluent User's Guide. Turbulence kinetic energy and specific dissipation rate are still segregated for this method.

Along with the coupled scheme, second order upwind spatial discretization was selected for pressure, momentum, turbulence kinetic energy and turbulence specific dissipation rate. The gradient had its least-squares cell based default option. A High order term relaxation for all the flow variables with a default value of 0.25 was used to improve the start-up of the simulation and prevent the convergence from stagnating. This form of relaxation should also minimize the need for modifications during the simulation, such as changing the courant number and/or the residuals. For the same reason choosing the double precision, the warped-face gradient correction was also used.

The flow courant number was lowered from the default 200 to 10 in order to guarantee stability and convergence at the cost of speed as a minimal interaction with the simulations was desired once the simulations were initiated. As the turbulence kinetic energy showed difficulties converging when the SIMPLE scheme was used, the under relaxation factors of pressure, momentum, density, turbulence kinetic energy and turbulence specific dissipation rate were lowered to 0.2, 0.2, 0.4, 0.35 and 0.35, respectively. Turbulence kinetic energy and turbulence specific dissipation rate are not coupled and still required the under relaxation factors to converge.

6.4 Solution Monitors

The static pressure, velocity and volume rate were monitored at the inlet, in the test section and at the outlet during the simulations in order to see whether the solution would converge. The convergence set to be reached when the continuity, momentum, turbulence kinetic energy and turbulence specific dissipation rate residuals were below $5e-5$. In comparison with the 2D simulations, the convergence criterium was lowered slightly. This was done first when the SIMPLE solver was still used in order to see whether the turbulence kinetic energy could converge before the continuity started to oscillate. It was not expected that the criterium of $5e-5$ would have any large effects and have a drastically changed outcome compared to when lower criteria were used instead. Moreover, there were insufficient resources available that would allow for lengthy simulations.

6.5 Boundary Conditions

The driving force through the wind tunnel was a pressure difference and made by selecting a pressure-inlet and pressure-outlet in Fluent. Whilst the gauge pressure at the inlet was kept zero, the gauge pressure at the pressure outlet was varied for the cases. For the cases without wall treatment, the gauge pressure was set at -25 Pa for the lower velocity limit and -725 Pa for the upper velocity limit, which would result in a flow velocity of approximately 10 and 50 m/s inside the test section, respectively. For the cases with wall treatment, the gauge pressure at the outlet was decreased from -25 Pa to -725 Pa with increments of 100 Pa. For the inlet as well as the outlet, the turbulence intensity was kept at its default value of 5 % whilst the hydraulic diameter was set to the respective hydraulic diameters of the duct found at the inlet and outlet.

6.6 Results

In Figure 47, the convergence of the velocity halfway through the test section can be seen for different simulation cases, where WT indicates the use of wall treatment. Figures 48a to 49b show the residuals of the simulations with the standard grids at 25 and 725 Pa. Figures 50a and 50b show contour plots of the velocity over the symmetry-plane. In this figure, regions of low velocity can be observed in the second diffuser. The $\overline{vv^{+2}}$ Reynolds stresses, determined by the Boussinesq approximation are plotted in Figures 51a and 51b. The low velocities found in Figures 50a and 50b and the regions with increased Reynolds stresses seen in Figures 51a and 51b may imply separation or other adverse flow effects in the diffusers. In Figures 52a and 52b, velocity vector plots of the cross-section can be seen at different locations in the first diffuser. Figures 53a and 53b are velocity vector plots over the cross-section at different locations in the second diffuser. Figures 54a to 55b and Figures 56a to 57b are identical to Figures 52a to 53b, but with the contours of the $\overline{vv^{+2}}$ Reynolds stresses and static pressure, respectively. Figures 58a and 58b are streamline plots through the wind tunnel.

The vector plots clearly show the presence of flow reversal or separation in the first and second diffuser. In the static pressure plots, a strong adverse pressure gradient developing from the corner of the first diffuser and present in the bottom of the second diffuser can be identified as the cause of the separation. In Figures 58a and 58b, some of the streamlines in the diffusers can be seen drifting. This also implies separation.

In Figures 59a and 59b velocity vector plots over cross-sections of the test section and the straight duct after the exit of the contraction. Figures 60a and 60b and Figures 61a and 61b are similar plots, but with the contours of the Reynolds stresses and static pressure, respectively, instead. A first glance at Figures 59a to 61b tells that the flow characteristics seem acceptable inside the test section.

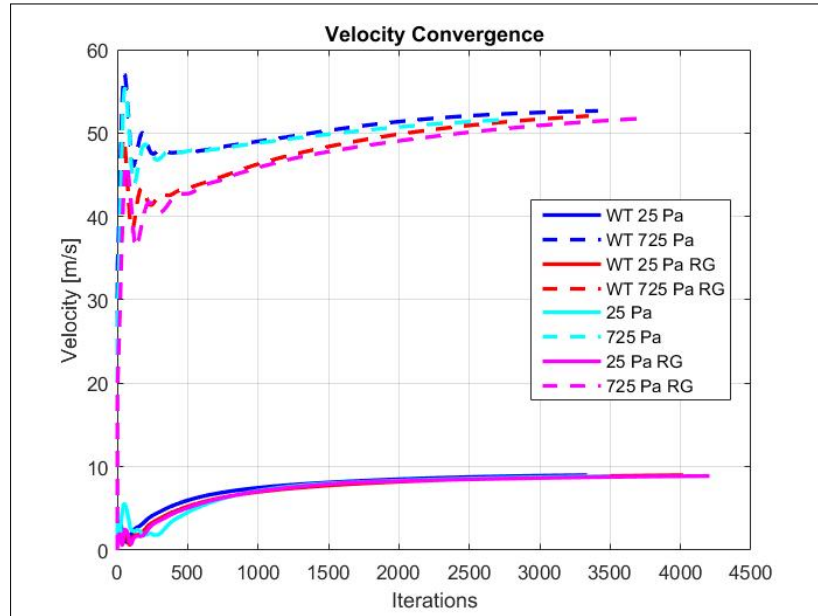
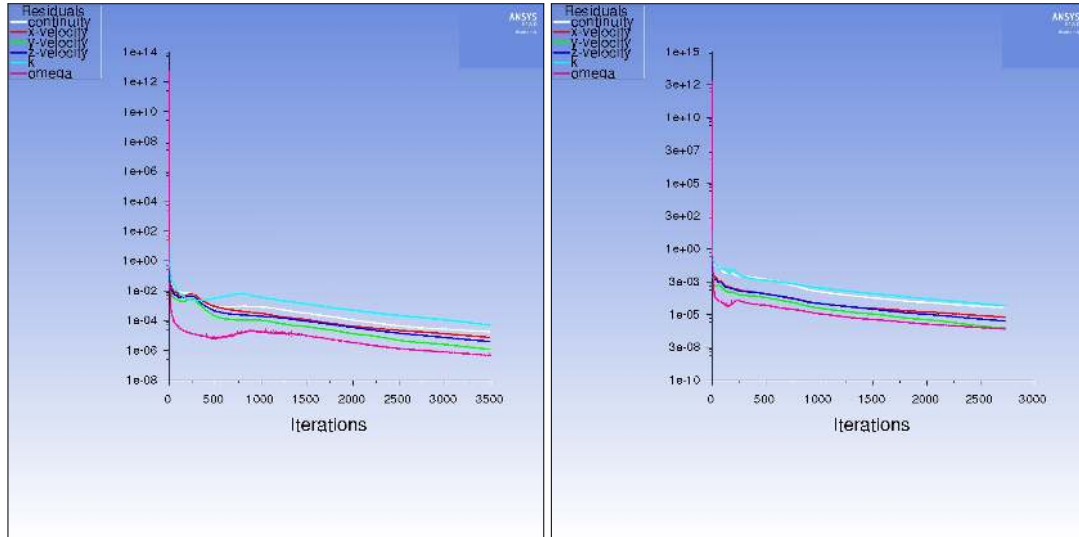


Figure 47: Convergence history of the velocity inside the test section. Wall treatment indicated by WT (from MatLab).

A further inspection of the flow inside the test section and the rest of the tunnel could be done by looking at the uniformity index of the velocity-profile and the turbulence intensity. Whilst the default definition of the area-weighted flow uniformity was good to go, the turbulence intensity had to be re-defined in Fluent as a user defined formula. From the Fluent Theory Guide, Equation 13 was taken

$$I \equiv \frac{\sqrt{\frac{2}{3}k}}{|U|} \quad (13)$$

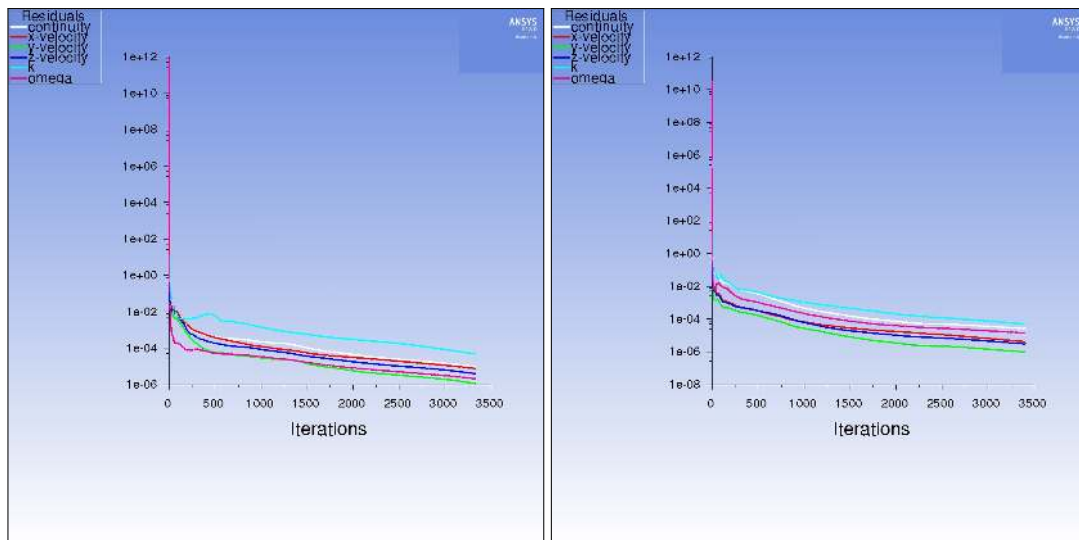
where I is the turbulence intensity, k is the turbulent kinetic energy and U is the velocity magnitude. In Table 3, the area-weighted average of the turbulence intensity and the area-weighted uniformity-index of the velocity and the area-weighted velocity at different locations inside the wind tunnel can be found. In Table 3 it can be seen that, the turbulence intensity at the inlet corresponds with the value given as the boundary condition and that the turbulence intensities found inside the test section generally stay low, the uniformity-indices of the velocity are high throughout the tunnel and that the velocity of the flow at the start of the first corner has reduced to 60% with respect to the test section as was desired during the design of the tunnel.



(a) Pressure difference of 25 Pa.

(b) Pressure difference of 725 Pa.

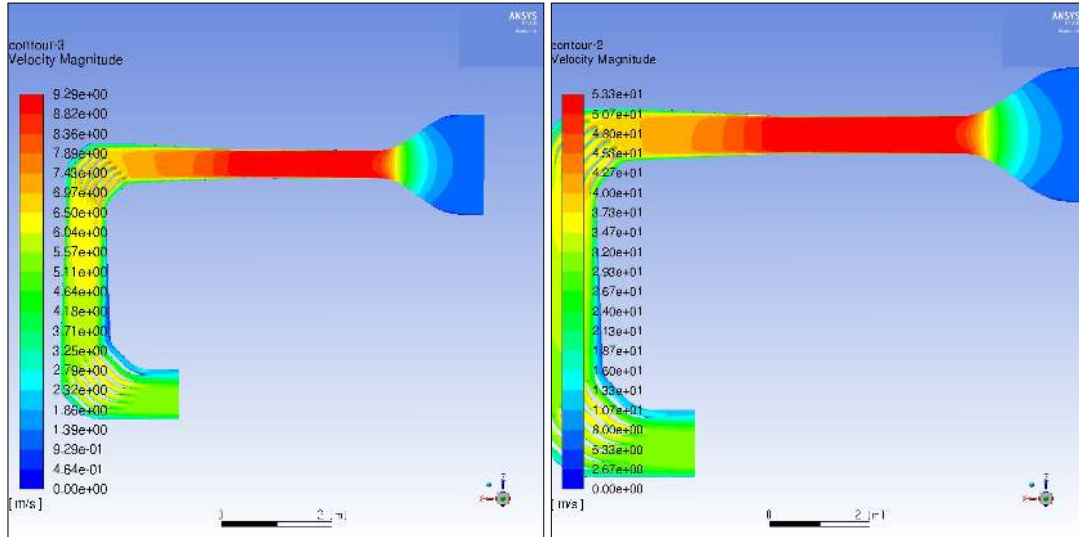
Figure 48: Residuals of the simulation with standard grid and no wall treatment (from Ansys Fluent).



(a) Pressure difference of 25 Pa.

(b) Pressure difference of 725 Pa.

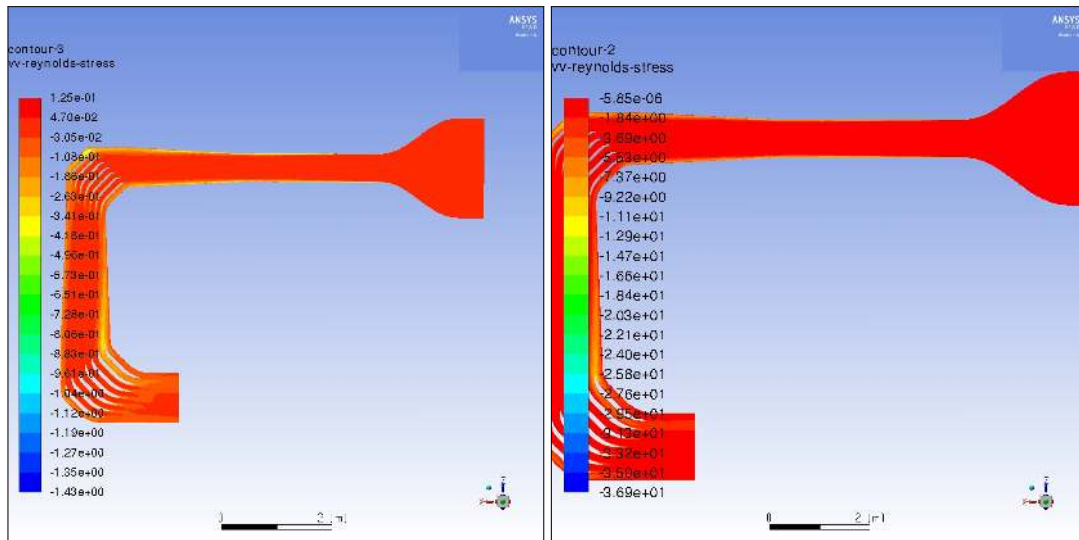
Figure 49: Residuals of the simulation with standard grid and wall treatment (from Ansys Fluent).



(a) Pressure difference of 25 Pa.

(b) Pressure difference of 725 Pa.

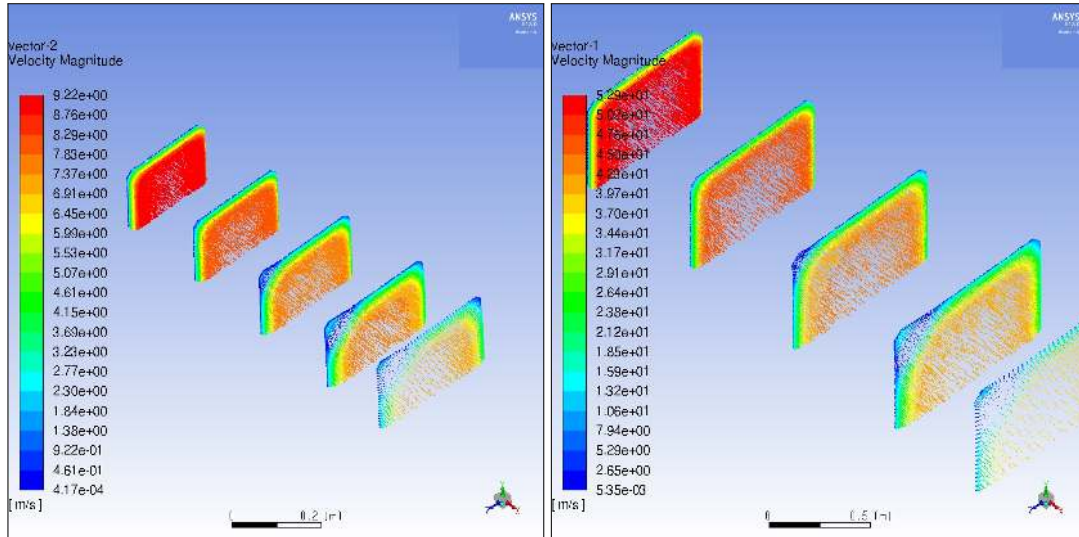
Figure 50: Contour plots of the velocity on the symmetry-plane (from Ansys Fluent).



(a) Pressure difference of 25 Pa.

(b) Pressure difference of 725 Pa.

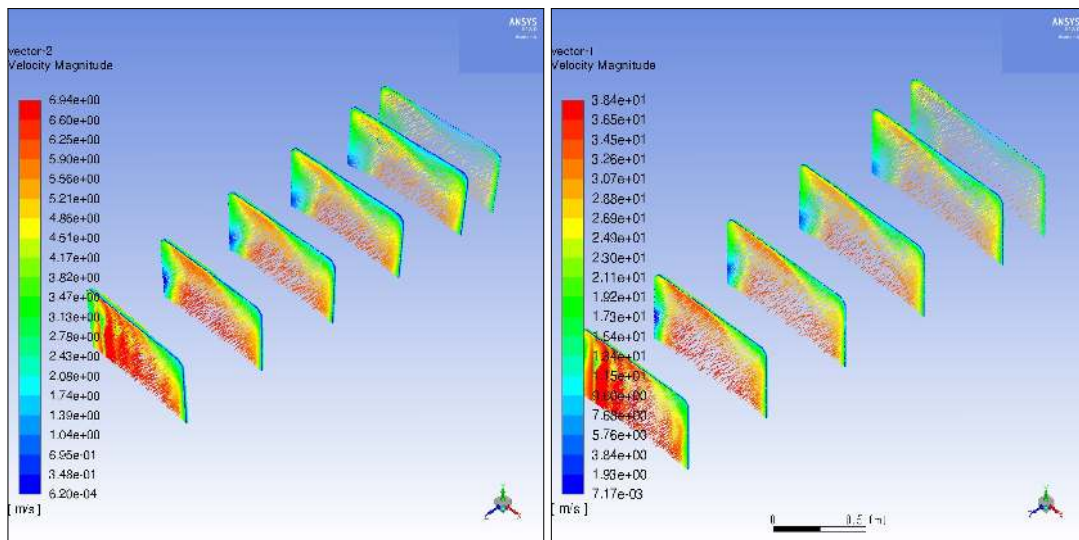
Figure 51: Contour plots of the $\overline{vv+2}$ Reynolds stresses on the symmetry-plane (from Ansys Fluent).



(a) Pressure difference of 25 Pa.

(b) Pressure difference of 725 Pa.

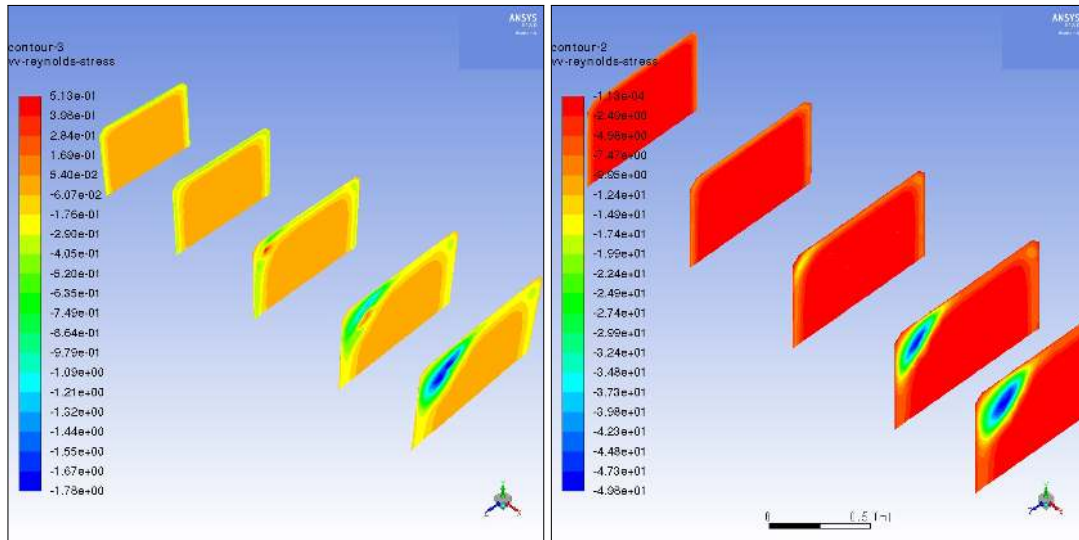
Figure 52: Velocity vector plots of the cross-section at different locations in the first diffuser (from Ansys Fluent).



(a) Pressure difference of 25 Pa.

(b) Pressure difference of 725 Pa.

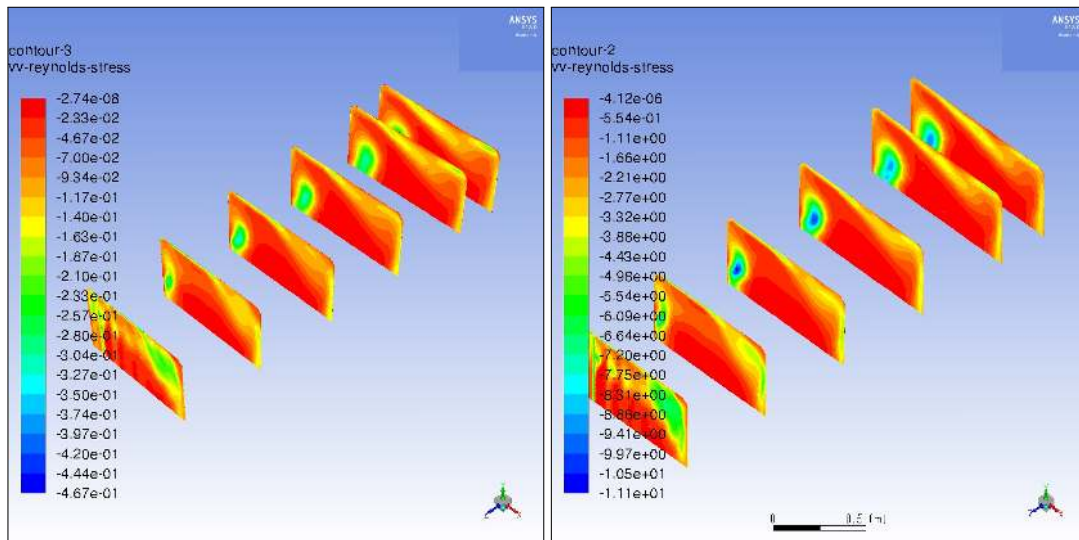
Figure 53: Velocity vector plots of the cross-section at different locations in the second diffuser (from Ansys Fluent).



(a) Pressure difference of 25 Pa.

(b) Pressure difference of 725 Pa.

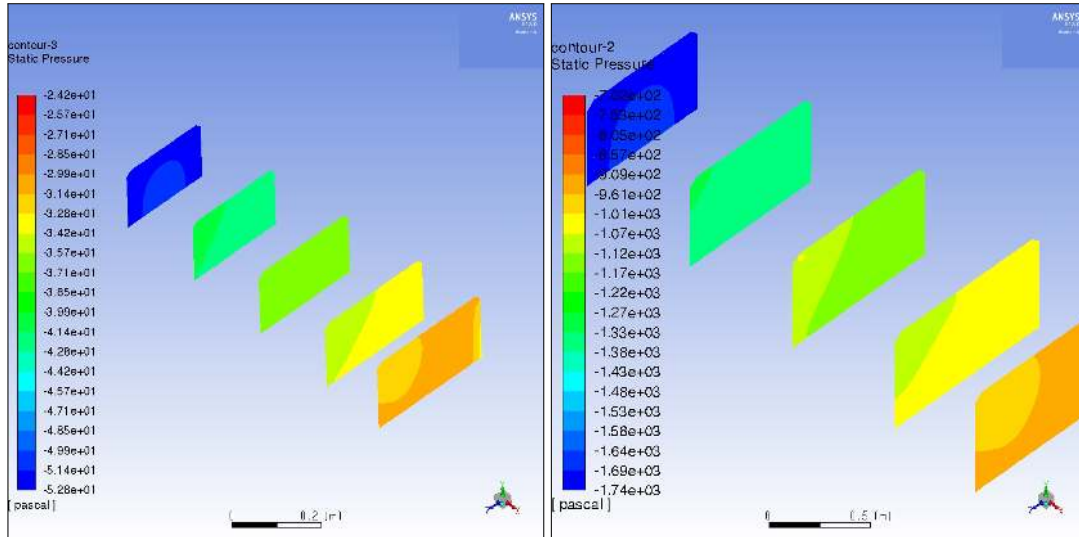
Figure 54: Contour plots of the $\overline{vv^{+2}}$ Reynolds stresses over the cross-sections at different locations in the first diffuser (from Ansys Fluent).



(a) Pressure difference of 25 Pa.

(b) Pressure difference of 725 Pa.

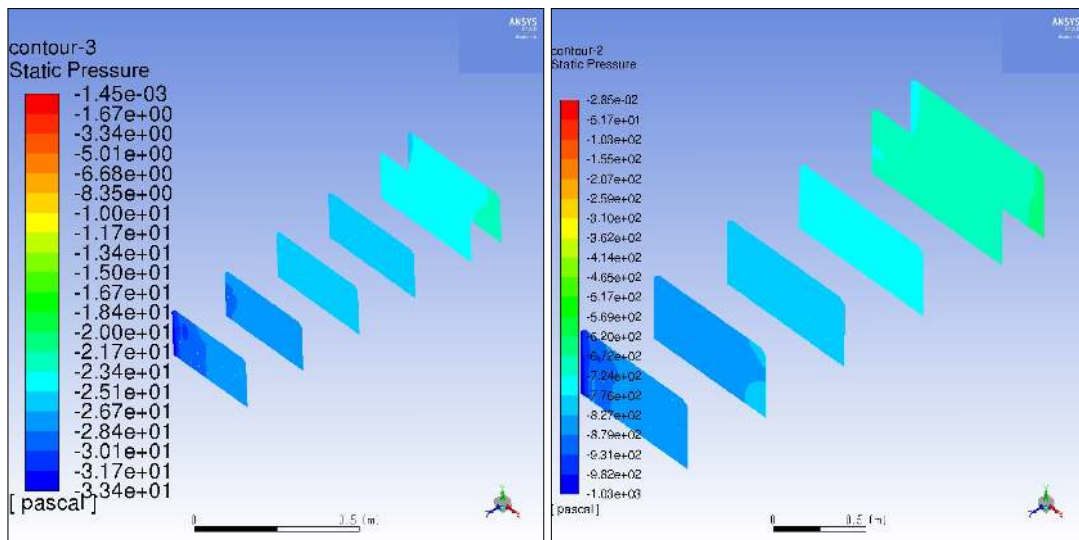
Figure 55: Contour plot of the $\overline{vv^{+2}}$ Reynolds stresses over the cross-sections at different locations in the second diffuser (from Ansys Fluent).



(a) Pressure difference of 25 Pa.

(b) Pressure difference of 725 Pa.

Figure 56: Contour plot of the static pressure over the cross-sections at different locations in the first diffuser (from Ansys Fluent).



(a) Pressure difference of 25 Pa.

(b) Pressure difference of 725 Pa.

Figure 57: Contour plot of the static pressure over the cross-sections at different locations in the second diffuser (from Ansys Fluent).

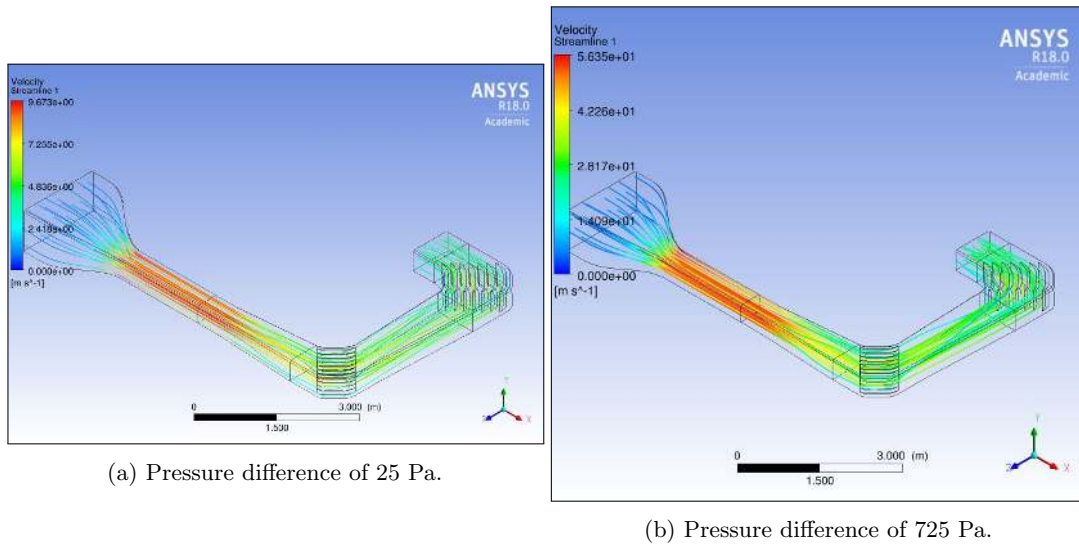


Figure 58: Streamline plot of the wind tunnel (from Ansys Fluent).

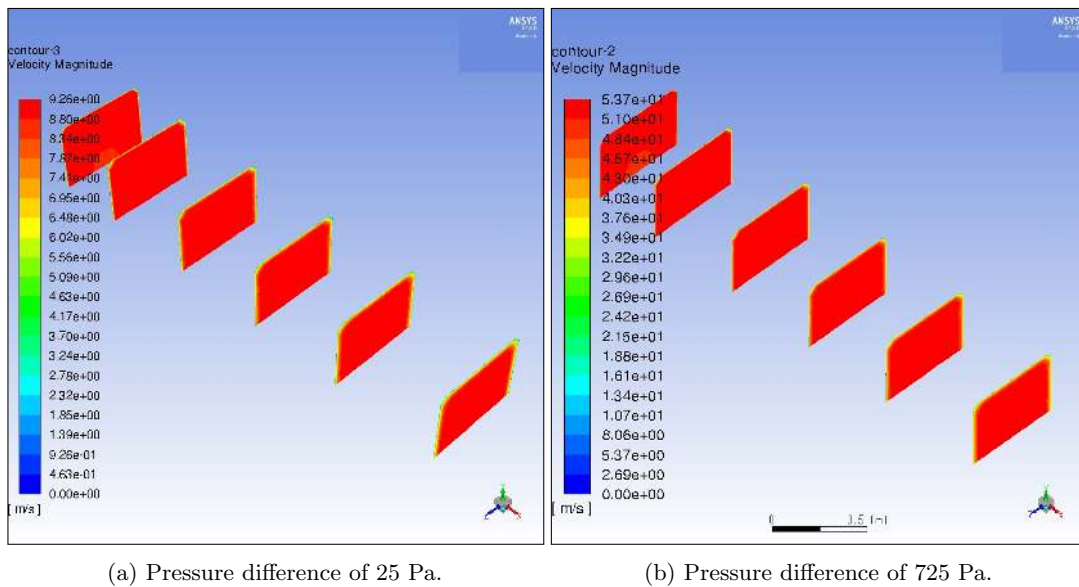
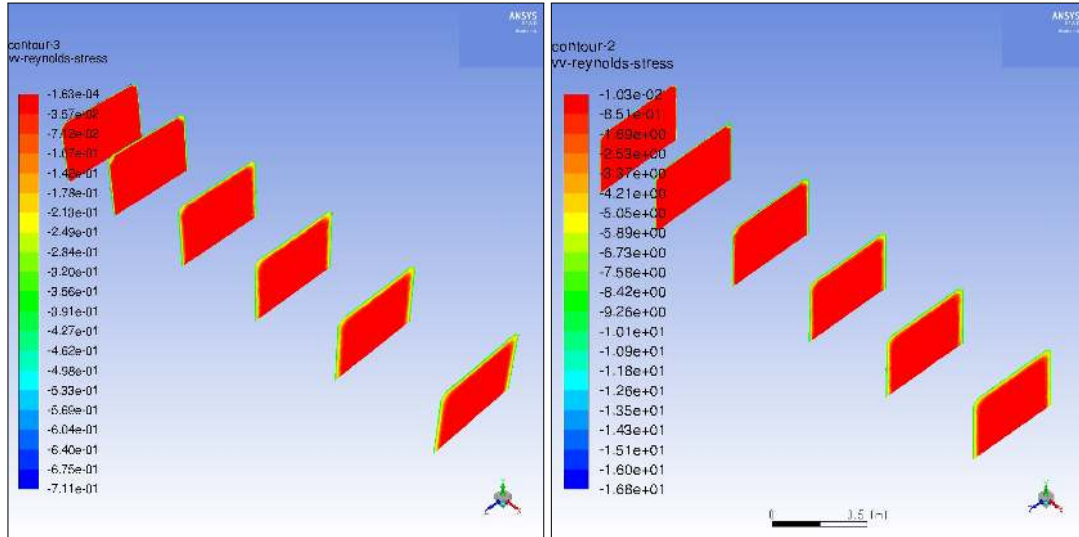


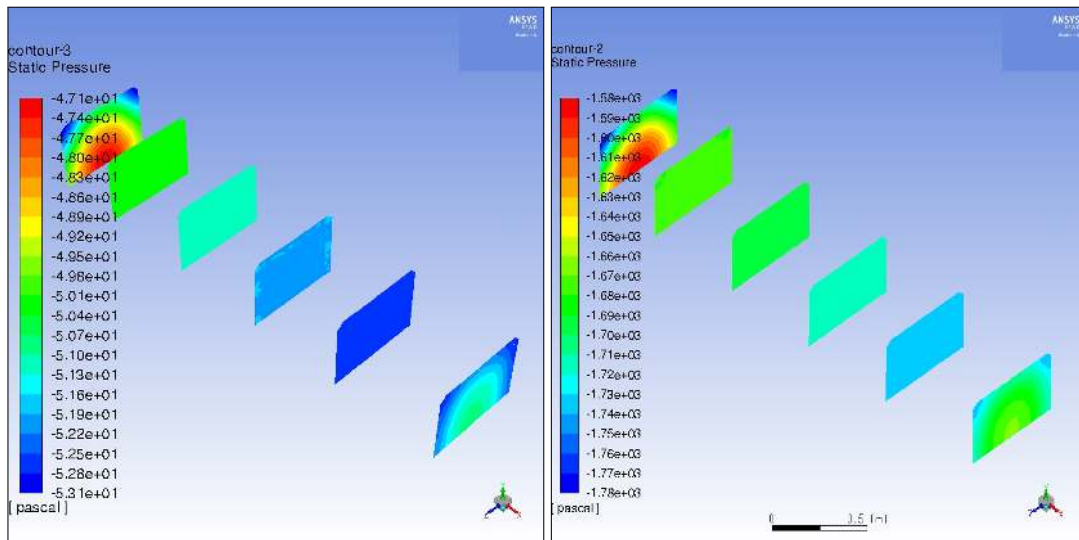
Figure 59: Velocity contour plot of the cross-section at different locations in the test section (from Ansys Fluent).



(a) Pressure difference of 25 Pa.

(b) Pressure difference of 725 Pa.

Figure 60: Contour plot of the $\overline{vv^{+2}}$ Reynolds stresses over the cross-sections at different locations in the test section (from Ansys Fluent).



(a) Pressure difference of 25 Pa.

(b) Pressure difference of 725 Pa.

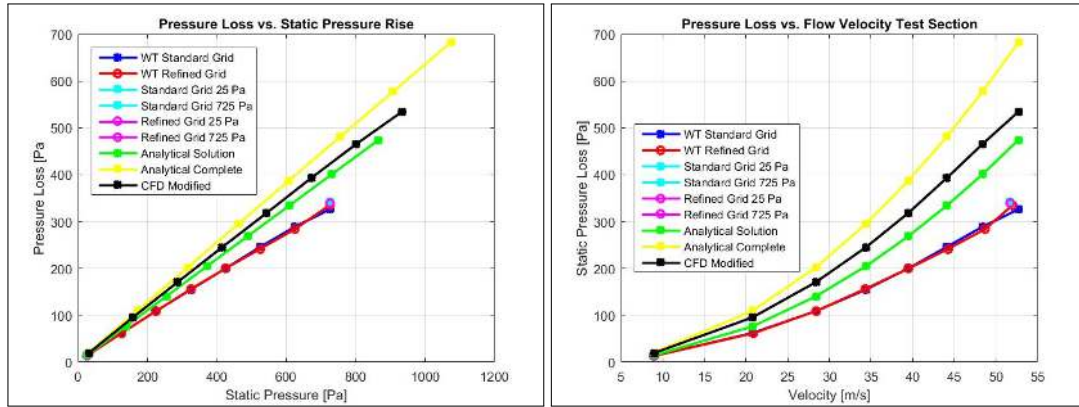
Figure 61: Contour plot of the static pressure over the cross-sections at different locations in the test section (from Ansys Fluent).

Table 3: Overview of the flow velocities, turbulence intensities and flow uniformities at different locations in the wind tunnel.

	Velocity [m/s]		Uniformity-Index [-]		Turbulence Intensity [%]	
	25 Pa	725 Pa	25 Pa	725 Pa	25 Pa	725 Pa
Inlet	1.04	6.08	0.976	0.978	1.00	1.00
Start Contraction	1.05	6.10	0.955	0.958	1.16	1.13
Exit Contraction	8.86	51.6	0.988	0.991	0.478	0.372
Start Test Section	8.86	51.6	0.983	0.989	0.719	0.526
Mid Test Section	8.86	51.6	0.971	0.980	1.25	0.876
Exit Test Section	8.69	51.6	0.960	0.972	1.69	1.21
Start 1st Corner	5.41	31.5	0.830	0.861	16.9	14.4
Exit 1st Corner	2.28	13.3	0.587	0.589	2.77	2.35
Start 2nd Corner	4.23	24.6	0.868	0.898	6.94	5.10
Exit 2nd Corner	4.24	24.7	0.923	0.939	5.63	4.62
Outlet	4.23	24.6	0.918	0.939	4.83	4.06

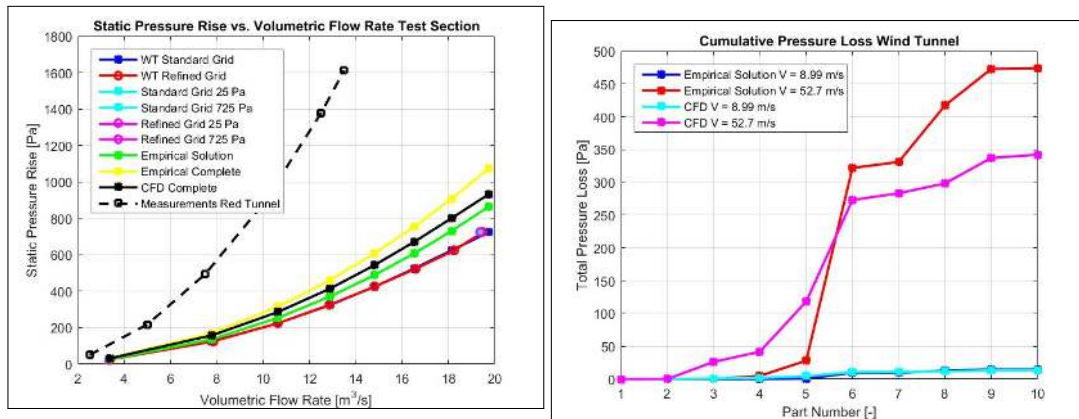
In Figure 62a the pressure loss as a function of the gauge pressure or static pressure rise is shown. Figures 62b and 63a show the pressure losses as a function of the flow velocity in the test section and the gauge pressure or static pressure rise as a function of volumetric flow rate in the test section, respectively.

In Figures 62a to 63a, pressure loss estimations derived from empirical data presented by (Eckert et al. 1976) are added. Besides the dimensions of the components that were determined in the previous, standard atmospheric conditions at sea level for density and dynamic viscosity and the theoretical flow velocities from continuity w.r.t. the flow velocity in the test section found by CFD were used. Contributions of the straight duct after the fan, the exit-diffuser and the four screens and its duct, as shown in Figure 1, along with the pressure loss from recovery at the exit were added to the CFD results and the already existing empirical estimations by using the same method and are shown as separate plots in Figures 62a to 63a too. For the screens, a porosity of 0.6 was assumed, along with wire radii of 0.7, 0.52, 0.33 and 0.15 millimeter. For extra comparison, measurements from pressure-tabs from the red wind tunnel are also shown in Figure 63a. It can be seen that the CFD results have the lowest estimation of the required pressure rise. The estimations from empirical data are slightly higher in term of pressure rise. The measurements in the red wind tunnel, on the other hand, show that a very high pressure rise is required compared to the other curves to attain the same flow velocities inside the test section. Figure 63b shows the cumulative pressure loss through the wind tunnel from inlet to outlet. Table 4 names the parts and as what number they can be found in Figure 63b. The largest differences in pressure losses from the two methods can be found in the contraction and the two diffusers.



(a) Total pressure loss of the wind tunnel as a function of static pressure rise. (b) Total pressure loss of the wind tunnel as a function of flow velocity inside the test section.

Figure 62: Pressure losses (from MatLab).



(a) Required static pressure rise for the wind tunnel as a function of volumetric flow rate inside the test section. (b) Cumulative pressure loss for all the separate wind tunnel parts from inlet to outlet.

Figure 63: Pressure losses (from MatLab)

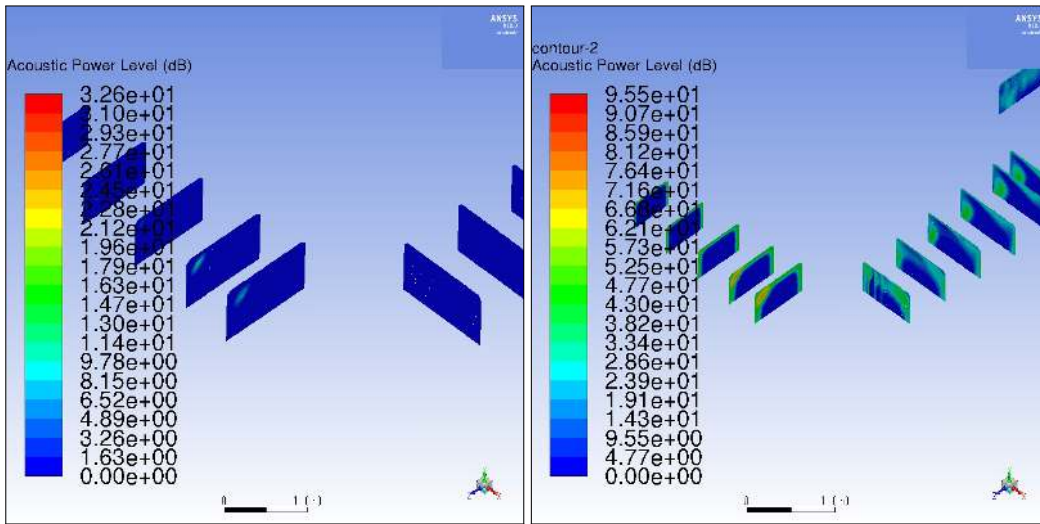
Table 4: Overview of the wind tunnel parts with their respective number in Figure 63b.

Number	Wind Tunnel Part
1-2	Settling Chamber
2-3	Contraction
3-4	Settling Duct
4-5	Test Section
5-6	First Diffuser
6-7	First Corner
7-8	Second Diffuser
8-9	Second Corner
9-10	Straight Duct

6.7 Aerodynamic Noise Sources

From a steady RANS solution, a prediction of the aerodynamically generated noise can be made in Fluent by using Lighthill's acoustic analogy. As a steady-state solution does not solve over time, the predictions are considered as broadband noise, where it is assumed that the acoustic energy is evenly distributed over a frequency-range, and does not, for example, allow for the identification of tonal noise. As stated in the Fluent User's Guide, the broadband noise source models purely identify the noise sources in, for example, terms of power and cannot predict how the noise would propagate up- or downstream. In the Fluent Theory Guide further information about the physics behind the acoustic broadband noise models can be found.

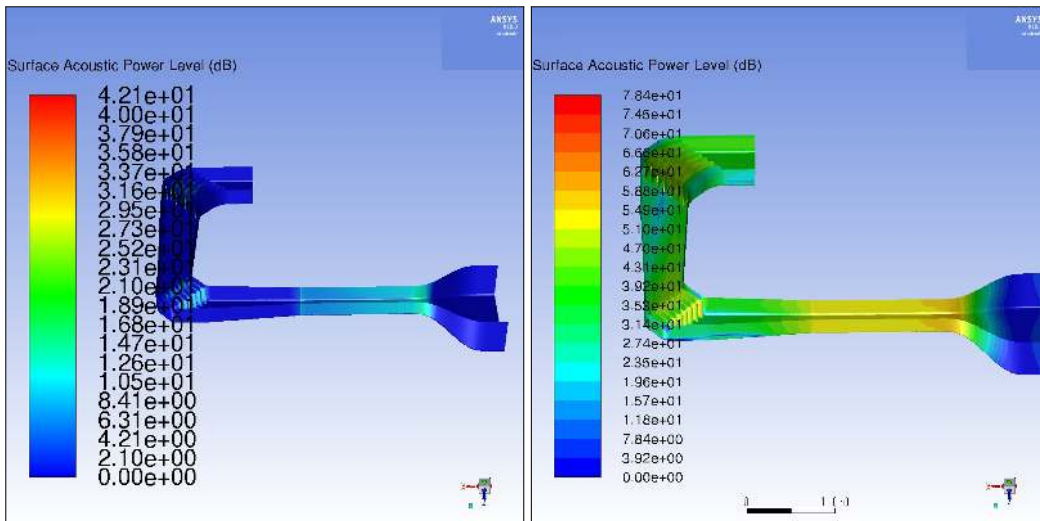
The first approximation of the aerodynamically generated noise was done by using Proudman's formula as formulated in the Fluent Theory Guide, where in terms of k and ω the acoustic power per unit isotropic turbulence is calculated. The power of the noise sources can be shown in Decibels by using the default $1e-12 W/m^3$ reference acoustic power in Fluent. In Figures 64a and 64b, the sound power level over different cross-sections between the first and second diffuser can be seen for gauge pressures of 25 Pa and 725 Pa, respectively. Only the two diffusers are shown as the turbulence kinetic energy and/or turbulence intensity are most significant in these parts. For the second approximation, a boundary layer noise source model was employed. Here, Fluent uses Curles integral in the form as shown in the Fluent Theory Guide to determine the local contribution of the wind tunnel surface to approximate the acoustic power in either W/m^2 or Decibels after normalizing it with the default reference value of W/m^2 . In Figures 65a and 65b the acoustic power level can be seen over the wind tunnel surfaces. In these Figures, the leading-edges of the corner vanes and the contraction exit are the most prominent noise sources.



(a) Pressure difference of 25 Pa.

(b) Pressure difference of 725 Pa.

Figure 64: Contour plots of the acoustic power level in Decibels found in the wind tunnel diffusers (from Ansys Fluent).



(a) Pressure difference of 25 Pa.

(b) Pressure difference of 725 Pa.

Figure 65: Contour plots of the acoustic power level in Decibels emitted by the surfaces in the wind tunnel (from Ansys Fluent).

6.8 Discussion of 3D CFD Results

At the points of convergence, figure 47 shows that the velocities inside the test section hardly change. Along with trend of the residual plots shown in figures 48a to 49b, it can be concluded that a steady-state solution adequately addresses the problem. The other cases converged in similar fashion.

The flow exiting the contraction can be seen settling in the short section before entering the test section. The flow conditions inside the test section appear to be acceptable, even though the uniformity indices of the flow velocity found inside the test section and turbulence intensities do not meet the desired numbers found in literature. The former can perhaps be explained by the fact that the consulted literature generally regarded big wind tunnels, where the area-ratio of the core-flow is relatively larger compared to the velocity profile near the wall. Whereas for the latter, it is expected that whenever turbulence screens are installed before the contraction the intensities will lower under the aforementioned 1% throughout the complete test section. The turbulence intensity is increasing along the length of the of the test section and is likely a result of the thickening of the boundary layer, which can be seen from both the plots where either velocity or Reynolds stresses over the cross-sections are shown. Walls with a slight divergence-angle should therefore be considered for the test section in order to compensate for this growth.

Whilst the flow from the inlet to end of the test section does not show any undesired effects, separation can be found in the first and second diffuser. Separation, especially in the first diffuser, is a problem as it generates noise and can propagate attenuated to the test section. Furthermore, the increased turbulence caused by the separation in the first diffuser will generate even more noise by its interaction with the leading-edges of the corner vanes as described in (Wagner 1996). In Figures 52a to 58b, it can be seen that the separation can be noticed halfway through the first diffuser. It is therefore likely that separation is caused by a combination of the increasing boundary layer thickness, an adverse pressure gradient and corner effects as can be seen in Figures 56a and 56b. Before chamfers were added to the corners over the cross-section of the wind tunnel and the transition edges were softened at the diffuser inlets, separation already started in the corner of the cross-section over the angle the first diffuser made with test section. For the second diffuser, increased Reynolds stresses and a pressure gradient can be seen to result in separation. Unlike before, the causes are less pronounced here than for the first diffuser. However, it is assumed that it is combination of the distorted flow from the separation in the first diffuser and the first corner and the pressure gradient result in separation in the second diffuser too.

In Figures 62a to 63a it can be seen that the CFD has lower estimation than the empirical prediction method presented in (Eckert et al. 1976), even

though the numbers are close and have generally the same trend in Figure 63b. Measurements showed that the red wind tunnel requires a much higher pressure rise than is predicted for the new tunnel to attain the same volumetric flow rates. The filter has been neglected in any of the estimations, as well as a conversion from a square to circular cross-section, stator vanes of the fan and obstructions subjected to the flow such as measurement equipment in the test section. However, the measurements showed pressure rises almost twice as large and it is not expected that the neglected aspects would account for that difference. It is therefore assumed that the high pressure rises are, amongst others a result of a somewhat inefficient wind tunnel design that causes high pressure losses. Improper screens and corner vanes design and placement and separation may have contributed to this. Other factors may be dust build-up inside the wind tunnel. As mentioned in the previous, the fan is powered by a motor of 42 kW. If the trend of the measurements is extrapolated to the maximum flow velocity of 65 m/s, which corresponds with a volumetric flow rate of $16.25 \text{ m}^3/\text{s}$ inside the test section of the wind tunnel, a pressure rise of over 2000 Pa would be required. This translates to a plausible efficiency of approximately 0.8 - 0.9 for the current motor-fan combination. Unless the fan is limited by the volume of air it can move, which is unlikely as axial fans are usually bounded by maximum pressure rise performance-wise, higher velocities than the aforementioned 43.3 meters per second or even 50 meters per second should be attainable inside the test section.

The interpretation of the sound power levels in these cases is not as straightforward as it would be for a receiver and sound pressure levels. From The Engineering Toolbox online, the boundary layer noise, that lies approximately at 40 and 70 dB for the low and high velocity cases, respectively, could be compared to the noise that a refrigerator and a vacuum cleaner produce at the lower and higher end, respectively. For the noise that the turbulence in the flow produces, the estimates lie between a refrigerator and a noisy shopping street or an air chisel, respectively. The comparison of sound power levels for the latter case, make the results somewhat unlikely and seem to be high approximations. However, it must not be forgotten that very small areas or volumes are seen to produce this sound power level. The effect and meaning it has on the receiver in terms of, for example, sound pressure level is not known. Then it must be taken into account that the models assume isotropic turbulence, that the flow is in stand still and the parameters are directly calculated from properties such as k and ω . The fact that there is a mean flow present that has been accelerated through a contraction, would already oppose the assumption of isotropic turbulence. Then there is chance of excessive approximation of turbulence because of the Boussinesq approximation, where the Reynolds stresses are proportional to the strain rate. Strong curvature, acceleration or deceleration may result in excessive production of turbulence kinetic energy. Even with the use of the curvature correction and production limiter, of which the latter only addresses the kinetic energy build-up at stagnation points according to the Fluent User's

Guide, the strong strain rates, and therefore turbulence kinetic energy build-, could still be found in the diffusers because of the expansion. It may therefore be an idea to use a different model for the 3D evaluation to see how those results would compare to the $k-\omega$ SST model, or to use the $k-\omega$ SST again with the Kato-launders limiter selected. It is needless to say that the separation seen in the diffusers may just be an over-prediction. When it turns out that there is still separation present after new evaluations or experiments, one or both diffusers require a redesign. All in all, the separation found in the second diffuser is most likely a consequence of the separation in the first. Meaning that the first diffuser is the key-point of interest. At the same time, it could be assumed that the corners function well enough in a 3D situation too, and that the lesser drifting of streamlines that is seen over the vanes of the first corner is also a consequence of the separation seen in the first diffuser.

7 Noise Measurements

In order to have a better understanding about noise propagation through a duct, an experiment was conducted where noise recordings were made at different locations along the duct of the red wind tunnel. Even though this wind tunnel would be removed from service, the results would still be able to tell something about noise propagation in general and the noise that the fan and motor produce, which will both be re-used for the new acoustic wind tunnel that will be built in this same study. The experiment may also give information about how the noise leaks through from one floor to the other. This is also of importance as the new wind tunnel, like the old tunnel, will also be built over two floors. The noise recordings are done at a range of velocities. These recordings were processed and used to create periodograms that would show the sound pressure level over a range of frequencies. Additionally, the noise in 1/3 octave spectra will be shown and correlations between measurements will be investigated. It is expected that low frequencies noise that stems from the motor and fan will be dominant at first. Higher frequency noise was expected to become increasingly prominent as aerodynamic induced noise increases drastically for higher flow velocities as written in (Wagner 1996).

7.1 Experiment Setup

In this experiment, seven microphones were used and the first step was placing them at different locations around the duct. The first microphone was placed one meter behind the outlet of the wind tunnel as can be seen in Figure 66. It was placed as such, that it would not be directly in the flow in order to avoid noise contamination from the air interacting with the microphone head. The second microphone was located just outside of the outlet as shown in Figure 67. Similarly to the first microphone, it was set up so that it would not interfere with the flow. The third microphone in Figure 68 was placed one half meter outside of the duct at the height of the fan. The fourth microphone was placed in a closed compartment adjacent to the test section. The microphone would be separated from the flow, but noise would still be able to propagate through the wall of the test section. Figure 69 shows the location of the fourth microphone. The fifth microphone was placed outside of the wind tunnel directly on the right side of the test section as can be seen in Figure 70. The sixth and seventh microphone, of which the location can be seen in Figures 71 and 72, respectively, were placed in the vicinity of the tunnel inlet. The sixth microphone was directly placed in the middle of the inlet, whilst the seventh was placed a meter away from the inlet on the right side. Figure 73 shows a simple schematic with all the microphone locations with respect to the tunnel.

The noise that is picked up by the microphones, is directed to a computer where the signal is sampled with a sample frequency of 25600 Hertz. The sampling is done for each microphone-channel separately. The samples of all

separate channels would be saved in one data-file and made up one recording. MatLab would be able to read and play back these sound files later on.



Figure 66: The first microphone, which can be found near the tunnel outlet.



Figure 67: The second microphone, which is located next to the tunnel outlet.



Figure 68: The third microphone, which is placed next to the fan and motor outside of the tunnel.



Figure 69: The fourth microphone, which is placed in a separate compartment underneath the test section.



Figure 70: The fifth microphone, which stands next to the test section of the tunnel.



Figure 71: The sixth microphone, which is placed directly in front of the inlet of the tunnel.



Figure 72: The seventh microphone, which is located some distance away from the inlet.

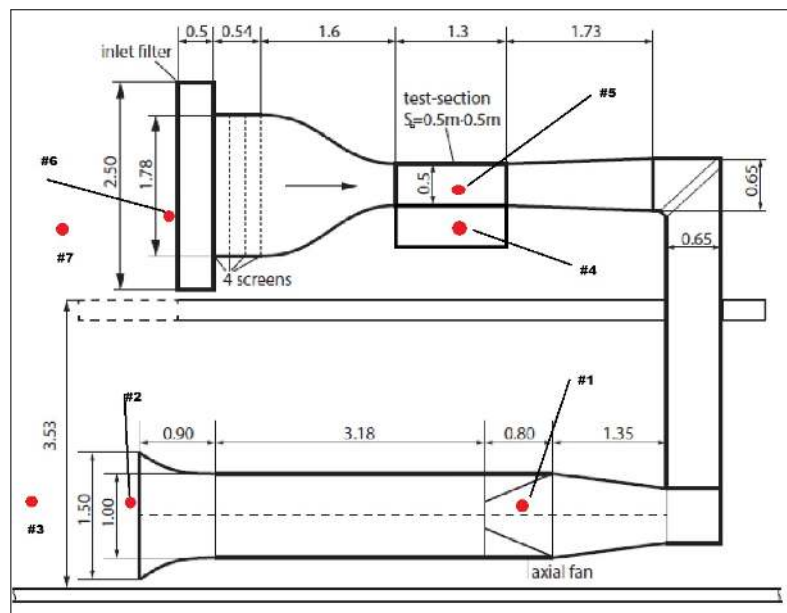


Figure 73: Schematic of the microphones that are placed around the wind tunnel.

7.2 Noise Recordings

The purpose of the experiment was to generate noise spectra for the recordings at each microphone at flow velocities running from 0 to 60 meters per second with intervals of 10 meters per second. At each velocity, 4 recordings of 2 minutes were made. In order to process these recordings, the recordings had to be played back first. The experiments were conducted in the day time and the hall was, of course, open and free to use. It was therefore required to listen back to all the microphone channels of the recording in order to check whether any noise, like opening and closing doors for example, would affect the recordings and spoil the subsequent noise spectra. Since listening back to all the channels and recordings separately would be very time consuming, Only the first and fifth microphone were used or this playback evaluation as they cover they basement and ground floor, respectively, on which the wind tunnel is located. Here it was assumed that these two microphones would pick up all significant irregularities from the background and account for all the other channels too. Table 6 shows the experiment log and Table 5 recording times. In order to be certain about the presence of a velocity-equilibrium, recordings samples were chosen for initial playback that lied well in the velocity interval during the experiment. This corresponded with recordings 6, 10, 14, 18, 22, 26 and 30. From playback it turned out that all recordings were not spoiled and could be used for further evaluation. The playback was done with the *Sound* function in *MatLab*.

Table 5: Number and time of the recordings.

Recording Number and Initiation Time							
Number	Time	Number	Time	Number	Time	Number	Time
1	12:16	9	12:32	17	12:48	25	13:04
2	12:18	10	12:34	18	12:50	26	13:06
3	12:20	11	12:36	19	12:52	27	13:08
4	12:22	12	12:38	20	12:54	28	13:10
5	12:24	13	12:40	21	12:56	29	13:12
6	12:26	14	12:42	22	12:58	30	13:14
7	12:28	15	12:44	23	13:00	31	13:16
8	12:30	16	12:46	24	13:02	32	13:18

Table 6: Recording log.

Wind Tunnel Status and Time	
Time	Wind Tunnel Status
12:16	Background Noise
12:17	Closed Tunnel Window
-	Wind Tunnel Start
12:23	Idle
12:31	Test Section 10 m/s
12:40	Test Section 20 m/s
12:48	Test Section 30 m/s
12:56	Test Section 40 m/s
13:04	Test Section 50 m/s
13:12	Test Section 60 m/s
13:19	Idle

7.3 Noise Post-Processing

The Welch method was used to do the spectrum analysis as it could be used to estimate the sound pressure level at different frequencies and offer a better solution (less variance) than Bartlett's method at the cost of a lower frequency resolution as in (Fowler n.d.). The Welch method estimates the power spectral density by dividing the audio-signal up in different segments, which overlap each other as explained in (Mathworks n.d.). Then, periodograms of each segment are made by doing a discrete Fourier transform. After which, ultimately, the average of the power spectral densities are found. In MatLab, this can be done by the built-in *pwelch* function, which returns the power spectral density per frequency as a function of the audio-signal, window-size, overlap, discretization refinement and sample frequency. By inserting the output of the power spectral density function with Equation 14, the sound pressure level over the frequency range could be found.

$$SPL = 20 \log\left(\frac{p}{p_{ref}}\right) dB \quad (14)$$

Where p is the registered pressure by the microphones and p_{ref} is the reference pressure of $2 \cdot 10^{-5}$, which is the lowest noticeable pressure difference by the human ear. With a sampling frequency of 25600 Hertz, a overlap of 0.5 and the number of discrete Fourier points at 512, the Welch method would return spectra up to 12800 Hertz (Nyquist frequency) with instances of 25 Hertz.

7.4 Results

Figure 74 shows the sound pressure levels for when the wind tunnel was switched off and it is the periodogram of the first recording listed in Table 6. Figures 75 to 80 show the periodograms of the wind tunnel noise with the background noise subtracted for flow velocities from 10 to 60 meters per second. Figures 81 to 87 show the frequency band-spectra, where the frequency-range is split up into 1/3 octave-bands for when the wind tunnel is switched off and then for flow velocities from 10 to 60 meters per second. Figures 88 to 94 show the noise spectra at different velocities for microphones 1 to 7, respectively. Also for the band-spectra and the periodograms of each separate microphone, the background noise was subtracted from the measurements for when the wind tunnel was in operation. For clarity, this subtraction was done by subtracting pressures and not sound pressure levels.

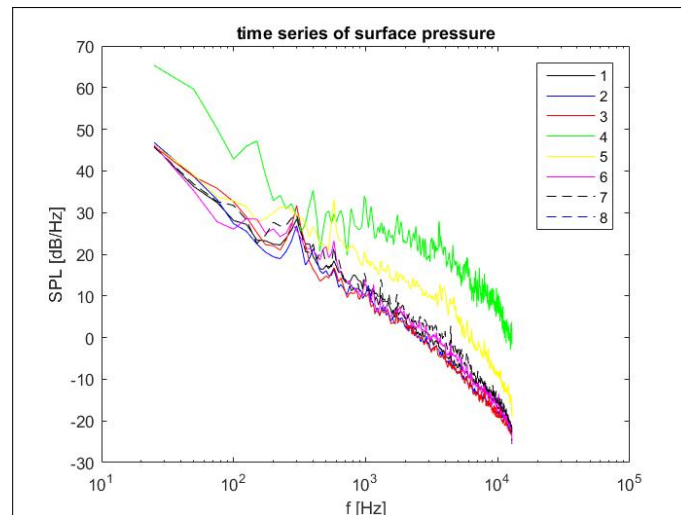


Figure 74: Periodogram of the measured noise for when the wind tunnel is switched off (from MatLab).

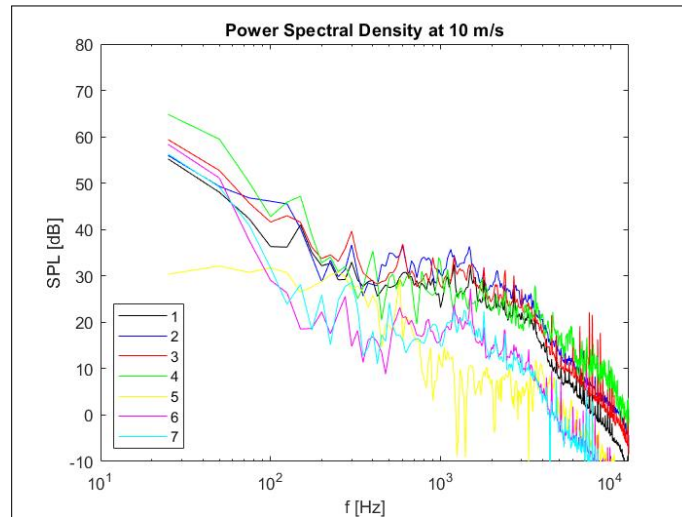


Figure 75: Periodogram of the measured noise at a flow velocity of 10 meters per second in the test section and the background noise subtracted (from MatLab).

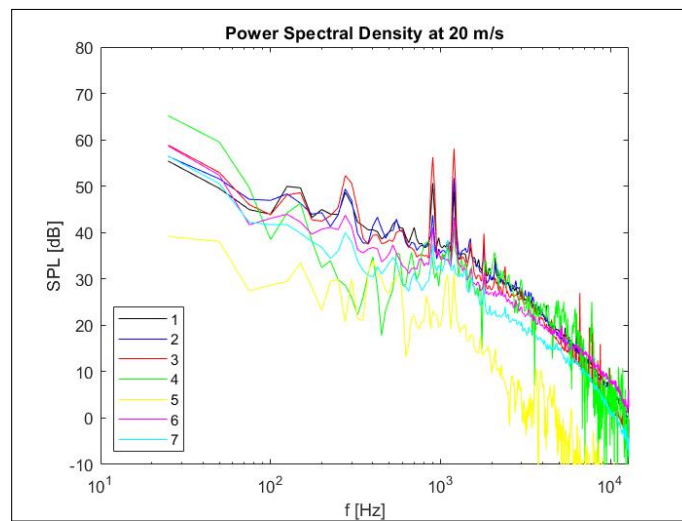


Figure 76: Periodogram of the measured noise at a flow velocity of 20 meters per second in the test section and the background noise subtracted (from MatLab).

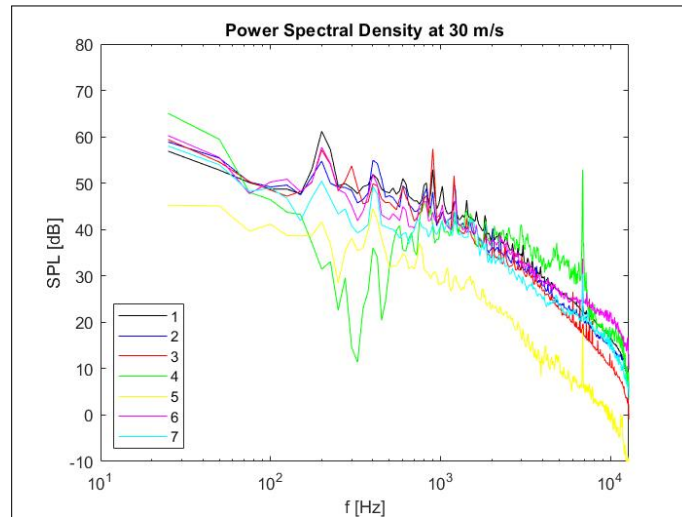


Figure 77: Periodogram of the measured noise at a flow velocity of 30 meters per second in the test section and the background noise subtracted (from MatLab).

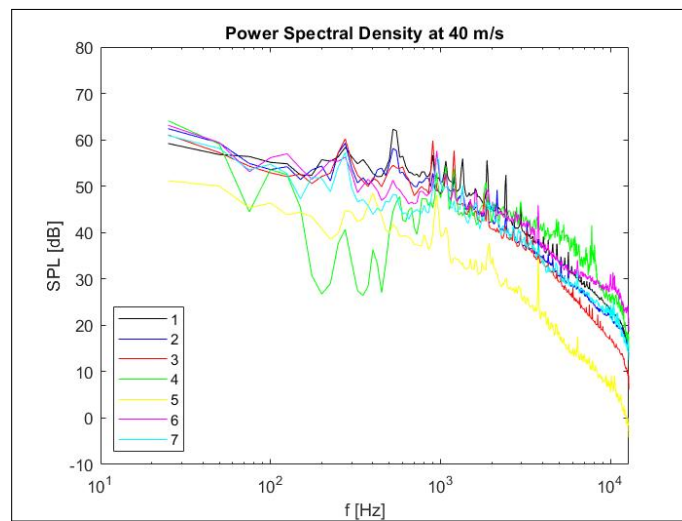


Figure 78: Periodogram of the measured noise at a flow velocity of 40 meters per second in the test section and the background noise subtracted (from MatLab).

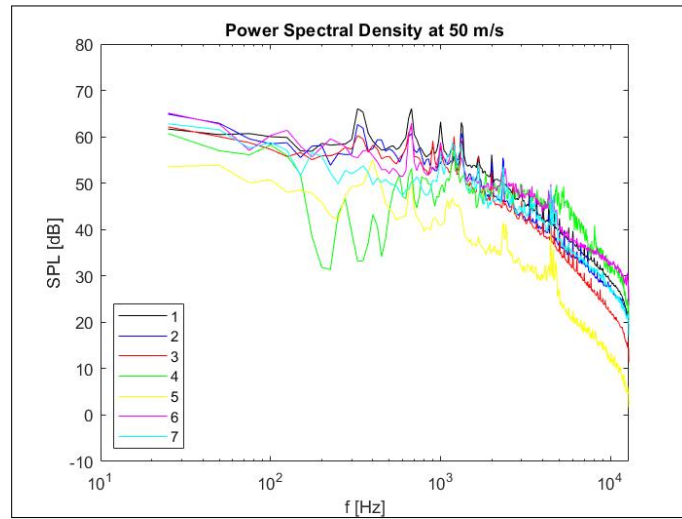


Figure 79: Periodogram of the measured noise at a flow velocity of 50 meters per second in the test section and the background noise subtracted (from MatLab).

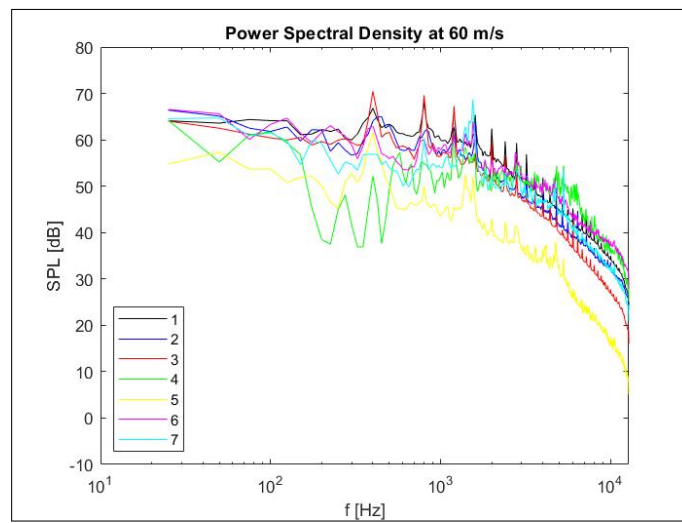


Figure 80: Periodogram of the measured noise at a flow velocity of 60 meters per second in the test section and the background noise subtracted (from MatLab).

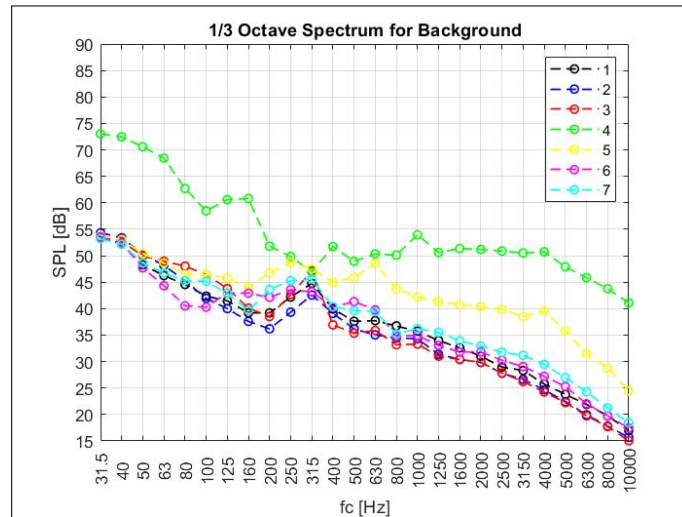


Figure 81: The noise for when the wind tunnel is switched off, shown in 1/3 octave-bands (from MatLab).

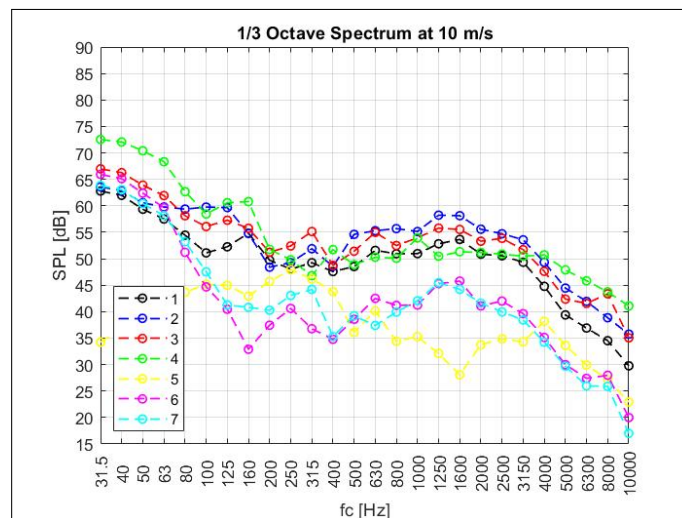


Figure 82: The noise at a flow velocity of 10 meters per second, with the background noise subtracted, shown in 1/3 octave-bands (from MatLab).

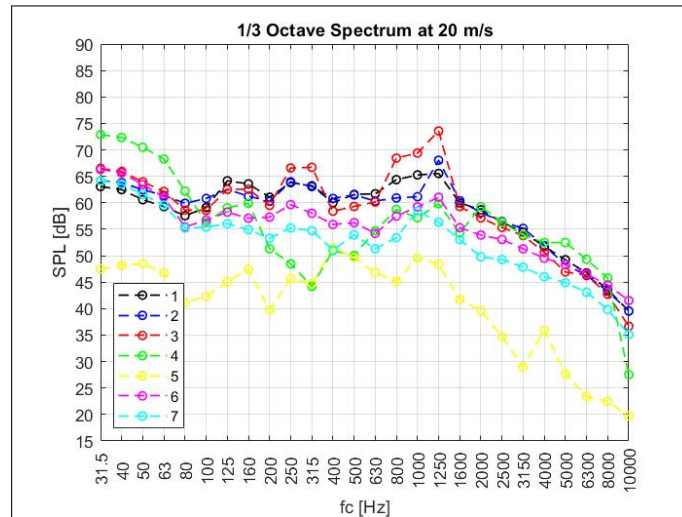


Figure 83: The noise at a flow velocity of 20 meters per second, with the background noise subtracted, shown in 1/3 octave-bands (from MatLab).

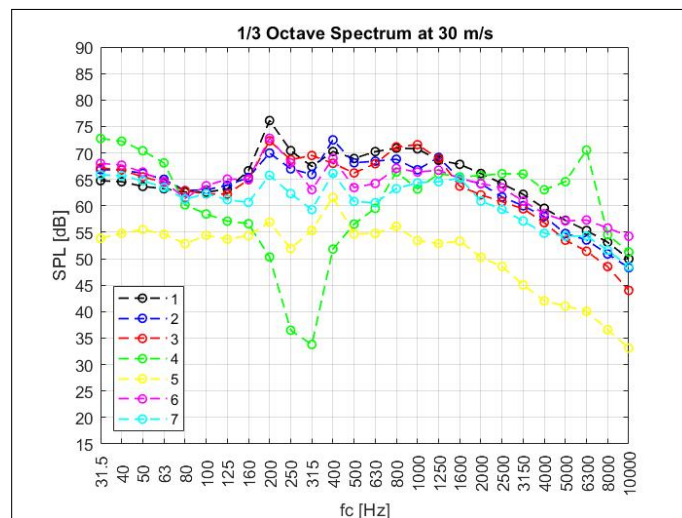


Figure 84: The noise at a flow velocity of 30 meters per second, with the background noise subtracted, shown in 1/3 octave-bands (from MatLab).

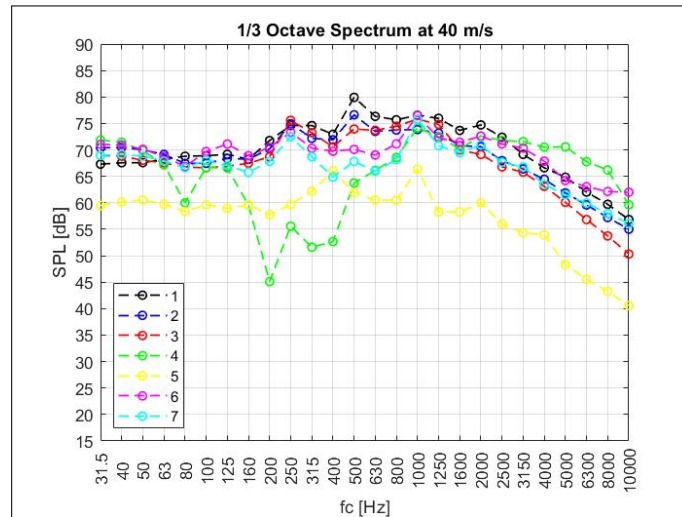


Figure 85: The noise at a flow velocity of 40 meters per second, with the background noise subtracted, shown in 1/3 octave-bands (from MatLab).

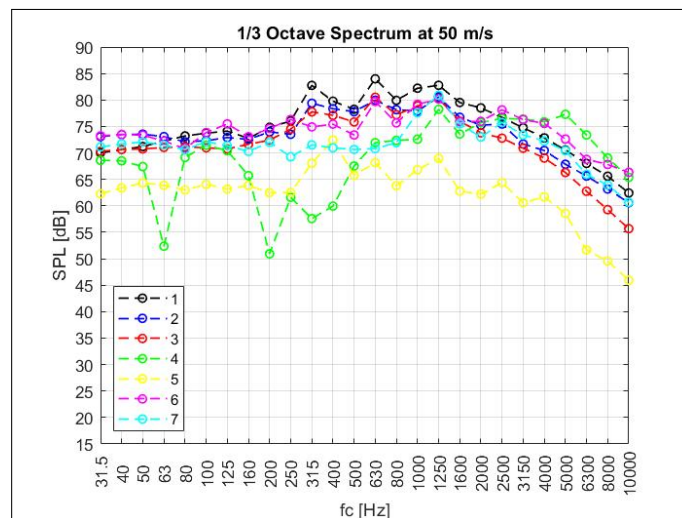


Figure 86: The noise at a flow velocity of 50 meters per second, with the background noise subtracted, shown in 1/3 octave-bands (from MatLab).

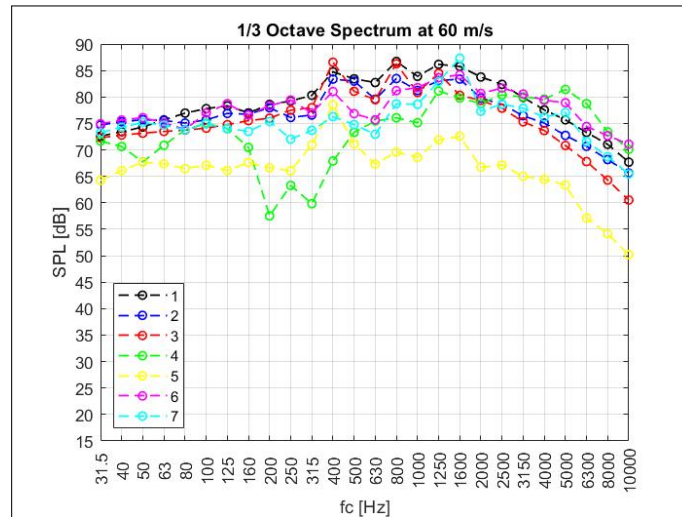


Figure 87: The noise at a flow velocity of 60 meters per second, with the background noise subtracted, shown in 1/3 octave-bands (from MatLab).

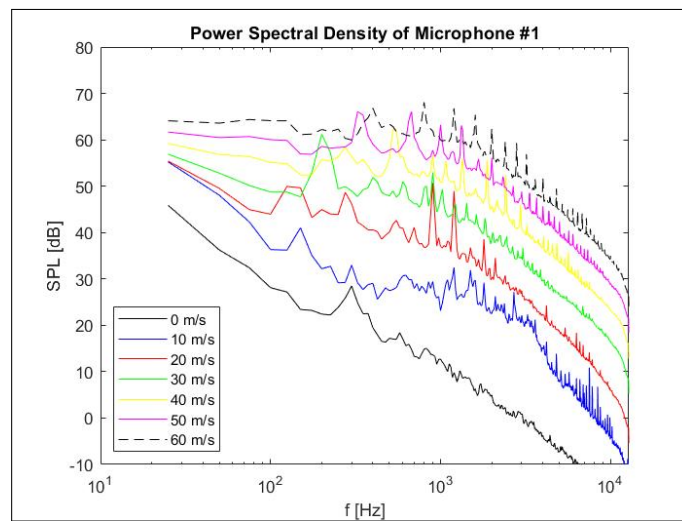


Figure 88: Periodogram of the noise recorded by the first microphone and the background noise subtracted for different flow velocities (from MatLab).

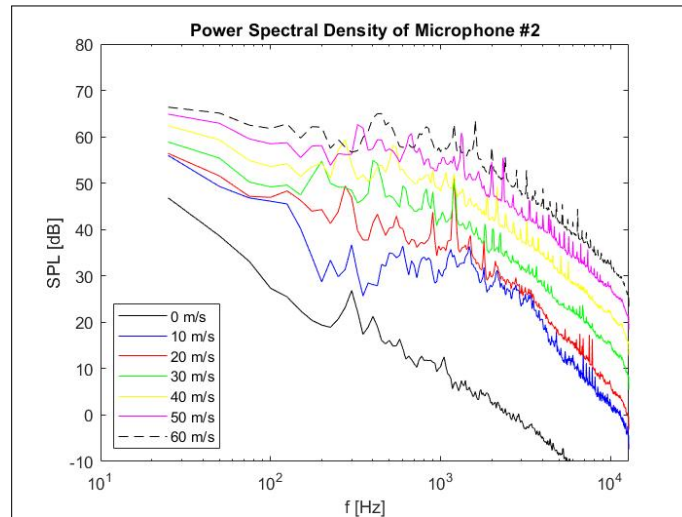


Figure 89: Periodogram of the noise recorded by the second microphone and the background noise subtracted for different flow velocities (from MatLab).

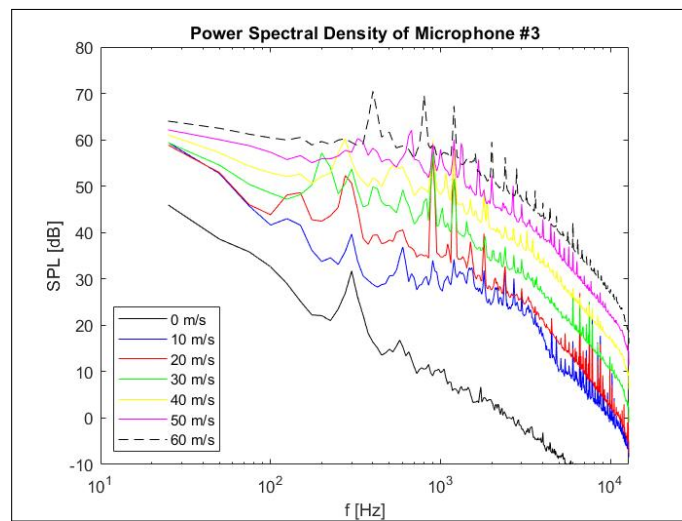


Figure 90: Periodogram of the noise recorded by the third microphone and the background noise subtracted for different flow velocities (from MatLab).

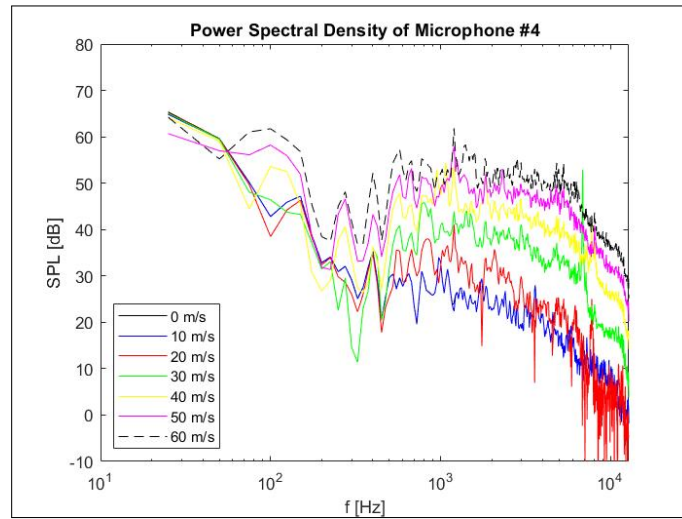


Figure 91: Periodogram of the noise recorded by the fourth microphone and the background noise subtracted for different flow velocities (from MatLab).

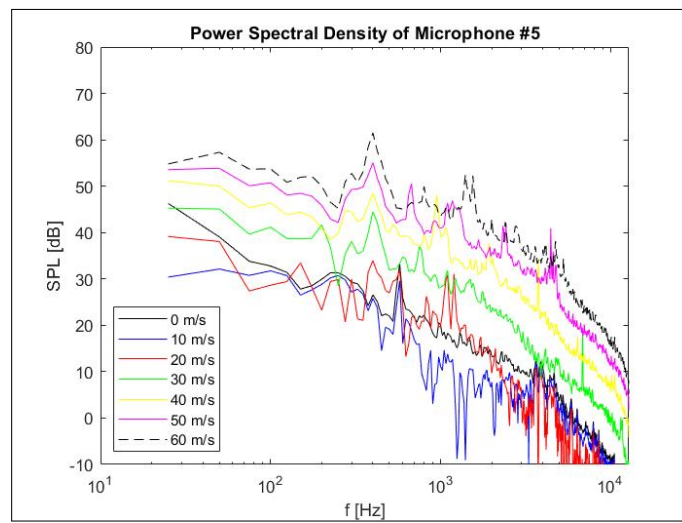


Figure 92: Periodogram of the noise recorded by the fifth microphone and the background noise subtracted for different flow velocities (from MatLab).

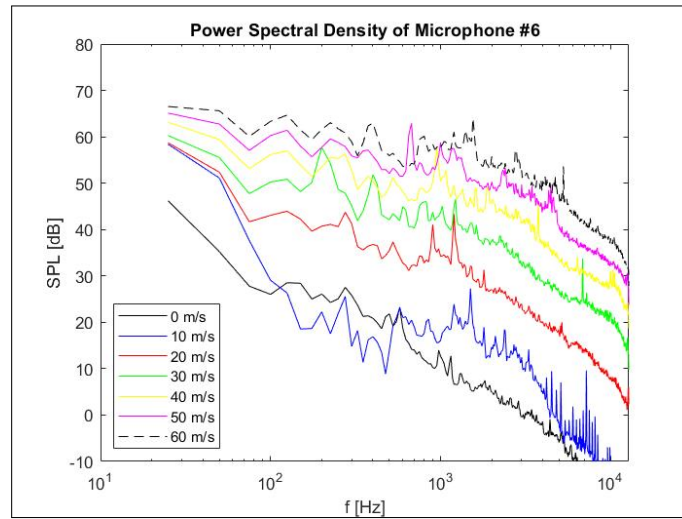


Figure 93: Periodogram of the noise recorded by the sixth microphone and the background noise subtracted for different flow velocities (from MatLab).

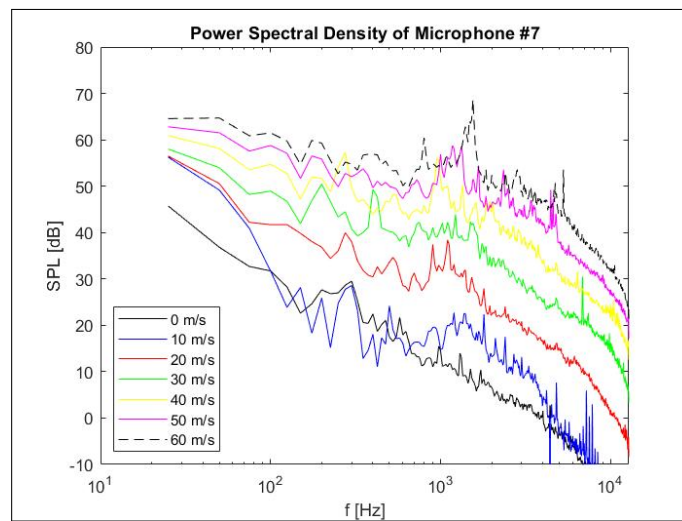


Figure 94: Periodogram of the noise recorded by the seventh microphone and the background noise subtracted for different flow velocities (from MatLab).

7.5 Conclusion and Discussion of Measurement Results

Microphones 4 and 5 record higher sound pressure levels over the audible frequency range for when the wind tunnel is idle. This may be a result of the increased activity in the main hall. The other microphones are shielded from this in this case by (movable) walls. It can be observed that the microphones record a similar envelope the frequency-range. A "bucket" can be observed in the periodogram of the fourth microphone, where noise of frequencies between 200 and 500 appear to be rather low. The fifth microphone registers lower sound pressure levels than all the other microphones for when the wind tunnel is in operation. An explanation for this could be the fact that it is not placed close to both the in- and outlet, nor in an adjacent chamber to the duct. It has to be kept in mind, again, that the inlet is shielded off by movable walls and the outlet is placed in a small basement, whilst the fifth microphone is placed rather isolated from places where the noise can easily reach to. Between 200 and 500 Hertz again, the fourth microphone registers significantly lower sound pressure levels. This may be a consequence of the test section wall that works as a filter for those noise frequencies. The sixth and seventh microphone generally have the same envelope as the first, second and third microphone, but they record somewhat lower sound pressure levels.

It can also be seen in Figures 75 to 80 that the noise shows itself primarily in three to five peaks between 300 and 2000 Hertz and one cluster of peaks around 8000 Hertz at first. These noise peaks are likely to stem from the motor and fan combination as the first three microphones record the highest sound pressure levels for these peaks. With increased flow velocity, smaller peaks appear for frequencies over 1000 Hertz. The sound pressure levels for the fourth channel increase for the mid- to high-frequency range. The sound pressure levels of the sixth and seventh channel also increase for higher frequencies, but not as strongly. The erratic behaviour the envelope of the periodogram of the fourth channel may be a consequence of the fact that it is located in a tight compartment adjacent to the test section. Reverberation is likely to play a role here. In general, the rise of higher frequency noise with increased flow velocity in the tunnel is possibly to be a result of self-noise inside the tunnel duct, from the flow going over the corner vanes for example, as (Thomas F. Brooks & Marcolini 1989) and (H. Arbey 1983) have shown that (untripped) airfoils mostly produce noise of higher frequencies too for low angles of attack. Another argument for this, is that the third microphone, next to the motor and fan on the outside of the wind tunnel, records much lower sound pressure levels for these high frequencies and the envelope of the periodogram there is quite dissimilar.

Figures 81 to 87 show the 1/3 octave spectra, where the frequency range is split up into 1/3 octave-bands. The spectra should be easier to analyse this way as the individual peaks are filtered out and not every frequency requires to be analysed individually. In Figure 81 it can be seen as well that the fourth and fifth microphone show higher sound pressure levels. The other five microphones

show the same trend over the bands with a small peak at a center frequency of 315 Hertz. For when the wind tunnel is in operation, the fifth microphone records the lowest sound pressure levels and generally follows the envelope of the first three and last two microphones over the bands for the different velocities. The last two microphones initially record lower sound pressure levels than the first three channels, but for increased velocity this will turn around for the very low and higher octave bands. Also the fourth microphone records higher sound pressure levels for the octave bands with higher center frequencies. Furthermore, it can be noticed that for the first three and two last microphones peaks at center frequencies of 160, 630 and 1250 Hertz start to appear besides the one at 315 Hertz when the wind tunnel is in operation. These peaks seem to shift to higher frequencies with increased flow velocity.

Figures 88 to 94 show the noise spectra at different velocities for microphones 1 to 7, respectively. It can be clearly seen that the sound pressure levels recorded by all the microphones increase for increased flow velocities. Whilst the envelope of the periodograms of the fourth and fifth microphones remain largely unchanged, the periodograms for the first, third, sixth and seventh microphones show that some of the peaks change significantly for different flow velocities. For microphone one and three in particular, there are two strong peaks just over a 1000 Hertz that appear rather suddenly at a velocity of 20 meters per second in the test section. These weaken somewhat and become stronger again for velocities of 50-60 meters per second. This may indicate resonance. For the same two microphones, many small peaks appear from 50 meters per second on between 2000 and 5000 Hertz. For the first three and the last two microphones, the peaks seem to shift slightly to higher frequencies with higher flow velocities.

(Donald A. Dietrich & Abbott 1977) and (L.D. Santana 2014) made similar noise measurements. The first paper regards a study to the acoustic signatures of a turbofan engine. The second paper is a report on the acoustic treatment for an anechoic wind tunnel. In both papers, multiple peaks can be observed throughout the spectra, similarly to the peaks found in this study. In these papers, there is a similar shift to higher frequencies for higher flow velocities or, analogically, an increase in revolutions per minute of the fan. The peaks are the tonal noise from the fan, which is a consequence of the blades passing the struts of the fan as explained in (Wagner 1996). The amount of peaks and their respective frequency are dependent on the amount of blades, struts and the revolutions per minute. Naturally, the frequency of the noise increases if the frequency of rotation is increased, which is, of course, the case for higher flow velocities. The fact that this frequency shift was only visible for higher flow velocities, may be a consequence of the fan operating beyond its design rotational speed where the loss in efficiency is compensated by a high rpm. All in all, judging from the comparison with other measurements, it can be concluded at this point that the dominant noise source during the measurements of this project was the fan.

(L.D. Santana 2014) presents plots of the noise spectrum at a flow velocity of 15, 31 and 37 meters per second. The second plot shows a very strong peak at approximately 200 Hertz, which is over 20 *dB* less strong in the first plot and is almost completely faded away in the third. This may, just like at the peaks found at a flow velocity of 20 meters per second in this experiment, indicate resonance. However, due to the lack of additional information, an explicit conclusion cannot be made regarding this. The acoustic treatment presented in (L.D. Santana 2014) shows that acoustic lining inside the fan-duct is effective for frequencies above 400 Hertz at 15 meters per second and frequencies above 700 Hertz at 37 meters per second. Baffle mufflers are used as extra treatment in this study and find their effectiveness mostly at lower flow velocities. In all presented situations, the combination of acoustic treatment used in this study is unable to counter the significant tonal noise from the first three peaks, but the sound pressure levels of the peaks above the aforementioned frequencies are successfully lowered. It may also be worth mentioned that also in (L.D. Santana 2014) a cluster of peaks can be found around 7-8 kHz, similarly to the measurements in this study. These clusters remain present in the three periodograms, but the baffle mufflers appear to be very effective in damping these specific peaks. Since the fan is the foremost noise source, it would be worthwhile to find its performance parameters, such as rpm, and place those next to the noise measurements.

The noise going through the elephant-hole also remains a point of interest and it is important to know how the noise propagates from the basement to the ground floor. In other words, what share of the noise that is recorded travelled through the duct upstream or went up through the elephant-hole. The fifth microphone shows periodograms that have an envelope that is similar to the microphones in the basement. The sound pressure levels are much lower however. Also the sixth and seventh microphone have similar envelopes to those in the basement. Whether the noise traveled through the duct or went up through the elephant-hole, could possibly be determined by calculating correlation-coefficients and the cross-correlation between the microphones. The correlation-coefficients between the periodograms of the microphones, could tell the degree of similarity between the measurements of each microphone.

Table 7 shows a table of correlation-coefficients between all the microphones. For these coefficients, the whole range of flow velocities have been taken into account. It can clearly be seen that the microphones closest to each other share the highest coefficients. The fourth microphone has the lowest correlation coefficients and this is likely a consequence of the reverberation in its tight compartment in combination with its physical separation from the fan and motor. Another explanation is that the noise it records comes mostly from the flow after all. In general, the coefficients for the seventh microphone are low and are even lower than for the fifth, despite the remote location of the microphone. For the sixth microphone they're rather high, which was unexpected as it was believed, with its location right in front of the inlet, that self-noise and noise

propagating through the duct would have had a considerable effect.

The cross-correlation of the measured time-signals could be used to find the lag between the microphones in their recordings and in turn be used to calculate a distance between the microphones (which is the cause of this lag) by dividing the lag by the sampling frequency and multiplying it again by the speed of sound. This distance may be able to assist in determining whether the noise traveled through the duct or went up through the elephant-hole. For example, if the cross-correlation between the first and seventh microphone is on the order of ten meters and not meters, it is likely that the noise has propagated through the duct. Table 8 shows the distances that are calculated from the lag in the time-signals. Short distances of a couple of meters between the first three and last two microphone do correspond with the setup that is used. Distances between first three microphones and the fourth or fifth microphone are way too large however and there is no real consistency between the numbers in general. It could be that the noise reaches the fifth and fourth microphone only after a couple of reflections, hence the calculated distances appear to be so high, but this explanation seems to be rather far-fetched. With multiple noise sources present, reverberation etc. it was already expected that the noise would most likely turn out to be uncorrelated. The measurements of the low velocity of 10 meters per second in the test section was already used to anticipate possible noise reflections, but then it still proved to be no help in finding some more valuable numbers. Also with the correlation-coefficients from the periodograms, frequency-shifts may have contaminated the numbers. It is somewhat likely that a large part of the noise from the basement leaks through the elephant-hole to the ground floor and propagation to the duct is limited.

Table 7: Correlation coefficients between all microphones from the complete range of velocities.

		Microphone						
		1	2	3	4	5	6	7
Microphone	1	1.00	0.85	0.81	0.19	0.61	0.73	0.47
	2	0.85	1.00	0.68	0.14	0.68	0.83	0.56
	3	0.81	0.68	1.00	0.09	0.75	0.58	0.33
	4	0.19	0.14	0.09	1.00	0.12	0.14	0.13
	5	0.61	0.68	0.75	0.12	1.00	0.63	0.42
	6	0.73	0.83	0.58	0.14	0.63	1.00	0.74
	7	0.47	0.56	0.33	0.13	0.42	0.74	1.00

Table 8: Distances in meters from cross-correlations between all the microphones at a velocity of 10 meters per second in the test section.

		Microphone						
		1	2	3	4	5	6	7
Microphone	1	0.00	3.79	4.84	49.27	116.29	0.48	0.87
	2	3.79	0.00	1.58	74.35	120.08	4.85	4.97
	3	4.84	1.58	0.00	5.95	65.67	5.61	6.28
	4	49.27	74.35	5.95	0.00	9.14	0.33	0.24
	5	116.29	120.08	65.67	9.14	0.00	4.38	4.18
	6	0.48	4.85	5.61	0.33	4.38	0.00	0.38
	7	0.87	4.97	6.28	0.24	4.18	0.38	0.00

8 Transmission Losses

The design of the new wind tunnel design requires two bends. From an aerodynamic perspective, the bends are not ideal because of pressure losses. However, their necessity can be exploited for the acoustic treatment of the wind tunnel in order to make the wind tunnel fit for aeroacoustic measurements. As mentioned and seen in the previous, the design of the corners allows them to be used as baffle mufflers. The thick corner vanes of the design allows for the housing of porous lining, which can aid in the attenuation of the motor- and fan-noise through the corners. The use of porous lining in corner vanes is, amongst others, presented in (Devenport et al. 2017) and (Bergmann 2012).

In the previous it was mentioned that the design of the corners as well as the vanes were inspired by the WindGuard anechoic wind tunnel in Germany. The motivation for the corners and vanes with a double bend with a straight section is between was for design simplicity – adding porous material inside a straight section would be placed easier than in an arch or heavily cambered airfoil-shaped vane. On top of that, an impermeable barrier is believed to not be required as air is unlikely to leak from one side of the vane to the other over a straight section.

(Soderman & Allen 2002) stated that aeroacoustic measurements will be possible when the background noise is 6 dB less than flow-induced noise by the model. From noise measurements it became evident that the sound pressure levels produced by the motor and fan combination at the maximum rotational speed is approximately 80 dB for frequencies below 2 kHz. (Munjaj 2014) mentions that an acoustically lined corner can attenuate noise for as much as 10 dB. (Munjaj 2014) states that at least a thickness of a tenth of the wavelength for the porous lining is required for it to work effectively. This already implies a difficulty in attenuating the lower frequency range of the noise.

In this section, a prediction of the transmission and insertion loss through the acoustically lined corners are made by using a finite element analysis. The effect of the complete wind tunnel configuration from the start of the fan-duct until the end of the test section will also be evaluated. In the following, the methodology and some background information regarding the used models and its inputs will be given first. Then the geometry, mesh and model set-up will be discussed. The results will be presented and discussed thereafter.

8.1 Methodology

The methodology for finding these losses is straightforward. The different parts of the tunnel have been designed earlier and these will, of course, be unchanged for the transmission loss predictions. The goal is to model the propagation of noise through each corner and calculate the attenuation. For each corner, two

cases will be presented: One where porous material is applied and one without porous material. The ratio of the attenuation between the cases, gives the insertion loss of the tunnel. The evaluations of the complete configuration will be done in a similar fashion.

The Ansys Mechanical APDL of Ansys 18.0 and the corresponding Acoustics ACT plugin were used for the simulations of noise propagation through the corners (with porous lining). After the geometries and meshes have been created, the ACT allows to set up acoustic boundary conditions and excitations as well as the option to define acoustic and material characteristics for each part of the model. Visualisations of the sound pressure levels found in the enclosed environment as well as of the transmission losses are possible with the same plugin. In this particular case, the noise propagation is found by an acoustic full harmonic analysis and without structural interaction.

In order to maintain simplicity and reduce computational effort for these evaluations, a thin model, where it is aimed to have a thickness of just one cell, will be used for the simulations. 2D simulations are not possible with the Mechanical APDL. The geometries with a thickness of one cell limits the degrees of freedom and the cell or node count of the model is kept within bounds. This almost 2D representation is identical to the 3D corner models apart from its thickness. It is assumed that results will be close to a full 3D representation as acoustic excitation and propagation are normalized to surface area. The methodology is similar to the simulations presented in (*Acoustic Simulation of a Silencer* n.d.). A 3D evaluation over a large frequency range is not possible, because it would require unavailable computational power with any of the available solvers.

8.2 Models

It is desired to do the analysis over an as wide as possible frequency-range and given that the flow resistivity, which will be discussed in more detail in later sections, is rather high for porous materials, as can be seen in (Mareze et al. 2012) and (Doutres et al. n.d.), the documentation for the Ansys Mechanical APDL implies that it would leave the JCA and Miki models as the only commonly used methods for the simulations with acoustic lining because of the ratio between frequency and flow resistivity.

In (Miki 1990) an improvement of the Delany-Bazley model is presented. The Delany-Bazley model is an empirical model that determines the characteristic impedance and the propagation coefficient of porous materials as a function of the ratio between the frequency of the noise and the flow resistivity of the porous material. Since the function by the power-law regression of the Delany-Bazley model would sometimes provide negative impedances, Miki improved the model with new regressions that would that would give only positive and

real values for the characteristic impedances. This automatically improved the performance at lower frequencies. Whereas the original Delany-Bazley model performed poorly at lower frequencies, the Miki model provides good results across the whole frequency range even though it is still bound to an upper-limit of the frequency and flow resistivity ratio of less than one. In the documentation for Ansys Mechanical APDL it is shown how the Miki model affects the impedance and propagation constant in an acoustic full harmonic analysis.

The JCA model stems from an improvement in (Champoux & Allard 1990) on the work presented in (Johnson et al. 1987). In Johnson, the acoustic behavior in porous media is described in terms of dynamic permeability and dynamic tortuosity. The model is derived from Biot's theory and attempts to solely determine the noise propagation in a porous medium by using macroscopic characteristics. The high-frequency behavior of the dynamic tortuosity is determined by the characteristic viscous length in (Champoux & Allard 1990): a parameter that is directly related to the geometry of the pores in the medium. Another parameter was determined in the same paper, the thermal characteristic length, defines the high frequency behavior of the dynamic permeability and is a result of the excess temperature caused by the compression of air inside the porous medium. The porosity, flow resistivity and tortuosity are the three remaining parameters required for the model. The JCA model is mentioned and used in multiple papers and is considered as a good method for estimating the noise propagation through porous material, even though its accuracy may diminish for lower frequencies as mentioned in Fluent Theory Guide. For a acoustic full harmonic analysis in Ansys, the JCA model alters the effective density (related to the dynamic permeability) and the effective bulk modulus (related to the dynamic tortuosity) in a full harmonic analysis in Ansys as written by the documentation for the Ansys Mechanical APDL.

In the previous subsection, the two models use a total of five parameters: flow resistivity, porosity, tortuosity, viscous characteristic length and thermal characteristic length. The first named is the only input parameters required for the Miki model. (Shravage et al. 2010b) is a study to the parameters of the JCA model, where the definition of each parameter and its effect on noise propagation is determined. The flow resistivity is the force required for the flow going through porous material. Increased flow resistivity increases transmission losses. Increased porosity also has a positive effect on transmission losses. Tortuosity is a measure of difference between the length of a straight path of a pore and the actual path of a pore. High values of tortuosity is subject to resonance effects in transmission losses throughout the frequency range as the speed of sound of the fluid is directly affected. Low values of tortuosity increase transmission losses for higher frequencies and shows itself to be the most effective. Porosity and Tortuosity often have values close to 1 for porous media. Low viscous characteristic lengths will result in higher transmission losses for mid and high frequencies. The thermal characteristic length has a minimum effect

on the transmission loss, except for very low values where it results in modified values for flow resistivity and tortuosity and will increase losses in the mid and high frequency range. In general, it becomes evident that the parameters influence the mid and high frequency range the most and this may ultimately result in poor quality of aeroacoustic measurements for low frequencies. It is therefore likely that the lower limit for the anechoic conditions for wind tunnels, besides limited lining thickness, is also a result of the inability to effectively manipulate the transmission loss for low frequencies material-wise.

8.3 Geometry

Even though a detailed design of the corner could be used for the evaluations, a simplified case is believed to suffice. This means, in addition to the duct, the lining and perforated plate/protective layer have to be added to the complete geometry of the corners. The thickness of the perforated plate should in any case be thin and was chosen to be an arbitrary 1.27 millimeter or 1/20th of an inch. This specific thickness was arbitrary. When a detailed design of the corners will be made and built in order to experimentally validate the numbers from these predictions, these thicknesses may have to be updated and the simulations may have to be run again. By leaving the geometry of duct untouched, the thicknesses of the sections with the porous material inside the vanes will become 27.46 and 57.46 millimeter thick, for the first and second corner, respectively. The length of the plate and lining sections are 300 millimeter, corresponding with the straight section of the corner vanes as can be seen in Figures 95 - 97.

In Catia V5, the geometries of the perforated plates and lining were created and assembled with their respective corners. The thickness of the whole assembled geometry was set to 1 millimeter, which would allow for a reduced cell size of the while maintaining a single-cell thickness of the mesh. The outer walls of the bend have lining-plate combinations with just one plate instead of two for the corner vane combinations. Since Ansys has a built-in model to simulate a perforated plate at the hand of several parameters, the holes did not have to be specified in the geometry. This also eases meshing at a later stage. In Figures 95 and 96 the assembly of the second corner can be seen. The first corner is, of course, assembled in a similar fashion.

For the complete geometry, the cross-section on the symmetry-plane of the duct was given a thickness of 1 millimeter. The geometries of the porous material and the perforated plates were added in the same fashion as for the separate corners. In Figure 97 the geometry of the complete configuration can be seen. For this geometry, the corners are, of course, identical to the two separate corners.

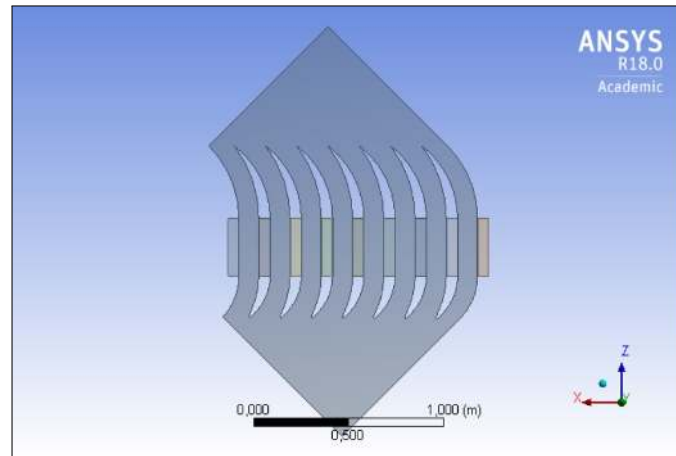


Figure 95: Simplified geometry of the second corner with perforated plate and porous material (from Ansys).

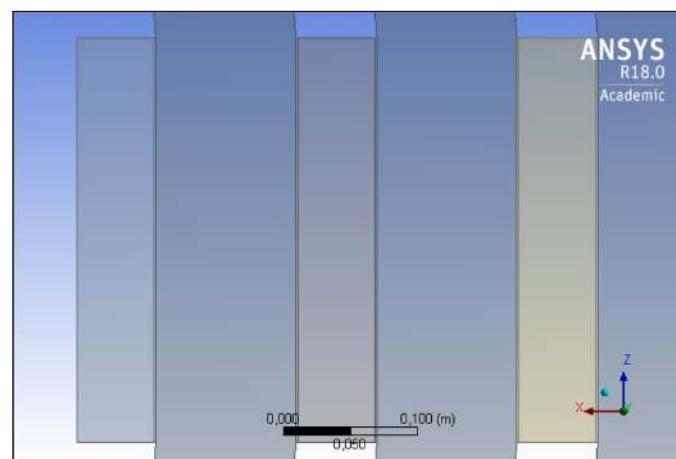


Figure 96: Close-up of the corner vane of the second corner with perforated plate and porous material (from Ansys).

8.4 Meshing and Analysis Settings

The next step was meshing the geometry. The refinement of the mesh is largely dependent on the frequency-range. For linear elements, 12 elements per wavelength are required and for quadratic elements, only 6 elements are needed. For the two corners, a multi-zone method was used with quadratic elements of a size of 2.5 millimeter. This cell-size would meet the requirements of at least 6 elements per wavelength up to a frequency of 20000 Hertz. For the convergence

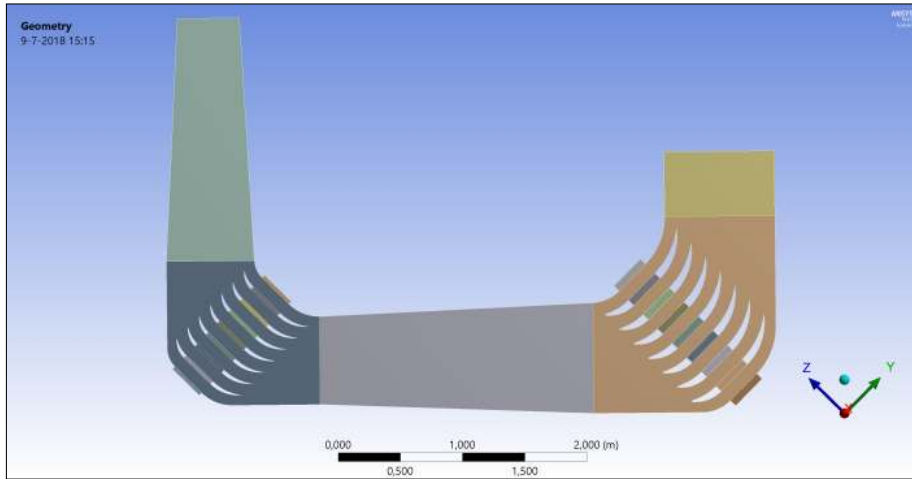


Figure 97: Simplified geometry of the complete geometry with perforated plates and porous material (from Ansys).

studies, the cell-size was reduced to 1.75 millimeters, which increased the cell-count by a factor of approximately. In order to model a perforated plate, the quadratic elements need to have exactly opposing faces and this was guaranteed by using the multi-zone method. The evaluations of the full configuration were done with cell-sizes of 7 and 5 millimeters for the standard and refined grid, respectively. The standard size would be sufficient for evaluations up to 8000 Hertz and the refined size would increase the cell-count by approximately a factor of two. Figures 98 to 105 show a part of the two corners for the 4 different meshes. An analysis up to 20000 Hertz would not be possible for the full geometry as the graphical user interface of Ansys Mechanical does not work properly on the cluster and the other available systems do not provide enough memory to generate the required mesh and input files or read the results files. Table 9 shows the number of cells in each model and case.

Table 9: Number of cells found in each geometry.

	Cell Count	
	Standard Grid	Refined Grid
Geometry 1st Corner	184105	375330
Geometry 2nd Corner	282421	576447
Complete Geometry	132493	259106

The fluid region, perforated plate and the porous material were selected as different acoustic bodies which held different acoustic properties. The fluid properties of air, found in the documentation for the Ansys Mechanical APDL, were given to all the acoustic bodies. The perforated plate was modelled by

adding a square grid model that uses a 2×2 transmittance matrix to model the holes in the body at the hand of plate thickness, hole spacing, hole radius and hole radius-ratio. (Munjal 2014) states that the acoustic properties of the porous material does not change with a porosity of 20%. This porosity of 20% was achieved with a ratio of 1 and a spacing and radius of 5 millimeter and 1.25 millimeter, respectively. (Mareze et al. 2012) provided all the relevant parameters of rock wool needed for the model to function with either the JCA or the Miki model. In this paper, rock wool has a flow resistivity of 20600 kNs/m^4 , a porosity of 0.98, tortuosity of 1.01, thermal characteristic length of $85 \mu\text{m}$ and a viscous characteristic length of $90 \mu\text{m}$. The numbers in (Mareze et al. 2012) follow the statements made in (Shravage et al. 2010b), where it is mentioned that porous media for acoustic treatment have often a porosity and tortuosity close to 1 and a high flow resistivity. For analyses without porous material applied, the acoustic bodies with the porous material and the perforated plates were simply suppressed.

An arbitrary normal surface velocity of -0.0024 m/s was chosen as the excitation for this particular solution. Radiation boundaries were given to the in- and outlet of the corner. Additional boundary conditions were the external ports given to the faces of the perforated plates adjacent to the air-line and porous material. The physical boundaries to which no boundary conditions were applied, had fully reflective walls by default. The analysis was set up to give a solution for all the center frequencies of the octave bands from 16 Hertz to 20000 Hertz for the corners and from 16 Hertz to 8000 Hertz for the complete configurations.

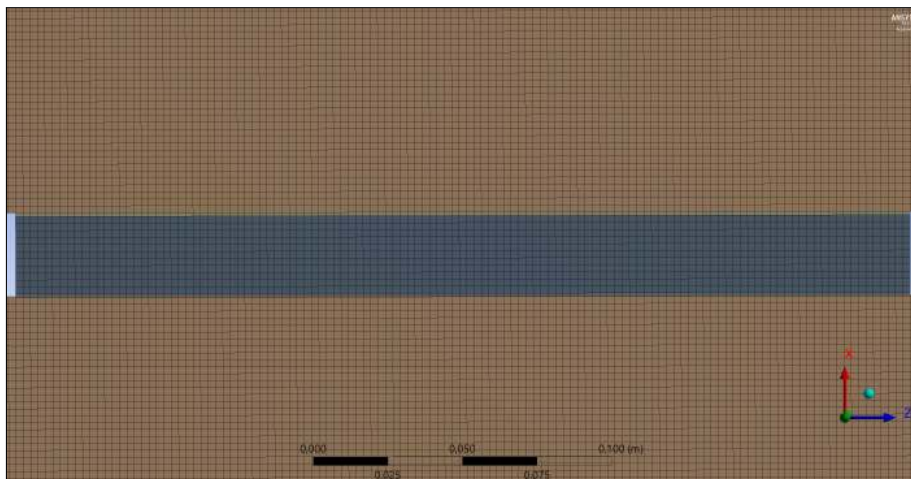


Figure 98: Mesh of the first corner, perforated plate and porous material assembly with a cell-size of 2.5 millimeter (from Ansys).

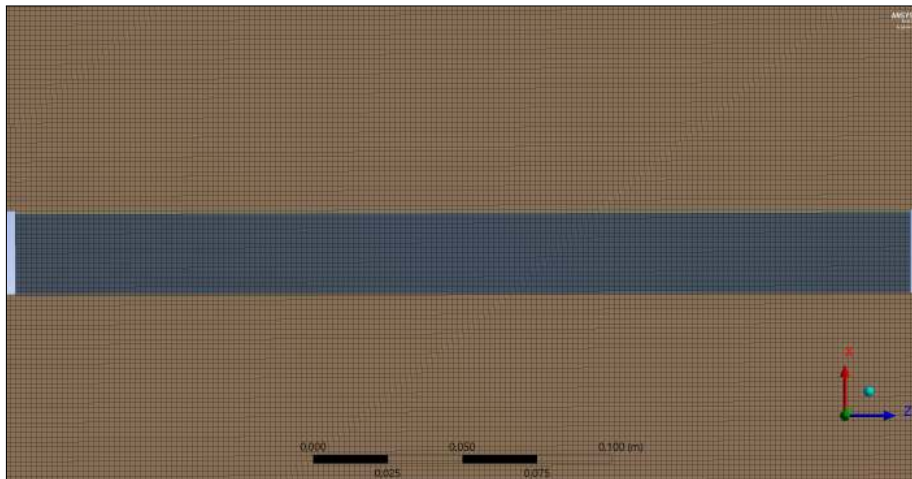


Figure 99: Mesh of the first corner, perforated plate and porous material assembly with a cell-size of 1.75 millimeter (from Ansys).

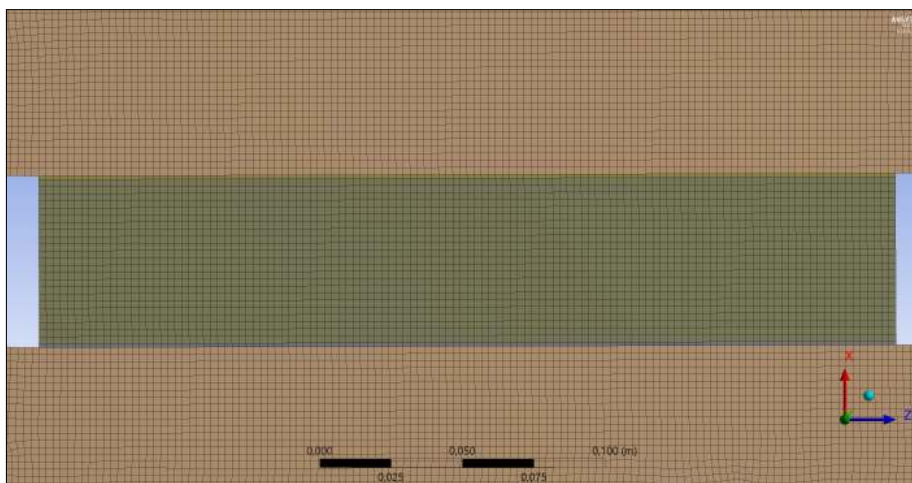


Figure 100: Mesh of the second corner, perforated plate and porous material assembly with a cell-size of 2.5 millimeter (from Ansys).

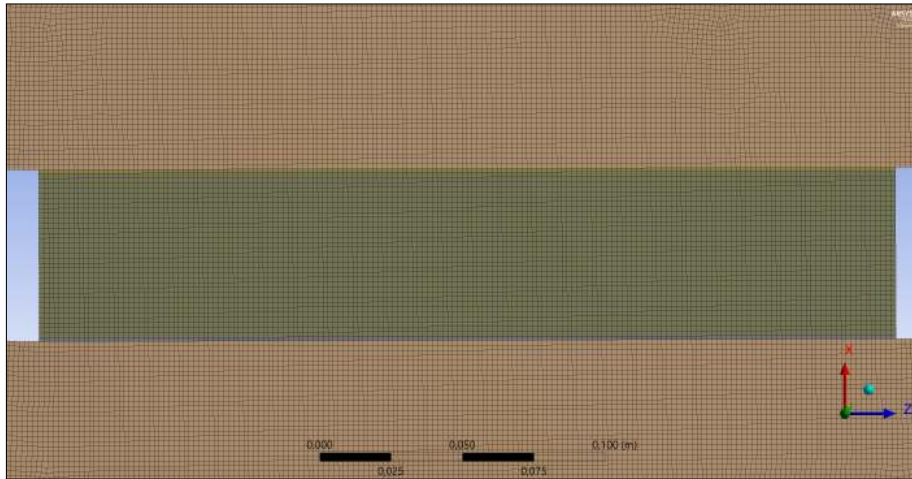


Figure 101: Mesh of the second corner, perforated plate and porous material assembly with a cell-size of 1.75 millimeter (from Ansys).

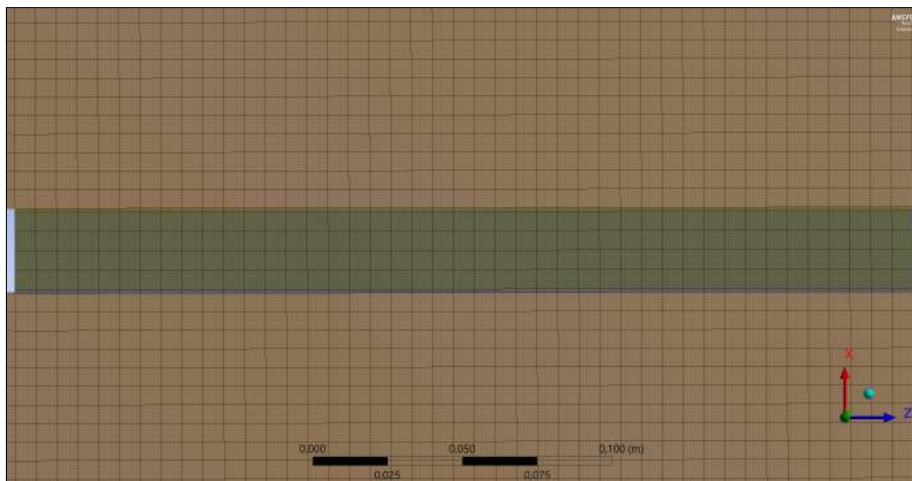


Figure 102: Mesh of the first corner, perforated plate and porous material assembly as in the complete geometry with a cell-size of 7 millimeter (from Ansys).

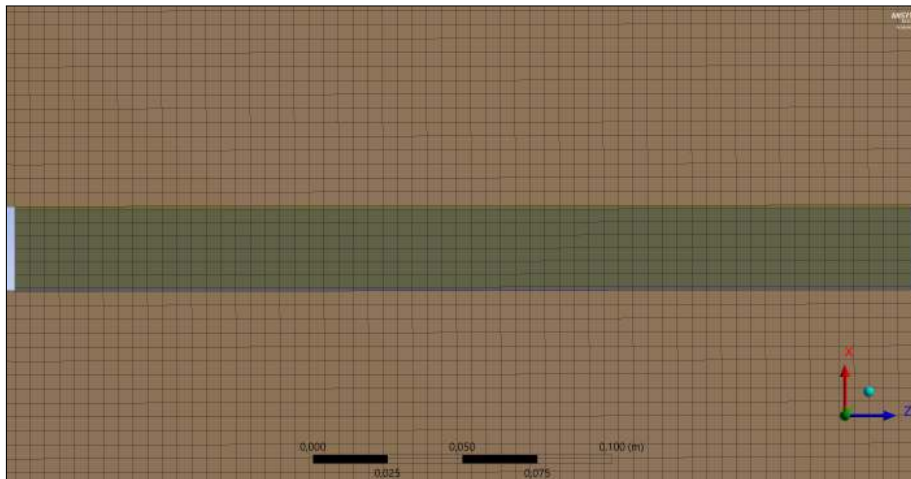


Figure 103: Mesh of the first corner, perforated plate and porous material assembly as in the complete geometry with a cell-size of 5 millimeter (from Ansys).

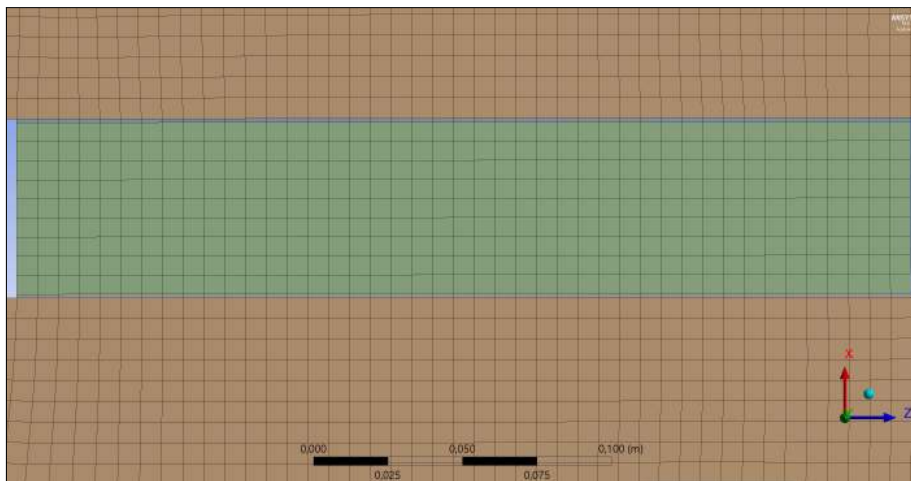


Figure 104: Mesh of the second corner, perforated plate and porous material assembly as in the complete geometry with a cell-size of 7 millimeter (from Ansys).

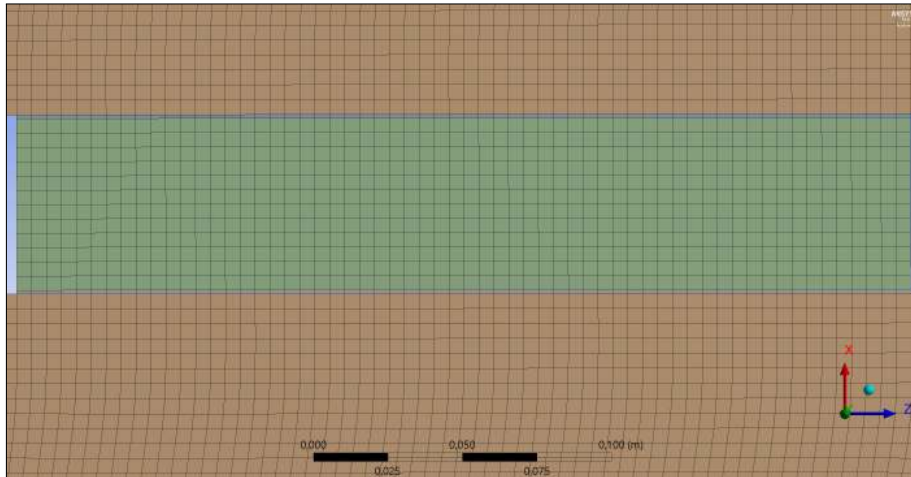


Figure 105: Mesh of the second corner, perforated plate and porous material assembly as in the complete geometry with a cell-size of 5 millimeter (from Ansys).

8.5 Results

The transmission losses through each corner with and without porous material can be seen in Figure 106. The results with a refined grid can also be seen here. In Figure 107 a similar Plot can be seen for the complete configuration. Figure 108 shows the noise reduction per corner, of the corners added together and the complete configuration, where the transmission loss without porous material is deducted from the transmission loss with porous material. Figures 109 to 114 show the contour Plots of the corners for the two different models that were and without porous material applied from the simulations with the standard mesh. Figures 115 to 117 show the same Plots for the complete configuration. Table 10 shows the average transmission losses through each corner with and without porous material. Table 12 shows the average transmission losses for the complete configuration. Table 11 shows the percentual difference between the outcomes of the standard and their respective refined grids of the corners. Table 13 shows the percentual differences between the outcomes of the convergence study for the complete configuration.

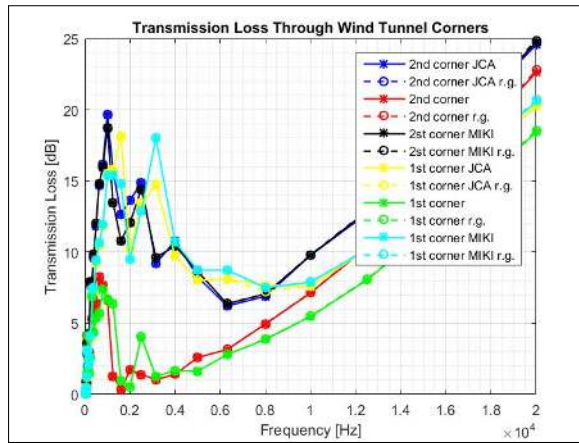


Figure 106: Transmission losses through the corners (from MatLab).

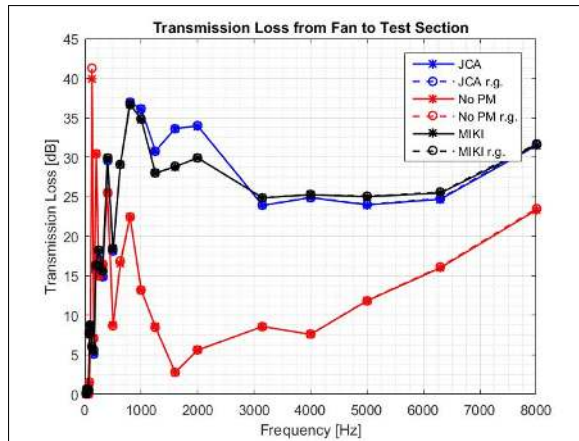


Figure 107: Transmission losses from fan to test section (from MatLab).

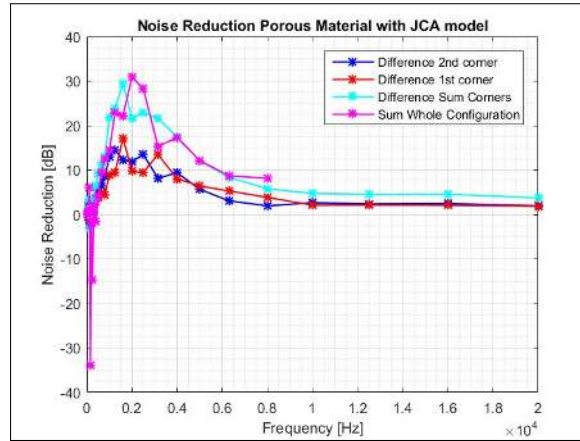


Figure 108: Noise reduction by applying porous material for the two corners and complete configuration (from MatLab).

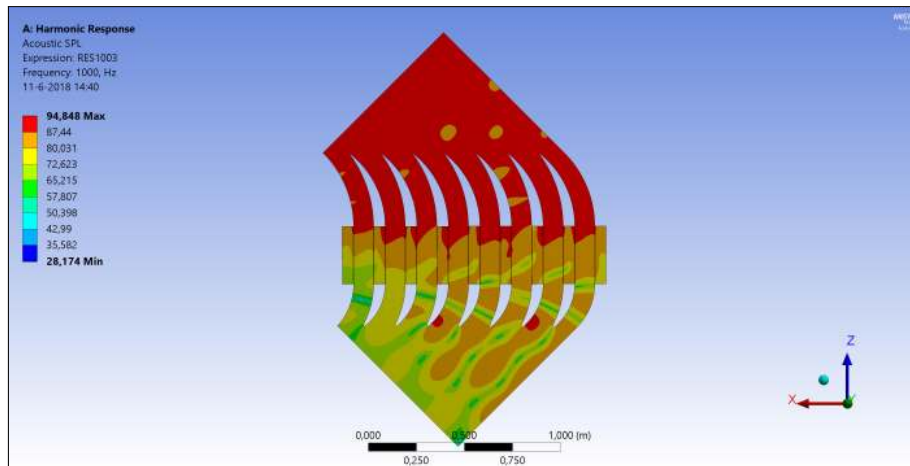


Figure 109: Contour plot of transmission losses through the second corner with the JCA model (from Ansys).

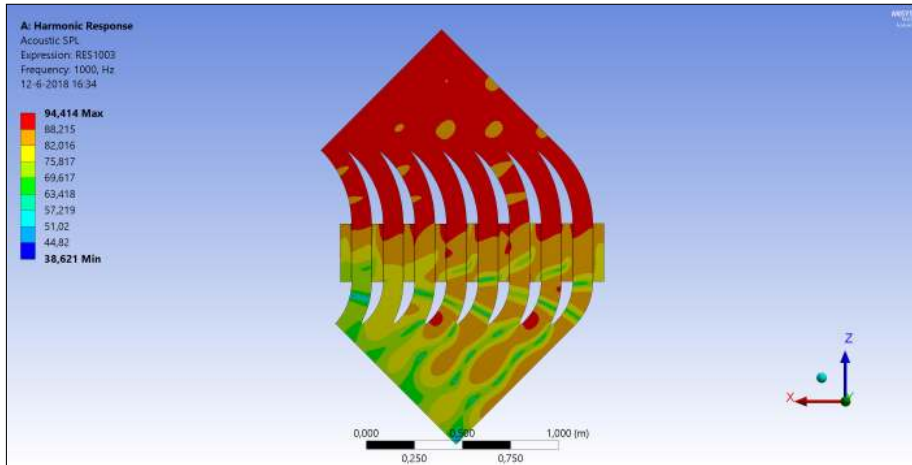


Figure 110: Contour plot of transmission losses through the second corner with the Miki model (from Ansys).

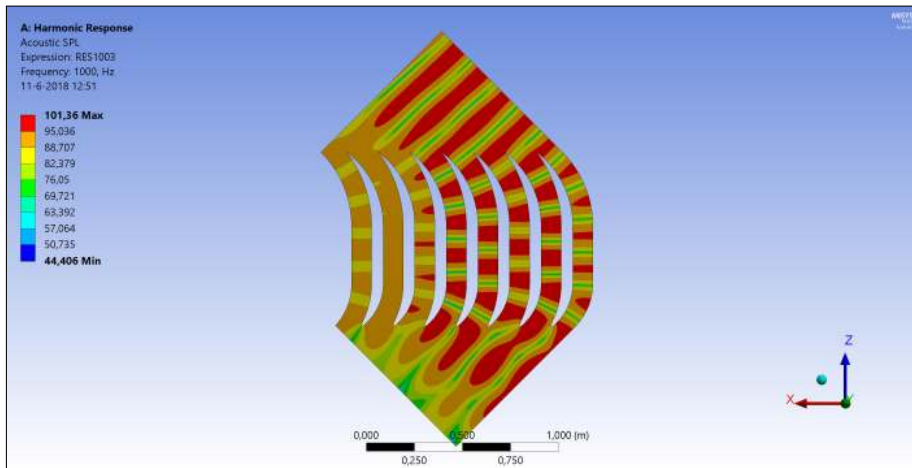


Figure 111: Contour plot of transmission losses through the second corner with no porous lining (from Ansys).

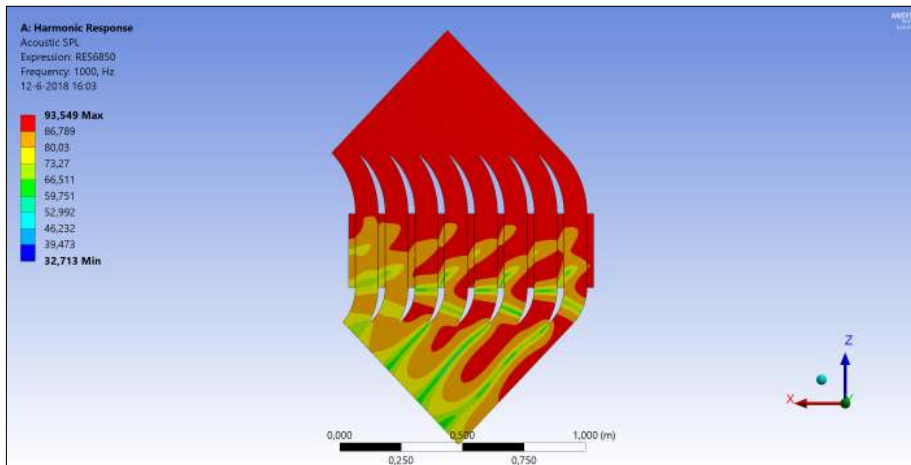


Figure 112: Contour plot of transmission losses through the first corner with the JCA model (from Ansys).

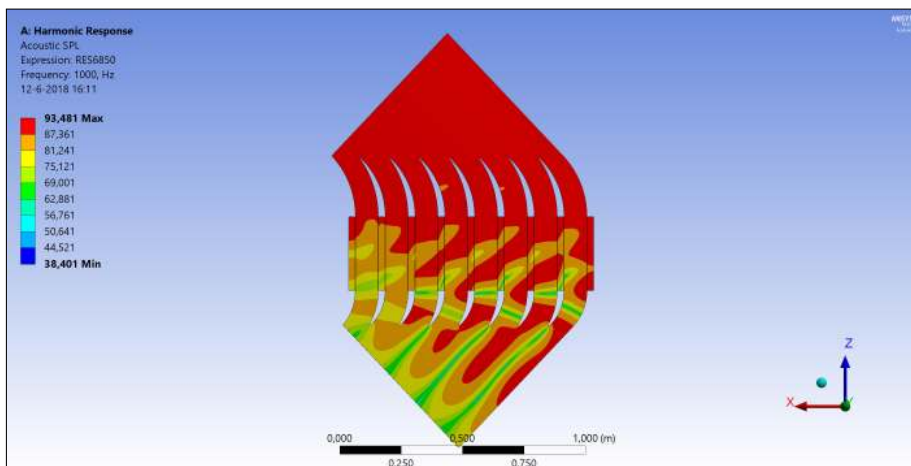


Figure 113: Contour plot of transmission losses through the first corner with the Miki model (from Ansys).

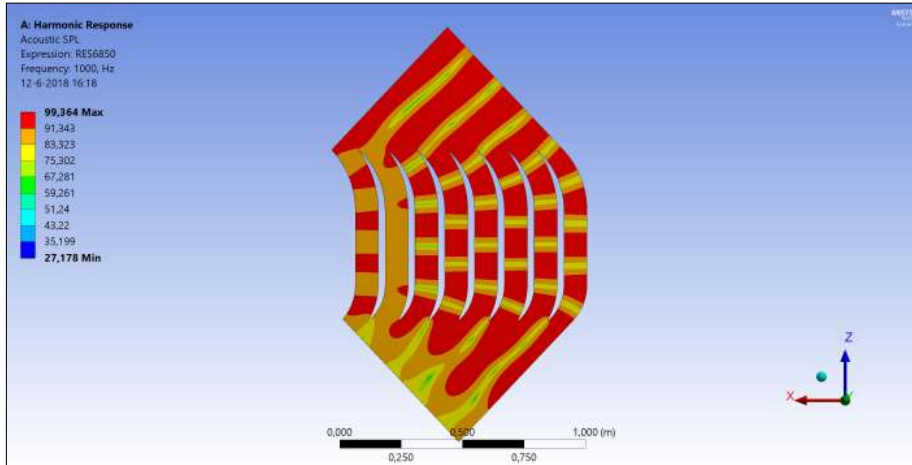


Figure 114: Contour plot of transmission losses through the first corner with no porous lining (from Ansys).

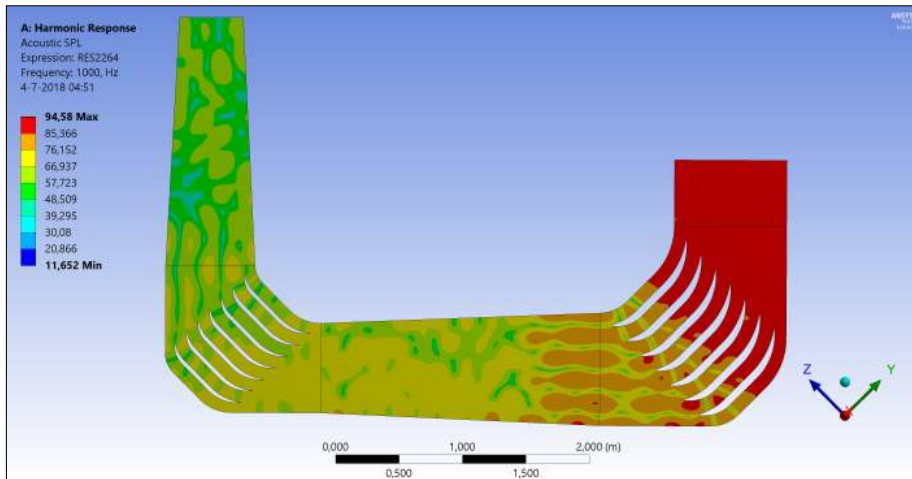


Figure 115: Contour plot of transmission losses from fan to test section with the JCA model (from Ansys).

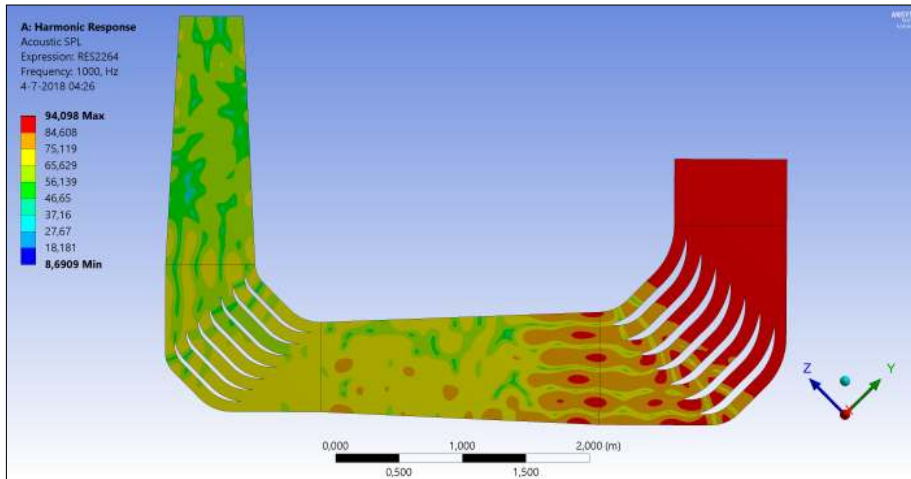


Figure 116: Contour plot of transmission losses from fan to test section with the Miki model (from Ansys).

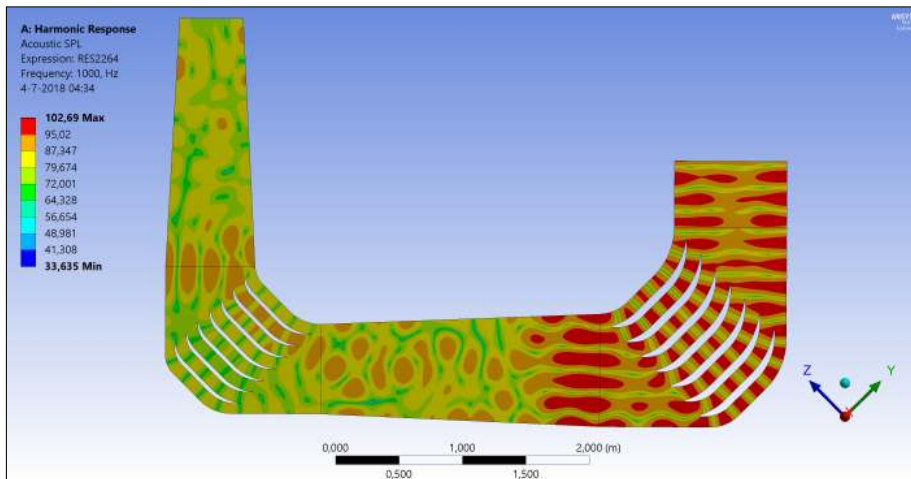


Figure 117: Contour plot of transmission losses from fan to the test section with no porous lining (from Ansys).

Table 10: Average transmission losses for the corners.

	Average Transmission Loss [dB]	
	Standard Grid	Refined Grid
1st Corner JCA	12.6361	12.6484
1st Corner Miki	12.9110	12.9633
1st Corner	8.6176	8.6726
2nd Corner JCA	14.489	14.5428
2nd Corner Miki	14.5074	14.5608
2nd Corner	10.5222	10.5768

Table 11: Results of grid-convergence study for the corners.

	Difference [%]
1st Corner JCA	0.0966
1st Corner Miki	0.6339
1st Corner	0.4037
2nd Corner JCA	0.3673
2nd Corner Miki	0.5166
2nd Corner	0.3667

Table 12: Average transmission losses for the complete configuration.

	Average Transmission Loss [dB]	
	Standard Grid	Refined Grid
JCA	27.3044	27.3706
MIKI	27.0434	27.1121
No Porous Material	13.8539	13.9184

Table 13: Results of grid-convergence study for the complete configuration.

	Difference [%]
JCA	0.2416
MIKI	0.2535
No Porous Material	0.4634

8.6 Discussion of Transmission Loss Results

From Figures 106 and 107 it can be seen that the corners with porous material are particularly effective for the mid-range frequencies between 1 kHz and 4 kHz. Figure 108 shows that the low frequencies are difficult to control and that the effect of the porous material diminishes for higher frequencies, even though the transmission loss is steadily going up in this range. The lower performance for the lower frequencies is explained in a parametric study by (Shravage et al. 2010b) and the book by (Munjal 2014), where in the former it is implied that the parameters of porous material have hardly any effect on the lower frequencies and in the latter it is stated that porous material is effective with a module-thickness of at least a 10th of the wavelength. The absorptive material is relatively thin compared to the long wavelengths of low frequency noise. For the high frequency range, it can be observed that even without porous material the transmission loss is high. In (Munjal 2014), there is also an estimate of 10 dB is given as an achievable transmission loss for a corner or baffle muffler. This 10 dB corresponds with the order of the numbers found by the simulations. The simulations of the noise propagation from the fan to the end of the test section showed that the transmission loss were only slightly higher than the losses found by adding up the transmission losses of the two separate corners and indicate that the diffusers and straight ducts only have a minor effect in attenuating the noise. In Figures 109 to 117, the contour plots show very well the plane waves through the corners where no porous lining is used. For the corners where porous material is applied, the attenuation of noise can clearly be observed. In these contour Plots, the differences between the JCA and Miki model can hardly be seen. The refined grid shows no drastic changes in results. The Miki model was used as a verification method for the JCA model as the two models are drastically different. Even though there are some noticeable differences of only a couple percent between the outcomes, the results are of the same order and follow the same trend.

In the previous, it was mentioned that aeroacoustic measurements are viable if the noise of the test subject is exceeds the background noise by 6 dB. In Figure 118 the transmission loss of both corners is deducted from the 1/3 octave band spectrum of the noise captured by the first microphone at a flow velocity of 40 meters per second in the previous section. The deduction of the transmission loss found for the complete configuration is also shown in the same figure. It can be seen that the first real difference with applying porous material in the corner vanes is observable at 200 Hertz and becomes significant after 500 Hertz. In the mid and high frequency range thereafter, the effect of the lining can be seen to be as much as 20 dB and the deductions leave sound pressure levels to lie between 40 and 50 dB up to the band with a center frequency of 8000 Hertz. The complete geometry generally performs better than the two separate corners in the mid and high frequency range. This difference may be the results of the incorporation of the straight ducts and diffusers for the analysis. The effect can be observed for both the cases with and without porous material applied. By

looking at (Brooks et al. 1989), the noise spectrum of different kind of airfoils is still found to lie around 50 dB. The same can be seen in (Arbey & Bataille 1983) for measurements at flow velocities of 35 meters per second. This, plus the fact that the lower frequencies are unattenuated, imply that the lined corner vanes may not be enough to guarantee an adequate environment for aeroacoustic measurements.

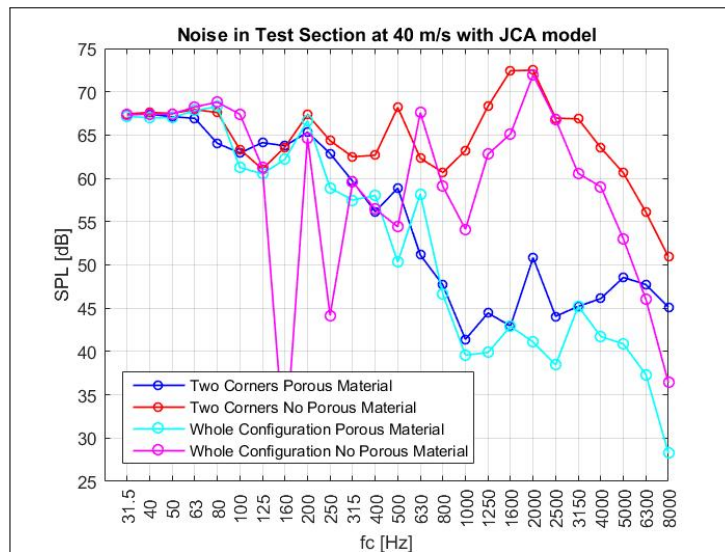


Figure 118: The transmission losses found in the two corners deducted from the noise measurements made with the first microphone at a flow velocity of 40 meters per second (from MatLab).

Validation is key and required to find out whether the 2D simulations of the corners give a good representation of the 3D problem. By constructing one of the corners and experimentally find the transmission loss in a setup that is similar to how the simulations setup, the value of this, in fact, prediction method can be shown. Another validation in a full wind tunnel setup, where the noise source would be a real fan, can show whether the simplification by using a normal velocity excitation is sufficient. In (Shravage et al. 2010a) and (Doutres et al. n.d.) methods are presented to find the acoustic properties of the material for when they are not known beforehand. This would mean that after the validation-process, simulations may need to be run again with altered parameters. The prediction of the noise that could be expected inside the test section may have been lacking in the sense that not the complete transmission loss of one octave-band has been calculated. Instead determining the octave-band from a range of frequencies with an identical resolution as the measurements (25 Hertz), simulations were run for just the center frequencies. This could be

a problematic simplification. However, doing simulations for frequencies up to 12800 or 20000 Hertz with a better frequency resolution results in large input-files, the need for loads of RAM and access to a lot of free disk-space (on the order of tens of terabytes). What can be concluded so far, is that the acoustic lining is not sufficient to allow for proper aeroacoustic measurements.

9 General Conclusion and Discussion

The first steps in designing a new aeroacoustic wind tunnel could be made in this study. From the literature study it could be concluded that there are straightforward and proven methods to design a wind tunnel. The design of aeroacoustic wind tunnels largely follow the same principles as regular wind tunnels do. Even though there is noise as an additional aspect that has to be taken into account in the design of such a wind tunnel, the focus should still be on the aerodynamics and the flow quality. The reason for this is, is that a clear understanding of the physics behind the noise is needed and a controllable environment is desired and bad flow quality may generate noise elsewhere in the tunnel. Rather than addressing noise sources inside the wind tunnel individually that may stand in the way of a proper anechoic environment for aeroacoustic measurements in the test section, simple and effective solutions such as (baffle) mufflers are recommended.

A design of the wind tunnel was made by following recommendations in literature. The corners however, were made with the philosophy that they would eventually be used as baffle-mufflers to attenuate noise. A trial-and-error process was done to find corner and thick corner vane geometries that would give good aerodynamic results in 2D simulations of the new wind tunnel design. The corner vanes were given a thickness beforehand for the placement of porous material later on. The 2D simulations gave good results for the current wind tunnel design. The methodology and the set up of these simulations however, did not exactly follow the Fluent User's Guide recommendations and may not have been ideal. The default inlet turbulence intensity was set at its default value of 5% as a boundary condition, whilst lower turbulence intensities could be expected in a true indoor environment with stationary air. Then the inflation-layer may not have been fine enough for some of the simulations where wall treatment was used. The convergence study may have been insufficient as well and even though the cases where the boundary layer was completely resolved showed favorable characteristics, an additional convergence study with an additional refinement may have shown different results.

The 2D solutions were considered good enough and 3D evaluations were done next. The 3D simulations followed much closer the Fluent recommendations and used a more robust solver that is available in Fluent. The quality inside the test section appeared to be good after the 3D simulations. The outcomes of the CFD simulations were also close to those from empirical predictions. It turned out that the new design has a better performance compared to the old red wind tunnel. Even though favorable characteristics were found inside the test section, mostly the first diffuser was giving problems. Separation was seen here and resulted in non-ideal flow characteristics in the first corner and second diffuser downstream. It was argued however, that this separation is incorrectly predicted by the model that was employed because of Boussinesq's assumption

of proportional production of turbulence kinetic energy to the strain rate. This separation, also predicted a large sound power level generated by the air. Its significance is somewhat unknown as it is not clear what amount or what volume of air produces these high levels of noise. At the same time, nothing is known about the propagation of the noise. It does occur close to the test section and may spoil aeroacoustic measurements. A reevaluation is needed where either the Kato-Launder limiter in order to limit the over-production of turbulence that is characteristic of the SST $k - \omega$ model and/or another model will be used, before a redesign of the first diffuser should be considered. The boundary layer noise on the other hand, was limited and only visible in regions with high velocity such as the contraction-exit and the leading-edges of the corner vanes. Also here it is not clear what the significance of the sources are for the receiver. However, it becomes clear what the benefit is from the long contraction-types with very moderate curvature designed by methods presented by (J. H. Downie 1984), for example, as the velocity extrema at the walls are low. The area of the noise sources of the leading-edges of the corner vanes is very small and the corner vanes themselves are a considerable distance away from the test section, making the boundary layer noise of less importance.

The noise measurements of the fan of the red wind tunnel showed that the noise of the fan was highest between 1000 and 2000 Hertz. The tonal noise was also visible as strong peaks in the spectra. The propagation of noise stemming from the fan in the basement to the ground floor did not become visible after using the (cross-)correlation of the time and frequency signal.

The transmission loss of the corners and the part of the wind tunnel going from the fan-inlet to the exit of the test section found in the simulations gave consistent results with refined grids and the use of different models. It remains unclear however if these numbers translate to real-life situations because of the 2D simplification. A validation is therefore required. The 2D simplification, the use of a plane-wave as a noise source and the assumption of fully reflective boundaries may have given unrealistic results. The prediction of the noise that could be expected inside the test section may have been lacking in the sense that not the complete transmission loss of one octave-band has been calculated. Instead determining the octave-band from a range of frequencies with an identical resolution as the measurements (25 Hertz), simulations were run for just the center frequencies. This could be problematic simplification as the behaviour for other frequencies in that band is unknown. However, doing simulations for frequencies up to 12800 or 20000 Hertz with instances of 25 Hertz requires large input-files, loads of RAM and a lot of free disk-space (on the order of tens of terabytes). An extensive study into the transmission loss by doing simulations requires, all in all, a lot of resources and is therefore in most cases a limiting factor. What is hinted in the noise measurements and transmission loss predictions so far, is that the acoustic lining may not be sufficient for proper aeroacoustic measurements.

The HPC services of DTU were used for the CFD and FEA simulations. For this, input files had to be created, which proved to be rather difficult at times as the Ansys geometrical, meshing and Fluent interfaces, did not work properly on the server computers. Hence, a personal computer had to be used to create input files. This was time-consuming with limited RAM and processing power. On top of that, the post-processing was also difficult on the HPC computers. Post-processing exported solution files on a personal computer was necessary and had a risk of crashing Ansys or the computer, because of the size of the exported solution files. This limited, amongst others, the amount and quality of figures and log files that could be extracted and presented in the report.

10 Recommendations

While the initial steps have been made for the design of a new wind tunnel, there is still room for improvement and there are additional steps to be taken. In continuation of this project, it is recommended that the 3D CFD simulations are done with another turbulence model or that a Kato-Lauder limiter is used with the current one. A redesign of the first diffuser may be needed depending on the results. For any new simulation, whether it is CFD or FEA, it is recommended to work on a computer with strong performance in order to ease pre- and post-processing.

Extra analyses with a higher frequency resolution could aid in better predictions of transmission losses. As was mentioned earlier, the effect of the corners is then easier to compare and to interpreted with noise measurements as it allows for a sounder picture of the losses in octave bands. The noise simulations need to be validated, however, in order to see whether the 2D simplification holds for real-life situations. This could possibly be done by placing a mock-up of the corners in an anechoic chamber. On the upstream side of the model, there is a microphone placed. On the downstream side of the corner a noise source that either emits a certain tone or white noise is placed. The transmission loss could then be found by subtracted the microphone readings from the pressure levels of the emitted noise.

Since the screens, inlet-filter, inlet-muffler, exit-diffuser and the square to circular transition have not been treated so far, these should also be investigated. Especially the cross-sectional transition may be important to model for CFD and evaluate before building as it will also determine the inflow conditions of the fan. Turbulence intensities in the test section appeared to be a bit high, but could be addressed together with the placement of screens and determining the wind tunnel characteristics in testing.

Parametric studies by using different porous linings and porosities of the perforated plates during propagation simulations, may give new insights or give better results in calculating transmission losses. Additionally, new evaluations with filling up the arcs of the corner vane's trailing-edges with porous material could be done in order to see whether it has a positive effect on the anechoic environment in the test section of the current wind tunnel configuration. The inclusion of the fan-duct in this analysis, where the fan-hub and walls are lined with porous material, is also recommended. The single plane-wave, could be replaced with two sources on planes on either side of the hub here if there are no better alternatives to model the noise sources for such an analysis.

Then, to have a better understanding of the fan as a noise source and to make an attempt to make it quieter in operation, noise measurements upstream of the fan inside the wind tunnel could be done by using a microphone array. (virtual)

noise sources on the fan could then be identified and possibly be eliminated in a similar fashion as described in (Remillieux et al. 1986). For such measurements, it is also recommended to use a higher sampling frequency in order to find the power spectral density at higher frequencies - In the literature study earlier, it was already mentioned that scaled models will emit noise of higher frequencies. During calibration for aeroacoustic measurements in the tunnel, it may be useful to have knowledge of the noise characteristics of the fan in this range.

Finally, detailed designs and engineering drawings of the new wind tunnel are required for construction and it might be of interest to find the pressures and forces on the wind tunnel walls during operation from the CFD results before that as it can be a help in selecting materials.

Additional things that might be of interest are, if the computational resources are available, modelling the propagation from the fan to the test section and the adjacent anechoic chamber. Similarly, the new design placed in the environment with two floors could be modelled in order to see how the noise propagates through the wind tunnel and elephant hole.

More in-depth noise analyses from the flow are difficult and unnecessary. Even though Fluent provides a direct method and an integral method based on acoustic analogy, which both use an unsteady/transient solution, they are of limited use in this situation according to the Fluent User's Guide. The integral method only calculates far-field noise to the free-stream. It is impossible to find the propagation in wall-bounded flows here. The direct method is limited to near-field noise, requires a lot of computational resources and non-reflective boundary conditions. What is possible, however, is a study to structural vibration and Helmholtz resonance. From a transient solution, the pressure fluctuations on surfaces and walls can be extracted and imported in Ansys Mechanical. These fluctuations can be implemented as excitations. The propagation of noise produced by these excitations can then be modeled.

11 Bibliography

- Abbaspour, M. & Shojaee, M. N. (2009), ‘Innovative approach to design a new national low speed wind tunnel’.
- Acoustic Simulation of a Silencer* (n.d.).
URL: <https://www.simutechgroup.com/tips-and-tricks/fea-articles/379-acoustic-simulation-of-a-silencer>
- Allen, C. S. & Olsen, L. E. (1998), ‘Effect of free stream turbulence on the flow-induced background noise of in-flow microphones’.
- Allen, C. S. & Soderman, P. T. (1993), ‘Aeroacoustic probe design for microphone to reduce flow-induced self-noise’.
- Amiet, R. K. (1975), ‘Correction of open jet wind tunnel measurements for shear layer refraction’.
- Anderson, J. D. (2008), *Introduction to Flight*.
- Arbey, H. & Bataille, J. (1983), ‘Noise generated by airfoil profiles placed in a uniform laminar flow’.
- Batchelor, G. K. (1953), *The Theory of Homogeneous Turbulence*.
- Bauer, A. B. (1976), ‘Acoustically transparent walls for wind-tunnel applications’.
- Bell, J. H. & Mehta, R. D. (1988a), ‘Contraction design for small low-speed wind tunnels’.
- Bell, J. H. & Mehta, R. D. (1988b), ‘Design and calibration of the mixing layer and wind tunnel’.
- Bergmann, A. (2012), ‘The aeroacoustic wind tunnel dnw-nwb’.
- Boes, S., Nüesch, S. & Stillman, S. (2013), ‘Aircraft noise, health and residential sorting: Evidence from two quasi-experiments’, *Health Economics* **22**, 1037–1051.
- Bradshaw, P. & Pankhurst, R. C. (1964), ‘The design of low-speed wind tunnels’, *NPL Aero REport*.
- Brooks, T. F., Pope, D. S. & Marcolini, M. A. (1989), ‘Airfoil self-noise and prediction’.
- Brouwer, H. H. (1997), ‘Anechoic wind tunnels’.
- Calautit, J. K., Chaudhry, A. N., Hughes, B. R. & Sim, L. F. (2014), ‘A validated design methodology for a closed-loop subsonic wind tunnel’.

- Champoux, Y. & Allard, J. F. (1990), 'Dynamic tortuosity and bulk modulus in air-saturated porous media'.
- Devenport, W., Bak, C., Brown, K., Borgoltz, A., Oesterlund, J. & Davidsson, P. (2017), 'Design and operation of hybrid aeroacoustic wind tunnels'.
- Donald A. Dietrich, M. F. H. & Abbott, J. M. (1977), 'Fan acoustic signatures in an anechoic wind tunnel'.
- Doutres, O., Salissou, Y., Atalla, N. & Panneton, R. (n.d.), 'Evaluation of the acoustic and non-acoustic properties of sound absorbing materials using a three-microphone impedance tube'.
- Duell, E., Yen, J., Walter, J. & Arnette, S. (2004), 'Boundary layer noise in aeroacoustic wind tunnels'.
- Eckert, W. T., Mort, K. W. & Jope, J. (1976), 'Aerodynamic design guidelines and computer program for estimation of subsonic wind tunnel performance'.
- Fowler, P. M. (n.d.), 'Practical classical methods'.
URL: <http://www.us.binghamton.edu/fowler/>
- Glegg, S. & Devenport, W. (2017), *Aeroacoustics of Low Mach Number Flows*.
- Grissom, D. L., Smith, B., Devenport, W. J. & Stewart, G. A. L. (2006), 'Rough-wall boundary layer noise'.
- H. Arbey, J. B. (1983), 'Noise generated by airfoil profiles placed in a uniform laminar flow', *J. Fluid Mech* **134**, 33–47.
- Hernandez, M. A. G., Lopez, A. I. M., Jarzabek, A. A., Perales, J. M. P., Wu, Y. & Xiaoxiao, S. (2013), 'Design methodology for a quick and low-cost wind tunnel'.
- Hersh, A. S., Soderman, P. T. & Hayden, R. E. (1974), 'Investigation of acoustic effects of leading edge serrations on airfoils'.
- Ito, T., Ura, H. & Yokokawa, Y. (2008), 'Aeroacoustic noise measurements in aerodynamic low-speed wind tunnels'.
- J. H. Downie, R. Jordinson, F. B. (1984), 'On the design of three-dimensional wind tunnel contractions'.
- Jacob, M. C. & Talotte, C. (2000), 'Numerical prediction methods for the assessment of aerodynamic sound generation on high speed trains'.
- Jaeger, S. M., Horne, W. C. & Allen, C. S. (2000), 'Effect of surface treatment on array microphone self-noise'.
- Janssen, S. A., Vos, H., Eisses, A. R. & Pedersen, E. (2010), 'Predicting annoyance by wind turbine noise'.

- Jewel B. Barlow, William H. Rae Jr., A. P. (1999), *Low-Speed Wind Tunnel Testing*, John Wiley Sons Inc.
- Johansson, A. V. (1992), ‘Low speed wind-tunnel with extreme flow quality - design and tests’.
- Johnson, D. L., Koplik, J. & Dashen, R. (1987), ‘Theory of dynamic permeability and tortuosity in fluid-saturated porous media’.
- Kaltenbach, M., Maschke, C., Hess, F., Niemann, H. & Fuehr, M. (2013), ‘Health impairments, annoyance and learning disorders by aircraft noise’, *International Journal of Environmental Protection* **6**, 15–46.
- Kolb, A., and Roger Drobietz, P. F. & Graenewald, M. (2007), ‘Aeroacoustic wind measurements on a 2d high-lift configuration’.
- Kulkarni, V., Sahoo, N. & Chavan, S. D. (2010), ‘Simulation of honeycomb-screen combinations for turbulence management in a subsonic wind tunnel’.
- L.D. Santana, M. Carmo, F. C. (2014), ‘The update of an aerodynamic wind-tunnel for aeroacoustic testing’, *J. Aerospace Technology Management* **6**(2), 111–118.
- Leclercq, D., Doolan, C. & Reichl, J. (2007), ‘Development and validation of a small-scale anechoic wind tunnel’.
- Leifsson, L., Koziel, S., Andrason, F., Magnusson, K. & Gylfason, A. (2012), ‘Numerical optimization and experimental validation of a low-speed wind tunnel contraction’.
- Lindgren, B., Oesterlund, J. & Johansson, A. V. (1998), ‘Measurement and calculation of guide vane performance in expanding bends for wind tunnels’.
- Loerke, R. I. & Nagib, H. M. (1976), ‘Control of free-stream turbulence by means of honeycombs: A balance between suppression and generation’.
- Lopes, L. V., Brentner, K. S., Morris, P. J. & Lockard, D. P. (2006), ‘Increased fidelity in prediction methods for landing gear noise’.
- Lv, J., Wang, N., Liao, D., Yu, Y. & Gao, X. (2018), ‘Study on acoustically transparent test section of aeroacoustic wind tunnel’.
- Mareze, P. H., Lenzi, A. & Pellegrini, C. (2012), ‘Rigid-frame porous material acoustic attenuation on compressor discharge’.
- Mathew, J., Bahr, C. J., Sheplak, M. & Cattafesta, L. (2005), ‘Design, fabrication and characterization of an anechoic wind tunnel facility’.
- Mathworks (n.d.), ‘Welch’s method’.
URL: <https://www.mathworks.com/examples/signal/mw/signal-ex45136368-welch-s-method>

- Mehta, R. D. & Bredshaw, P. (1979), 'Design rules for small low speed wind tunnels', *The Aeronautical Journal of the Royal Aeronautical Society*.
- Mehta, R. D. & Hoffmann, P. H. (1986), 'A study of the factors affecting boundary layer two-dimensionality in wind tunnels'.
- Menter, F. R. (1994), 'Two-equation eddy-viscosity turbulence models for engineering applications', *AIAA Journal*. **32**(8).
- Migliore, P. & Oerlemans, S. (2003), 'Wind tunnel aeroacoustic tests of six airfoils for use on small wind turbines'.
- Miki, Y. (1990), 'Acoustical properties of porous materials - modifications of delany-bazley models'.
- Morel, T. (1975), 'The comprehensive design of axisymmetric wind tunnel contractions'.
- Munjaj, M. (2014), *Acoustics of Ducts and Mufflers*, John Wiley and Sons Ltd.
- Pascioni, K., Reger, R., Edstrand, A. & Cattafesta, L. (2014), 'Characterization of an aeroacoustic wind tunnel facility'.
- Patterson, G. N. (1938), 'Modern diffuser design'.
- Piccin, O. (2009), 'Cepra19: The onera large anechoic facility'.
- Remillieux, M. C., Crede, E. D., Camargo, H. E., Burdisso, R. A. & Devenport, W. J. (1986), 'The virginia tech stability wind tunnel from an aerodynamic into an aeroacoustic facility'.
- Remillieux, M. C., Crede, E. D., Camargo, H. E., Burdisso, R. A., Devenport, W. J., Rasnick, M., Seeters, P. V. & Chou, A. (2008), 'Calibration and demonstration of the new virginia tech anechoic wind tunnel'.
- Ross, R., Young, K. J., Allen, R. M. & van Ditschuijzen, J. C. A. (1983), 'Acoustic wave propagation through the shear layer of the dnw large open jet wind tunnel'.
- Sahlin, A. & Johansson, A. V. (1991), 'Design of guide vanes for minimizing the pressure loss in sharp bends'.
- Santana, L. D., Carno, M. & Catalano, F. M. (2014), 'The update of an aerodynamic wind tunnel for aeroacoustic testing'.
- Scheiman, J. & Brooks, J. D. (1980), 'Comparison of experimental and theoretical turbulence reduction from screens, honeycomb, and honeycomb-screen combinations'.
- Selig, M. S., Deters, R. W. & Williamson, G. A. (2011), 'Wind tunnel testing airfoils at low reynolds numbers'.

- Shrivage, P., Jain, S. & Karanth, N. (2010*a*), 'A comparison of analytical and optimization inverse techniques for characterizing intrinsic parameters of porous materials'.
- Shrivage, P., Jain, S. & Karanth, N. (2010*b*), 'Effect of intrinsic parameters on sound absorption and transmission loss - a parametric study'.
- Sijtsma, P., Oerlemans, S., Tibbe, T. G., Berkefeld, T. & Spehr, C. (2014), 'Spectral broadening by shear layers of open jet wind tunnels'.
- Soderman, P. T. & Allen, C. S. (2002), 'Microphone measurements in and out of airstream'.
- Soderman, P. T., Jaeger, S. M., Hayes, J. A. & Allen, C. (2000), 'Acoustic performance of the 40- by 80-foot wind tunnel test section deep acoustic lining'.
- Su, Y.-X. (1991), 'Flow analysis and design of three-dimensional wind tunnel contractions'.
- Sumer, B. M. (2003), 'Lecture notes on turbulence'.
- Thomas F. Brooks, D. S. P. & Marcolini, M. A. (1989), 'Airfoil self-noise and prediction', *NASA Reference Publication* (1218).
- Wagner, Bareiss, G. (1996), *Wind Turbine Noises*, Springer.
- Williamson, C. H. K. (1996), 'Vortex dynamics in the cylinder wake'.
- Winkler, J., Temel, F. Z. & Carolus, T. (2007), 'Concept, design and characterization of a small aeroacoustic wind tunnel facility'.

In this master thesis project, the initial steps for the design of a new wind tunnel for aeroacoustic measurements are made. A literature study and 2D CFD simulations are used to create a new wind tunnel design. Thick corner vanes will be a characteristic feature of the design with the purpose of using them as base muellers to create a better environment for aeroacoustic measurements. The performance of the wind tunnel is evaluated by 3D CFD simulations. Noise measurements are used to find the noise characteristics of the fan-motor combination and to see how it propagates. Furthermore, predictions of the transmission loss through the corner vanes are made by using finite element analyses.

Technical
University of
Denmark

Nils Koppels Alle, Building 403
2800 Kgs. Lyngby
Tlf. 4525 1700

www.vindenergi.dtu.dk